

University of Southampton Research Repository

Copyright © and Moral Rights for this thesis and, where applicable, any accompanying data are retained by the author and/or other copyright owners. A copy can be downloaded for personal non-commercial research or study, without prior permission or charge. This thesis and the accompanying data cannot be reproduced or quoted extensively from without first obtaining permission in writing from the copyright holder/s. The content of the thesis and accompanying research data (where applicable) must not be changed in any way or sold commercially in any format or medium without the formal permission of the copyright holder/s.

When referring to this thesis and any accompanying data, full bibliographic details must be given, e.g.

Thesis: Author (Year of Submission) "Full thesis title", University of Southampton, name of the University Faculty or School or Department, PhD Thesis, pagination.

Data: Author (Year) Title. URI [dataset]

University of Southampton

Faculty of Engineering and Physical Sciences

School of Chemistry

Surface Chemistry for Point-of-Care Raman Spectroscopy

by

Bethany May Bowden

ORCID ID 0000-0002-2312-2727

Thesis for the degree of Doctor of Philosophy

18 February 2024

University of Southampton

Abstract

Faculty of Engineering and Physical Sciences

School of Chemistry

Doctor of Philosophy

Surface Chemistry for Point-of-Care Raman Spectroscopy

by

Bethany May Bowden

This work explores the fundamentals required for developing waveguide enhanced Raman spectroscopy (WERS) as a suitable technique for point-of-use biological detection. WERS has the capability to use low-cost and miniaturised or integrated optical components, with the potential for highly sensitive and low-burden detection. Currently, WERS devices being developed globally are immature and are not yet suitable for use outside of controlled laboratory conditions. This research aims to provide information on the surface chemistry required for waveguide sensors to drive the future development of highly sensitive WERS.

In this research, there has been a focus on the chemical functionalisation of tantalum pentoxide waveguides to tune the surface properties, enabling the future immobilisation of biorecognition elements. Self-assembled monolayers of octadecylphosphonic acid were used to show the suitability of phosphonic acid derivatives for waveguide surface modification. These were characterised using contact angle goniometry, measuring the hydrophobicity imparted by the monolayer. A probe molecule, *m*-nitrophenylphosphonic acid, was adsorbed to the waveguide surface, and WERS of a monolayer was shown.

Typical Raman reference materials cannot be used with WERS; thus, benzyl alcohol has been identified as a suitable standard to assess the function and calibration of the WERS spectrometer. The initial characterisation of benzyl alcohol formed a study into the scattering cross-sections of several solvents, which were determined using Raman microscopy and density functional theory. WERS was then performed, producing spectra of benzyl alcohol, benzyl- d_7 alcohol, and *m*-diethynylbenzene.

Substrates for surface enhanced Raman spectroscopy (SERS) were also investigated. Comparisons were drawn between the two methods, with SERS able to strongly enhance the signal, but with difficulties in reproducibility and stability. Biofunctionalized silver nanostars were produced, with the aim of assessing a combined WERS-SERS sandwich assay, although the research did not reach this stage.

A wax printer has been used to produce a paper fluidic device capable of incubating the glucose oxidase reaction with glucose and delivering the product to a SERS active surface.

Combining the above elements together with signal enhancement and more targeted efforts towards biological assays should demonstrate the benefits of WERS for accessible and rapid biosensing.

Table of Contents

Table of Contents	i
Table of Tables	v
Table of Figures	ix
Research Thesis: Declaration of Authorship	xvii
Acknowledgements	xix
Definitions and Abbreviations	xxi
Chapter 1 Introduction	1
1.1 Optical sensors	1
1.2 Raman spectroscopy	2
1.3 Raman instrumentation	6
1.4 Surface enhanced Raman spectroscopy	7
1.4.1 Electromagnetic mechanism	8
1.4.2 Charge transfer mechanism	9
1.4.3 SERS substrates	9
1.5 Waveguide enhanced Raman spectroscopy (WERS)	10
1.5.1 History of WERS.....	11
1.5.2 Fabrication considerations and choices.....	13
1.5.2.1 Wavelength	14
1.5.2.2 Coupling.....	14
1.5.2.3 Materials.....	15
1.5.2.4 Thickness	17
1.5.2.5 Shape	17
1.5.2.6 Signal collection.....	19
1.6 Summary of Raman spectroscopy for biosensing	19
1.7 Thesis structure	20
Chapter 2 Methods	23
2.1 SERS substrate preparation.....	23
2.1.1 Sphere segment void (SSV) substrates.....	23

Table of Contents

2.1.2	Silver nanostars (AgNS).....	25
2.2	Surface modification strategies	27
2.2.1	Gold SSV functionalisation.....	27
2.2.2	Functionalisation of AgNS.....	27
2.2.3	Preparation of AgNS in SSV cavity substrates.....	28
2.2.4	Functionalisation of Ta ₂ O ₅	28
2.3	Raman measurements	28
2.3.1	Assignment of spectra	28
2.3.2	SERS measurements	29
2.3.3	Cross-section determination	29
2.3.4	WERS measurements.....	31
2.4	Additional characterisation methods	32
2.4.1	Contact angle measurement	32
2.4.2	Scanning electron microscopy (SEM)	33
2.4.3	Transmission electron microscopy (TEM).....	33
2.4.4	Fluorescence microscopy.....	33
2.5	Wax printed fluidics	34
2.5.1	Glucose tests.....	34
2.6	Density functional theory (DFT).....	34
2.6.1	DFT calculation of spectral properties.....	34
Chapter 3	Phosphonic acid functionalisation	37
3.1	Overview	37
3.2	Functionalisation of Ta ₂ O ₅ with phosphonic acids	37
3.2.1	Immersion method	41
3.2.2	Tethering by aggregation and growth (T-BAG) method.....	46
3.3	WERS characterisation of phosphonic acid monolayers	47
3.4	Formation of functional interfaces	60
3.5	Summary	62

Chapter 4 Raman cross-section analysis of liquid analytes across spectrometer platforms	65
4.1 Overview.....	65
4.2 Raman cross-section of bulk organic liquids.....	65
4.2.1 Introduction.....	65
4.2.2 Experimental cross-section determination.....	70
4.2.3 DFT determination of cross-section.....	76
4.2.4 Comparison between DFT and experimental results.....	83
4.3 WERS spectra of bulk organic liquids	84
4.3.1 <i>m</i> -Diethynylbenzene	85
4.3.2 Benzyl alcohol.....	88
4.4 Summary	92
Chapter 5 SERS studies.....	95
5.1 Overview.....	95
5.2 Introduction to SERS substrates.....	95
5.2.1 Sphere segment void (SSV) substrates.....	96
5.2.2 Silver nanostars (AgNS)	96
5.3 Calculation of SERS enhancement factors	97
5.3.1 Benzenethiol.....	98
5.3.2 Aminobenzenethiol	101
5.3.3 Nitrobenzenethiol	105
5.4 Effects of SSV diameter on SERS	108
5.5 Silver nanostars functionalised with rabbit anti-BSA.....	112
5.5.1 Thiobenzonitrile functionalisation	113
5.5.2 DTNB functionalisation.....	116
5.5.3 Summary of AgNS biofunctionalization strategies.....	118
5.6 Introduction to paper fluidics	119
5.6.1 Glucose detection as proof of concept	121
5.7 Summary	128

Table of Contents

Chapter 6	Conclusions and further work	131
6.1	Research summary and conclusions	131
6.2	Further work	133
6.2.1	Biological recognition and detection	133
6.2.2	Phosphonic acid SAM characterisation	134
6.2.3	Development of SSV and AgNS substrates	134
6.3	Concluding statement.....	136
Appendix A	DFT calculation of polar derivatives.....	137
List of References	141

Table of Tables

Table 1 Comparison of the refractive index, waveguide geometry, loss, and Raman collection efficiencies for four materials tested in [46]. The superstrate was air $n=0$ and excitation wavelength 785 nm.	16
Table 2 The phosphonic acids chosen for this study are octadecylphosphonic acid and phenylphosphonic acid. The length of the molecule, the supplier and purity of the supplied reagent are included in the table.	41
Table 3 Pictures of 1 μ L droplets of water on Ta ₂ O ₅ substrates after being subjected to ODPA solutions for 5 min, 60 min, 24 h, and 1 week.	43
Table 4 Contact angles and hysteresis values for ODPA SAMs on Ta ₂ O ₅ after 24 h immersion.	44
Table 5 Contact angles and hysteresis values for ODPA SAMs on Ta ₂ O ₅ after 1 week immersion	44
Table 6 Fractional coverage of ODPA SAMs on Ta ₂ O ₅ calculated using the Cassie equation.	45
Table 7 Contact angle and hysteresis of phenylphosphonic acid SAMs formed after 1 week in water, ethanol and THF. Hysteresis value not recorded for THF due to substrate size.	45
Table 8 The contact angles and hysteresis for ODPA SAMs formed on Ta ₂ O ₅ using the T-BAG method. ODPA solutions were in EtOH and THF with initial concentrations of 1 mM - 0.001 mM.	47
Table 9 DFT predictions for each vibrational mode of CNPPA and the calculated Raman tensor.	54
Table 10 Raman tensors of selected vibrational bands of NPPA.	58
Table 11 The contact angle measured as a function of the ratio of -OCH ₃ to -OH terminated oligoethylene glycol units is increased	62

Table of Tables

Table 12 The liquid analytes used in this work and their key physical properties. Values have been taken from Sigma-Aldrich.	69
Table 13 Experimentally determined relative cross-sections of the liquid analytes, focussed on the C-C stretch (A) in Figure 32. Cyclohexane C-H stretch has been included. Peak intensity is the average over five measurements, showing the standard deviation.	73
Table 14 Experimentally determined cross-sections of the ring-breathing mode 12 of the aromatic analytes, (B) in Figure 32.	73
Table 15 Experimentally determined cross-sections of the aromatic C=C stretches.(C) in Figure 32.	74
Table 16 Experimentally determined cross-sections for the triple bond stretches. (D) in Figure 32.	75
Table 17 DFT calculations of the Raman cross-section using hybrid functional B3LYP and 6311G++(d,p) basis set. Showing the cross-sections for the aliphatic C-C stretch. (A) in Figure 33.	78
Table 18 DFT calculations of the Raman cross-section using hybrid functional B3LYP and 6311G++(d,p) basis set. Showing the cross-sections for the aromatic ring-breathing.(B) in Figure 33.	79
Table 19 DFT calculations of the Raman cross-section using hybrid functional B3LYP and 6311G++(d,p) basis set. Showing the cross-sections for the aromatic C=C stretches. (C) in Figure 33.	80
Table 20 DFT calculations of the Raman cross-section using hybrid functional B3LYP and 6311G++(d,p) basis set. Showing the cross-sections for the triple bond stretches.(D) in Figure 33.	81
Table 21 DFT calculations of the Raman cross-section using hybrid functional B3LYP and 6311G++(d,p) basis set. Showing the cross-sections for the C-H stretching region (E) in Figure 33.	82

Table 22 <i>m</i> -DEB vibrational frequencies and assignments made by King.(ref) The shift is that recorded in the Raman spectrum, with the WERS results in brackets where the two differ.	87
Table 23 The Raman shifts and assignment of benzyl alcohol. The figure in brackets represents the shift using WERS.	91
Table 24 The Raman shifts and assignment of benzyl- <i>d</i> ₇ alcohol. The figure in brackets represents the shift using WERS.	91
Table 25 The enhancement factors calculated for the 1576 cm ⁻¹ band of benzenethiol.	98
Table 26 The enhancement factors calculated for the 1002 cm ⁻¹ band of benzenethiol.	99
Table 27 The enhancement factors calculated for the 1078 cm ⁻¹ band of ABT on SERS substrates.	102
Table 28 The enhancement factors calculated for the 1145 cm ⁻¹ band of ABT on SERS substrates.	102
Table 29 The enhancement of NBT monolayers on the selected substrates for the 1338 cm ⁻¹ peak, relative to that of NBT monolayer on a flat gold substrate.	106
Table 30 Comparison of the enhancement factors calculated for BT and ABT on 600 nm and 220 nm SSV substrates with and without nanostars.	111
Table 31 Polar derivatives for CNPPA, calculated in Gaussian.	137
Table 32 Polar derivatives of NPPA, calculated in Gaussian.	138

Table of Figures

- Figure 1 The general structure of a planar waveguide. Light is guided within the high-index waveguide layer (n_w) by total internal reflection. The light penetrates the substrate (n_s) and superstrate (n_c) layers where it decays exponentially as an evanescent field. Image adapted from [9]..... 2
- Figure 2 Jablonski diagram showing the Raman Effect with Stokes and Anti-Stokes scattering, along with a representation of Rayleigh scattering. The dashed line represents the virtual energy level, and the solid lines the vibrational energy levels within the molecule. 3
- Figure 3 SERS E-melting procedure demonstrated on an SSV substrate by Mahajan *et al.* [29]. Left shows light incident on an SSV substrate, and shows Rayleigh and Raman scattered light. On the right, E-melting is depicted, showing that the labelled DNA strand dehybridises with $-\Delta E/+\Delta T$ to leave a single strand on the gold surface. 10
- Figure 4 Work by Dhakal *et al.* [49] showing a) Raman spectrogram as a function of hybridisation time. At $t = 60$ s, cDNA-Cy3 was introduced; (b) WERS spectra after the addition of cDNA at 6 s (red) and after hybridisation at 120 s (blue); (c) The intensity of the Raman signal ($\text{counts s}^{-1} \text{mW}^{-1}$) of the 1392 cm^{-1} line of Cy3 as the hybridisation reaction occurs; (d) WERS showing the stepwise functionalisation of Si_3N_4 waveguide..... 13
- Figure 5 Spectra showing the Raman background from rib waveguides made from different materials (Raza *et al.*) This was conducted using a 785 nm laser and TE excitation. The top of the waveguide was clad in air. The spectrum of TiO_2 has had the intensity reduced by a factor of 10 for comparison purposes. [46] 16
- Figure 6 Cross-sections for various waveguide configurations overlaid with the simulated fundamental modal intensity distribution for planar (a, d), rib (b, e), and channel waveguides (c, f). TE (top) and TM (bottom) polarizations have been calculated. The planar waveguide exhibits pure TE and TM modes,

Table of Figures

while the rib and channel waveguides exhibit quasi-TE and quasi-TM modes. The arrows indicate the major E -field direction. [42]	19
Figure 7 Project vision. The waveguide chip is shown as part of the device, including the biorecognition layer, microfluidics, and the laser coupling path.....	21
Figure 8 Diagram showing the stepwise process of producing SSV substrates with 600 nm polystyrene sphere standards. Inset photograph showing the opalescent surface produced from the array of polystyrene spheres.....	23
Figure 9 Chronoamperogram showing the typical response curve for the electrodeposition of gold around the 600 nm polystyrene sphere template. Potential -0.72 V.	24
Figure 10 SEM image of an SSV substrate with 600 nm sphere template. Accelerating voltage 10.0 kV, 30000× magnification, scale bar 100 nm.....	25
Figure 11 UV-vis spectra of three AgNS colloids showing absorption maxima at 380 nm and displaying a large tail in the visible to near IR region. Inset photograph of AgNS colloid.....	26
Figure 12 TEM images of silver nanostars. Left: showing an individual nanostar (accelerating voltage 15.0 kV, 70000× magnification, scale bar 100 nm); right: showing a cluster of nanostars (accelerating voltage 15.0 kV, 40000× magnification, scale bar 100 nm). Images collected by Dr A. Marti-Morant.	26
Figure 13 The Wilson modes of benzene as depicted by Gardner and Wright [57]. Arrows indicate atomic motion, the + symbol indicates movement out of the plane and towards the reader, and the - symbol depicts the opposite. Modes that are degenerate are shown by the labelling a and b.	30
Figure 14 Photograph of the WERS apparatus showing the overall set-up, a close-up of the waveguide chip, and an example of 637 nm light being coupled into the waveguide for visualisation of the light path.	32
Figure 15 Contact angle measurements using Krüss DSA where the baseline is defined by the pink line, the droplet outlined by the green line and the region	

selected in the blue box. The contact angle is shown between the white line and the baseline.	33
Figure 16 Self-assembling molecules that have been used to functionalise metal oxide surfaces, which include trichlorosilanes, alkoxy silanes, phosphates, and phosphonate esters.	38
Figure 17 Mechanism of phosphonic acid attachment to Lewis acidic (top) and Lewis basic (bottom) oxides. Image from [89].	39
Figure 18 Stepwise biofunctionalisation of ITO with fluorescently labelled proteins. The carboxylic acid monolayer is activated using EDC/NHS coupling to form a mixed monolayer with CH ₃ and OH terminal groups. DSC/DMAP is used to attach labelled BSA through the OH groups. Image from [87].	40
Figure 19 Graph showing the change in water contact angle with respect to the functionalisation of Ta ₂ O ₅ with ODPA The contact angle with the error bar showing standard deviation is shown. At least three repeats were conducted for each measurement condition.	43
Figure 20 The set-up of the tethering by aggregation and growth (T-BAG) method. The Ta ₂ O ₅ wafer is suspended vertically in a solution of the target phosphonic acid solution, the solvent is left to evaporate, forming a functionalised Ta ₂ O ₅ substrate.	46
Figure 21 WER spectra of NPPA monolayers on Ta ₂ O ₅ waveguide (bold lines), also showing the background (pale lines) of an unmodified chip, in the TE configuration. The background and sample spectra have been collected with various acquisition times, and potential sample peaks have been indicated with *. The excitation wavelength is 785 nm, with 6.3 mW power in the waveguide.	49
Figure 22 A depiction of the planar waveguide and molecular axes, showing the tilt, rotation and azimuthal angles.	51
Figure 23 The Raman spectrum of CNPPA powder. The spectrum was collected using 785 nm excitation, 1 mW, and an acquisition time of 10 s.	52

Table of Figures

- Figure 24 DFT Raman spectrum of a single molecule of CNPPA. This was calculated at the B3LYP 6-311G++(d,p) level of theory. The Raman shift was scaled by a factor of 0.9668 to account for the exchange correlation. 53
- Figure 25 Structure and coordinate axes for CNPPA. The expected surface plane where CNPPA would be expected to adsorb when forming a monolayer is shown by the black line. This is representative only, as the adsorption angle is yet to be fully determined. 54
- Figure 26 The Raman spectrum of NPPA powder. A significant fluorescent background was observed, obscuring Raman features. The spectrum is shown for the range 1250-1450 cm^{-1} which features the symmetric NO_2 stretch..... 56
- Figure 27 DFT Raman spectrum of a single molecule of NPPA. This was calculated at the B3LYP 6-311G++(d,p) level of theory. The Raman shift was scaled by a factor of 0.9668 to account for the exchange correlation. 57
- Figure 28 Structure and Cartesian axis of NPPA used in this calculation. Note the two N=O double bonds. A representative surface plane showing where NPPA would be expected to adsorb in a monolayer is depicted by the black line, although the angle is yet to be determined through a combined theoretical and experimental approach. 57
- Figure 29 Spectra showing the DFT predictions of free (bottom), monodentate (middle) and bidentate (top) coordinated CNPPA to Ta atoms. 59
- Figure 30 Confocal fluorescence images of Ta_2O_5 with different surface chemistries. The substrates were incubated with AF488 dye. Top left shows the covalent linkage of AF488 to the surface and shows the highest density of dye. Top middle shows where dye was introduced to the surface, but subsequently washed away. Top right shows a phosphonic acid monolayer in the absence of dye. Bottom left shows the mixed monolayer, where some dye is covalently linked. A low level of fluorescence is observed. 61
- Figure 31 Graph from [99] showing the dependence of the cross-section on environmental factors, in this case, the increasing concentration of

acetone. Green represents C=O and red the C-H stretching modes of acetone dissolved in the standard, acetonitrile.	67
Figure 32 Raman spectra of the selected analytes which have been offset for clarity. Note: <i>m</i> -DEB and benzyl- <i>d</i> ₇ alcohol were not measured under the standard conditions and have been scaled for visual purposes. The regions of interest are highlighted as (A) C-C stretching, (B) ring breathing, (C) C=C stretching, (D) triple bond stretching.	72
Figure 33 DFT Raman spectra of the solvents included in this study, using the B3LYP hybrid functional and 6-311G++(d,p) basis set. The spectra are offset for clarity, and the frequency has been scaled by 0.9668. The intensity of the spectrum of <i>m</i> -DEB has been divided by a factor of 4 to allow greater visualisation of the remaining spectra. Here (A) shows C-C stretching, (B) shows ring breathing, (C) is C=C stretching, (D) shows triple bonds and C-D stretching, and (E) is C-H stretching.....	77
Figure 34 Graph showing the differences in the Raman cross-section calculated using DFT (triangles) and laboratory measurements (squares). The similarity of the two methods validates the DFT approach as a way of determining Raman cross-sections. Only cyclohexane has data for both experimental and DFT cross-sections in the C-H stretching region at approx. 3000 cm ⁻¹	83
Figure 35 WERS background signal observed from a Ta ₂ O ₅ waveguide chip exposed to air with 785 nm excitation. A significant background is observed between 250-1000 cm ⁻¹ intrinsic to vibrations in Ta ₂ O ₅	85
Figure 36 Raman and WERS spectra of <i>m</i> -diethynylbenzene. For WERS, a 2 μL droplet of <i>m</i> -DEB was placed on the surface of a Ta ₂ O ₅ waveguide. 785 nm light was coupled into the waveguide using a grating. The acquisition time was 5 s. For Raman, a droplet of <i>m</i> -DEB was placed on a microscope slide.....	86
Figure 37 The proposed interaction between the alkyne and weakly acidic hydroxyl sites	88

Table of Figures

- Figure 38 Overlaid Raman and WERS spectra showing benzyl alcohol and deuterated benzyl alcohol. The spectra have been scaled and offset for clarity, and lines have been added to aid comparison between peaks. 90
- Figure 39 Raman and WERS spectra of benzyl alcohol and deuterated benzyl alcohol using 6.3 mW 785 nm laser. Spectra have been de-noised according to a non-local means algorithm and the background subtracted. Image taken from Ettabib *et al.* Grating-incoupled waveguide enhanced Raman sensor. 93
- Figure 40 SEM image showing the distribution of silver nanostars on an SSV surface. Accelerating voltage 10 kV, 15000× magnification, scale bar 1 μ M. ... 99
- Figure 41 SERS spectra for benzenethiol monolayers on AgNS (top), SSV (middle), and combined AgNS and SSV substrates (bottom). The spectra have been normalised to counts $\text{mW}^{-1} \text{s}^{-1}$ and offset for clarity. 785 nm excitation. 100
- Figure 42 SERS spectra for *p*-aminobenzenethiol monolayers on AgNS (top), SSV (middle), and combined AgNS and SSV substrates (bottom), the intensity of this spectrum was divided by 100 to allow for comparison between the spectra. The spectra have been normalised to counts $\text{mW}^{-1} \text{s}^{-1}$ and offset for clarity. 785 nm excitation..... 103
- Figure 43 The Raman spectrum of a nitrobenzenethiol monolayer on flat gold coated microscope slide. Collection parameters: 785 nm excitation, 10 s, 0.05 mW..... 105
- Figure 44 SER spectra showing NBT monolayers on different substrates, flat Au (top), AgNS, SSV, and SSV+AgNS (bottom). The spectra have been normalised to counts $\text{mW}^{-1} \text{s}^{-1}$ and offset for clarity. 107
- Figure 45 SEM image showing the long-range surface packing of an SSV substrate templated using 220 nm sphere standards. Accelerating voltage 15.0 kV, 4000x magnification, scale bar 1 μ m..... 108
- Figure 46 SERS showing a comparison between 600 nm and 220 nm SSV substrates for BT. The double headed arrow in each spectrum indicates 10000 Counts mW^{-1}

s ⁻¹ . Top – in the absence of silver nanostars. Bottom – with silver nanostars in cavity.	109
Figure 47 SERS showing a comparison between 600 nm and 220 nm SSV substrates for ABT. The arrows indicate 10000 Counts mW ⁻¹ s ⁻¹ (top spectra) and 10 ⁶ Counts mW ⁻¹ s ⁻¹ (bottom spectra). Top – in the absence of silver nanostars. Bottom – with silver nanostars in cavity.....	110
Figure 48 SEM image showing a single AgNS residing within the 220 nm SSV cavity. Accelerating voltage 15 kV, 50000x magnification, scale bar 100 nm.	112
Figure 49 SERS spectrum of AgNS functionalised with a mixed monolayer of TBN and MHDA. Collection parameters: 785 nm, 0.05 mW, 10 s.....	114
Figure 50 UV-vis spectrum showing silver nanostars functionalised with a mixed monolayer of TBN and MHDA. $\lambda_{\max} = 400$ nm.	115
Figure 51 UV-vis spectrum showing silver nanostars functionalised with a mixed monolayer of TBN and MHDA, followed by binding of IgG antibody.	115
Figure 52 TEM micrographs of AgNS functionalised with TBN-MHDA (a, b) and TBN-MHDA + Ab (c, d). (a) accelerating voltage 100 kV, magnification 20000x, scale bar 500 nm; (b) 100 kV, 120000x, scale bar 100 nm; (c) 100 kV, 20000x, scale bar 1 μ m; (d) 100 kV, 20000x, scale bar 200 nm.	116
Figure 53 The SERS spectrum of AgNS functionalised with DTNB. Collection parameters: 785 nm excitation, 10 s integration, 0.05 mW.	117
Figure 54 UV-visible spectrum of DTNB functionalised AgNS.	117
Figure 55 TEM images showing DTNB functionalised AgNS	118
Figure 56 Paper microfluidic detection of glucose and BSA. The boundaries have been defined by a photoresist, but the same effect is observed when the boundaries are wax.[130]	120
Figure 57 A 3D paper fluidic device allowing the incubation of cardiac marker miR-29a-3p with SERS active nanoparticles. [131].....	121

Table of Figures

- Figure 58 Glucose detection methods using 4-MPBA attached to gold SSV surface. The indirect detection method uses H_2O_2 to cleave the $C-B(OH)_2$ bond to give 4-MP. The direct method forms a complex with glucose and the boronic acid..... 123
- Figure 59 The wax printed design used for the glucose detection experiment. Glucose oxidase was spotted into the incubation zone. The outlet zone was pressed against the 4-MPBA decorated SSV substrate, allowing transfer of the reactants from the paper to the SERS platform. This photograph depicts the set-up for *in-situ* Raman monitoring. A hole was made in the paper, and the laser focussed on the SSV substrate. 124
- Figure 60 SERS spectra on SSV substrate showing the conversion of MPBA monolayer to MP in the presence of hydrogen peroxide. Top shows the averaged spectrum of 4-MPBA, middle shows the averaged spectrum of 4-MPBA after H_2O_2 exposure, and bottom shows the spectrum of a pure 4-MP monolayer..... 125
- Figure 61 SERS spectrum of 4-MPBA monolayer on SSV substrate after being exposed to glucose in the absence of glucose oxidase. 126
- Figure 62 The SERS response to H_2O_2 concentration using 3-MPBA coated AuNPs in PBS. [139] Left plots the ratio of the bands at 882 cm^{-1} and 995 cm^{-1} corresponding to the ring stretching and C-C bending modes, respectively. The 882 cm^{-1} band is specific to the product of the reaction, 3-MP. Right shows the average SERS spectra for increasing concentrations in the range 0.1-100 μM 128

Research Thesis: Declaration of Authorship

Print name: Bethany M. Bowden

Title of thesis: Surface Chemistry for Point-of-Care Raman Spectroscopy

I declare that this thesis and the work presented in it are my own and has been generated by me as the result of my own original research.

I confirm that:

1. This work was done wholly or mainly while in candidature for a research degree at this University;
2. Where any part of this thesis has previously been submitted for a degree or any other qualification at this University or any other institution, this has been clearly stated;
3. Where I have consulted the published work of others, this is always clearly attributed;
4. Where I have quoted from the work of others, the source is always given. With the exception of such quotations, this thesis is entirely my own work;
5. I have acknowledged all main sources of help;
6. Where the thesis is based on work done by myself jointly with others, I have made clear exactly what was done by others and what I have contributed myself;
7. Parts of this work have been published as:-
 - M. A. Ettabib, A. Marti, Z. Liu, B. M. Bowden, M. N. Zervas, P. N. Bartlett, and J. S. Wilkinson; Waveguide Enhanced Raman Spectroscopy for Biosensing: A Review; *ACS Sens.*, **2021**, 6, 6, 2025–2045
 - M. S. Zalaffi, P. Ugo, A. Marti, B. M. Bowden, A. E. Russell, P. N. Bartlett; SERS using nanostar-in-cavity structures; *J Raman Spectrosc*, **2022**, 53(11), 1871
 - M. A. Ettabib; B. M. Bowden; Z. Liu; A. Marti; G. M. Churchill; J. C. Gates; M. N. Zervas; P. N. Bartlett; J. S. Wilkinson; Grating-Incoupled Waveguide-Enhanced Raman Sensor; *PLoS ONE*, **2023**, 18(8)
 - Z. Liu, M. A. Ettabib, B. M. Bowden, P. N. Bartlett, J. S. Wilkinson, M. N. Zervas; Multiframe-based non-local means denoising for Raman spectra; *Spectrochimica Acta Part A: Molecular and Biomolecular Spectroscopy*, **2024**, In Press

Signature: Date:

Acknowledgements

First and foremost, I would like to thank my supervisor Prof. Phil Bartlett for all his guidance and encouragement throughout. Getting through a PhD research project is never straightforward, and this was no exception to that rule. Thank you for staying supportive. I would also like to say thank you to my second supervisor, Prof. Sumeet Mahajan for your helpful advice in SERS and writing.

The whole experience was brightened by every member of the Bartlett group, past and present, providing frequent laughs and the occasional scientific discussion over a cup of tea. This would not have been possible without Ann and Genny running the show, so major thanks are due for keeping us all suitably caffeinated.

In addition, I would also like to thank Prof. James Wilkinson, Prof. Michalis Zervas, Dr Mohamed Ettabib, and Liu Zhen who provided a range of additional perspectives on all the work that was carried out. I can only hope I have imparted as much chemical knowledge as I have learned everything optics from you.

Nikolay Zhelev deserves major praise for keeping all the equipment in the department running, providing training, and for the plentiful supply of gold coated slides.

I would like to express my gratitude to the Defence Science and Technology Laboratory (Contract No. DSTLX-1000128554) for supporting an EPSRC industrial CASE award and making this research possible. I can't thank Dr Sarah Goodchild enough for all her advice, determination, and encouragement along the way. In addition, I would like to express huge levels of appreciation to Sarah, Tom Ciuksza, and the team for helping me in that final push across the finish line.

On a more personal note, I would like to thank my parents for their lifelong encouragement. A great big thank you to Jack for your love, supporting me the whole way, and knowing exactly what advice to give and when to give it (and when to stand back and offer biscuits instead). I've learned a lot from you.

And to Sharon Sharp (that's without an 'e'). I hope things are tickety-boo.

Definitions and Abbreviations

ABT	4-Aminobenzenethiol
AFM	Atomic force microscopy
AgNS	Silver nanostars
BA	Benzyl alcohol
BSA	Bovine serum albumin
BT.....	Benzenethiol
CARS	Coherent anti-Stokes Raman spectroscopy
CCD	Charge coupled device
cDNA.....	Complimentary DNA
CMC.....	Critical micelle concentration
CNPPA.....	4-Cyanophenylphosphonic acid
CT.....	Charge transfer
DBCO	Dibenzocyclooctyne
DFT	Density functional theory
DMAP	4-(Dimethylamino)pyridine
DNA	Deoxyribonucleic acid
DSA	Drop shape analyser
DSC	<i>N,N'</i> -Disuccinimidyl carbonate
DTNB.....	5,5'-Dithiobis(2-nitrobenzoic acid)
EDC	1-Ethyl-3-(3-dimethylaminopropyl)carbodiimide
EF.....	Enhancement factor
EM	Electromagnetic
GOx.....	Glucose oxidase
HRP	Horseradish peroxidase

Definitions and Abbreviations

IPA.....	Isopropyl alcohol
IR.....	Infrared
ITO.....	Indium tin oxide
LFA.....	Lateral flow assay
LSPR.....	Localised surface plasmon resonance
<i>m</i> -DEB.....	<i>m</i> -Diethynylbenzene
MES.....	2-(<i>N</i> -Morpholino)ethanesulfonic acid
MGITC.....	Malachite green isothiocyanate
MHDA.....	Mercaptohexadecanoic acid
MP.....	4-Mercaptophenol
MPBA.....	Mercaptophenylboronic acid
NA.....	Numerical aperture
NBT.....	4-Nitrobenzenethiol
NEXAFS.....	Near edge X-ray absorption fine structure
NHS.....	<i>N</i> -Hydroxysuccinimide
NIR.....	Near infrared
NPPA.....	3-nitrophenylphosphonic acid
ODPA.....	Octadecylphosphonic acid
OEG.....	Oligoethyleneglycol
PBS.....	Phosphate buffered saline
PEG.....	Polyethyleneglycol
POC.....	Point of care
PPA.....	Phenylphosphonic acid
PTCS.....	<i>p</i> -Tolyltrichlorosilane
RNA.....	Ribonucleic acid
RRS.....	Resonance Raman spectroscopy

SAM	Self-assembled monolayer
SEM.....	Scanning electron microscopy
SERRS.....	Surface enhanced resonance Raman spectroscopy
SERS.....	Surface enhanced Raman spectroscopy
ssDNA	Single stranded DNA
SSV.....	Sphere segment void
T-BAG.....	Tethering by aggregation and growth
TBN	Thiobenzonitrile
TE.....	Transverse electric
TEM	Transmission electron microscopy
TERS.....	Tip enhanced Raman spectroscopy
THF	Tetrahydrofuran
TM	Transverse magnetic
ToF-SIMS	Time of flight secondary ion mass spectrometry
TTCS.....	Trichlorophenylsilane
UV	Ultraviolet
WERS	Waveguide enhanced Raman spectroscopy
XPS.....	X-ray photoelectron spectroscopy

Chapter 1 Introduction

There is an understandable need for highly sensitive detection methods within a range of applications which can – amongst others – include biosensors, trace chemical detection, and environmental monitoring. Optical sensors form a major part of this, and the type of sensor employed can vary depending on the needs of the user and the analyte. Several books and review articles have been written covering refractometric techniques,¹ interferometry,^{2,3} fluorescence,^{4,5} and vibrational spectroscopies.^{6,7} Research into the development of flexible, cost-effective, and low-burden optical systems is an active and ongoing area and forms the overarching focus for this research. This introduction will focus on optical sensor technologies and how these may be applied for the detection of biological material.

1.1 Optical sensors

Optical sensors convert light into a measurable electrical signal which can then be analysed by the user. The optical signal may originate from a labelled target molecule, observed in fluorescence and UV-visible absorption techniques. Alternatively, label-free techniques such as interferometry, surface plasmon resonance, and vibrational spectroscopies may be employed. The costs and benefits of each must be considered. For instance, the labelling process increases the cost and labour intensiveness of the measurement but may result in very low limits of detection. The simplicity and flexibility of label-free approaches is attractive, but the sensitivity of such devices may be a limiting factor in the absence of further research. In each case, the specificity must be considered, although this can be controlled through careful choice of surface chemistry. For example, refractometers can be extremely sensitive, but non-specific binding may result in false positives.⁸

The limit of detection can be improved in both labelled and non-labelled techniques by confining light within a waveguide and probing the analytes captured within the evanescent field.^{9,10} The signal collection efficiency can also be highly efficient. From a manufacture point of view, the tuneability and integrability of waveguides into lab-on-a-

chip style devices are appealing. This is beneficial in device miniaturisation and aids progress in the development of portable technologies.

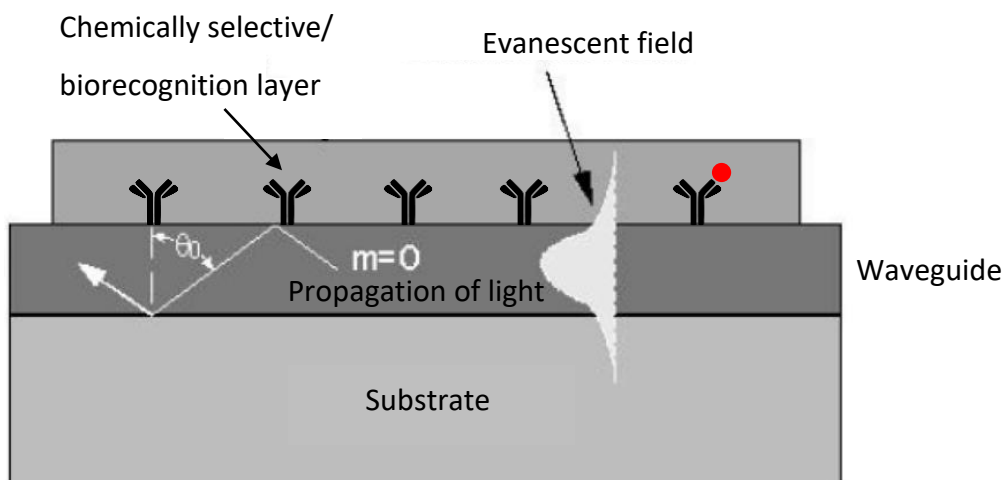


Figure 1 The general structure of a planar waveguide. Light is guided within the high-index waveguide layer (n_w) by total internal reflection. The light penetrates the substrate (n_s) and superstrate (n_c) layers where it decays exponentially as an evanescent field. Image adapted from [9].

Analytes held within the evanescent field experience an increase in the local light intensity in addition to being probed over a greater interaction length, whereas material in the bulk is unaffected. It is possible to control the affinity of the surface towards target materials through absorbent polymers or by self-assembled monolayers (SAMs). Self-assembled monolayers form structured arrays of molecules that are covalently linked to the waveguide surface through an anchor group.¹¹ The terminal functional group of the SAM imparts surface properties such as charge, hydrophobicity, or allows for the immobilisation of recognition elements.¹¹

1.2 Raman spectroscopy

Infrared (IR) and Raman spectroscopies are both vibrational spectroscopies that are non-destructive and give in-depth characterisation of the molecule. Most untreated biological samples are aqueous, which limits the use of IR spectroscopy without sample pre-treatment as water strongly absorbs IR radiation. Raman spectroscopy on the other hand is not impeded by aqueous environments, as the scattering cross section of water is very

low. The requirement for sample labelling or pre-treatment is minimal with Raman spectroscopy when compared with techniques such as fluorescence microscopy, and the measurement is often able to take place under ambient temperature and pressure conditions. The ability for multiplex analysis is an additional reason why this technique may be chosen over – or in combination – with others.

The main drawback is that the Raman effect is very weak, so analysis of low concentration samples can be challenging. Considerable research focus aims to increase the Raman effect by increasing the incident light intensity and molecular polarizability which will be covered in more detail later in the chapter.

The Raman Effect describes the inelastic scattering events that occur when light interacts with a molecule to give characteristic information about the vibrational modes of the molecule (Figure 2). Photons from a monochromatic light source incident on a molecule interact to excite the molecule to a virtual energy level. Most of the light is scattered elastically and is termed Rayleigh scattering. In a small proportion of cases (~ 1 in 10^8)¹² the incident photons can exchange energy with the molecule resulting in the emission of a second photon allowing the molecule to return to a lower vibrational energy level. For this energy exchange to occur, the molecule must exhibit a change in polarizability on vibration.

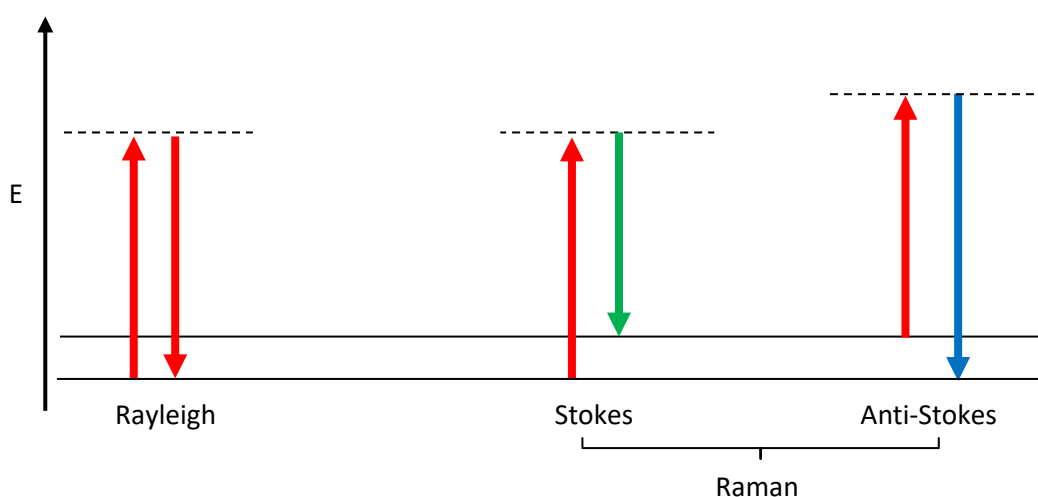


Figure 2 Jablonski diagram showing the Raman Effect with Stokes and Anti-Stokes scattering, along with a representation of Rayleigh scattering. The dashed line represents the virtual energy level, and the solid lines the vibrational energy levels within the molecule.

Chapter 1

The classical theory of Raman spectroscopy treats the incident light as a wave. This means the molecule interacts with an oscillating electric field. In the presence of the electric field, a time-dependent dipole moment is induced (μ_{ind}). The magnitude of the induced dipole is a product of the applied electric field (E) and the polarizability (α) of the molecule.

$$\mu_{\text{ind}} = \alpha E \quad (1.1)$$

As the magnitude of E varies with time, the dipole moment within the molecule also varies. The oscillating dipole moment emits a quantum of energy, and the molecule relaxes to lower vibrational state.

Polarizability is the ease at which the electron cloud can be distorted by the applied electric field and is a property intrinsic to the molecule. The polarizability depends on the orientation of the electric field relative to the molecular axis, meaning that polarizability is a tensor quantity having magnitude in all directions.

$$\begin{pmatrix} \mu_x \\ \mu_y \\ \mu_z \end{pmatrix} = \begin{pmatrix} \alpha_{xx} & \alpha_{xy} & \alpha_{xz} \\ \alpha_{yx} & \alpha_{yy} & \alpha_{yz} \\ \alpha_{zx} & \alpha_{zy} & \alpha_{zz} \end{pmatrix} \begin{pmatrix} E_x \\ E_y \\ E_z \end{pmatrix} \quad (1.2)$$

For Raman scattering to occur, the molecular vibration must be accompanied by a change in molecular polarizability. If there is no change in polarizability, then only elastic scattering is observed. This can be explained by expansion of the α and E terms in $\mu = \alpha E$ to take into account the vibration of the molecule and the oscillation of the electric field as a function of time. Equation 1.3 describes the electric field (E) of a light wave oscillating with frequency ν_0 with amplitude E_0 at a given moment in time (t).

$$E = E_0 \cos(2\pi\nu_0 t) \quad (1.3)$$

Substitution of the above expression for E into (1.1) shows that the oscillating electric field causes the induced dipole to oscillate at the frequency of the incident radiation.

$$\mu_{\text{ind}} = \alpha E_0 \cos(2\pi\nu_0 t) \quad (1.4)$$

To be able to derive an expression for the time-dependent α term, the nuclear distortion of a vibrating molecule must be considered. This is represented by (1.5). A molecule

vibrating with frequency ν_{vib} undergoes nuclear distortion with respect to its equilibrium position Q , where Q_0 is the maximum vibrational amplitude.

$$Q = Q_0 \cos(2\pi\nu_{\text{vib}}t) \quad (1.5)$$

The polarizability of the vibrating molecule can be described using equation 1.6 where α_0 is the polarizability at the equilibrium position, and the rate of change of α and Q are evaluated around the equilibrium position.

$$\alpha = \alpha_0 + \left(\frac{\delta\alpha}{\delta Q}\right)_0 Q \quad (1.6)$$

Thus, the change in polarizability during the molecular vibration can be calculated from substituting the expression for Q in (1.5) into (1.6) to give equation 1.7.

$$\alpha = \alpha_0 + \left(\frac{\delta\alpha}{\delta Q}\right)_0 Q_0 \cos(2\pi\nu_{\text{vib}}t) \quad (1.7)$$

With the α and E contributions to the induced dipole having been assessed, it is possible derive equation 1.8. This equation describes the induced dipole, which varies with time, the electric field amplitude, and the vibration.

$$\mu_{\text{ind}} = \left[\alpha_0 + \left(\frac{\delta\alpha}{\delta Q}\right)_0 Q_0 \cos(2\pi\nu_{\text{vib}}t)\right] [E_0 \cos(2\pi\nu_0t)] \quad (1.8)$$

By using the trigonometric relationship in (1.9), it is possible to derive an interpretation of (1.8) with respect to the Rayleigh (ν_0), Stokes ($\nu_0 - \nu_{\text{vib}}$), and Anti-Stokes ($\nu_0 + \nu_{\text{vib}}$) terms to give (1.10).

$$\cos A \cos B = \frac{1}{2} [\cos(A + B) + \cos(A - B)] \quad (1.9)$$

$$\mu_{\text{ind}} = \underbrace{\alpha_0 E_0 \cos(2\pi\nu_0t)}_{\text{Rayleigh}} + \underbrace{\frac{1}{2} \left(\frac{\delta\alpha}{\delta Q}\right)_0 Q_0 E_0 \{\cos[2\pi(\nu_0 + \nu_{\text{vib}})t] + \cos[2\pi(\nu_0 - \nu_{\text{vib}})t]\}}_{\text{Stokes and Anti-Stokes}} \quad (1.10)$$

If a vibration occurs without a corresponding change in polarizability, then $\left(\frac{\delta\alpha}{\delta Q}\right)_0 Q_0 = 0$ and there is no contribution from the second part of equation 10. In this case, equation 10 simplifies to the Rayleigh term – $\mu_{\text{ind}} = \alpha_0 E_0 \cos(2\pi\nu_0t)$ – hence light is only scattered

Chapter 1

elastically. If $\left(\frac{\delta\alpha}{\delta Q}\right)_0 Q_0 \neq 0$ then the polarizability changes with the vibration. The induced dipole oscillates at a combination of the excitation frequency and the vibrational frequency to give Anti-Stokes and Stokes scattering.

The magnitude of Raman scattering is directly proportional to λ^{-4} , such that a laser with wavelength 633 nm would have a greater field strength than that of a 785 nm laser. Hence, there is a loss in signal intensity at longer excitation wavelengths. Where biological detection is concerned, however, a great deal of autofluorescence and background signal is observed at shorter wavelengths. The laser wavelength must therefore be chosen to maximise the signal intensity whilst reducing any competing signal. 785 nm excitation is known to be effective for biological Raman detection, as the wavelength lies mostly outside the autofluorescence range without significantly compromising the signal collection intensity and signal to noise ratio.

1.3 Raman instrumentation

Modern, conventional Raman microscopy uses the backscattering configuration. In this arrangement, the laser source is directed to the sample through a series of mirrors and is then focused on the sample using an appropriate objective. Scattered light is collected at 180° relative to the incident light and follows the same path in reverse. The scattered light passes through a Rayleigh rejection filter and is passed to a holographic grating, where the light is separated based on wavelength onto a CCD detector. This data is then sent to a digital display for the user to analyse.

A selection of excitation wavelengths can be chosen, commonly including 532 nm, 633 nm, 785 nm, and 1064 nm. The intensity of Raman spectra obtained from shorter excitation wavelengths is greater than for longer excitation wavelengths by a factor of λ^{-4} . However, longer wavelengths are often chosen to reduce background fluorescence within the sample. Compounds in resonance at the chosen wavelength can also result in greatly enhanced spectra.

The choice of objective is also important as the magnification and numerical aperture affect the collection efficiency and the number of molecules sampled. A 5 \times objective can give a good spectrum averaged over a large area of the sample, although the collection is

weak. 50× objectives may be employed and can be used to look at specific areas of interest (*e.g.*, defects, nanoparticles) and are capable of efficient collection, resulting in highly detailed spectra.

Spectrometers of this type are capable of highly sensitive, and highly resolved measurements and can be used with surface enhanced Raman spectroscopy (SERS) to observe enhancements on the magnitude of up to 10^{14} compared to standard Raman measurements. However, this equipment is often costly, bulky and extremely sensitive to misalignment of the optical components, so alternatives are being sought in handheld and smartphone-integrated devices.^{13–15}

1.4 Surface enhanced Raman spectroscopy

Surface enhanced Raman spectroscopy (SERS) is a surface sensitive technique that results in the enhancement of the Raman signal generated by molecules adsorbed at a roughened or nanostructured metallic substrate. Analytes within 10 nm of the substrate surface can experience the SERS effect.⁶ The signal enhancement for SERS can be of the magnitude 10^{14} - 10^{15} enabling single molecule detection in idealised conditions,^{16,17} or in the region of 10^6 - 10^7 for conventional SERS techniques, enabling the detection of monolayers and sub-monolayers of target material.

Fleischmann, Hendra and McQuillan first discovered the SERS effect in 1974, observing a 10^6 enhancement of the Raman spectra of pyridine adsorbed on a roughened silver electrode.¹⁸ Initially attributing this enhancement to the large surface area, this finding generated a surge in interest in the field and by the late 1970s, Albrecht and Creighton,¹⁹ and Jeanmaire and Van Duyne²⁰ provided the theories that are used to explain the surface enhancement effect to this day.

The enhancement is made up of two main contributions: the change in the polarizability of a molecule occurring as a result of adsorption to a surface, and the amplification of the electric field experienced by molecules in close proximity to the surface. These effects, termed the chemical or charge transfer (CT) mechanism, and the electromagnetic (EM) mechanism contribute 10^2 - 10^3 (CT) and up to 10^{10} (EM) to the overall enhancement.

$$P_{\text{SERS}} = G_{\text{SERS}}^{\text{EM}} G_{\text{SERS}}^{\text{CT}} P_{\text{Raman}} \quad (1.11)$$

Chapter 1

The SERS scattered power is a product of the two SERS contributions and the Raman scattered power. Where $P_{\text{Raman}} = KN\sigma I$ describes the Raman signal generated by a sample, K represents the fraction of photons that reach the detector, N is the number of illuminated molecules, σ is the absolute Raman scattering cross-section of the vibrational mode, and I is the laser intensity impinging on the sample.⁶

1.4.1 Electromagnetic mechanism

Enhancement by the electromagnetic mechanism relies on the generation of a strong electromagnetic field at the surface of a nanostructured material. This can be considered to have two contributions, an enhancement of the incident light, and an enhancement of the scattered light. At a metal-dielectric interface, electrons oscillate at a frequency intrinsic to the metal itself, creating a coherent oscillation of charges known as a surface plasmon. When the excitation laser is of the correct frequency, it can couple to the plasmon mode. Localised surface plasmon resonance (LSPR) occurs when the electromagnetic radiation is confined to localised hot spots, which is the case for metals with structures smaller than the wavelength of the incident light – typically 5-100 nm. This results in the amplification of the incident light, so the electric field that is interacting with the analyte is increased. Silver and gold are effective SERS substrates because they have a free electron and plasmon resonance frequency in the visible-NIR region.

The re-radiation enhancement is the enhancement of the light scattered by the analyte. The power radiated by the oscillating dipole is increased due to being in the enhanced incident field; the scattered light is also amplified by coupling into a plasmon. The intensity of SERS is therefore proportional to the product of the incident and re-radiation enhancements.

$$I_{\text{SERS}} \propto \left| \frac{E_{\text{loc}}(\omega_0)}{E_0(\omega_0)} \right|^2 \left| \frac{E_{\text{loc}}(\omega_{\text{Raman}})}{E_0(\omega_{\text{Raman}})} \right|^2 \quad (1.12)$$

In the low frequency region, where the frequency of the incident and scattered light can be approximated as the same, then the total SERS intensity is proportional to $|E|^4$. Hence, a small increase in electric field enhancement can lead to a significant enhancement in Raman intensity. This is the origin of the electromagnetic enhancement.

1.4.2 Charge transfer mechanism

Interaction of the analyte through direct bonding to the substrate alters the polarizability of the molecule relative to its unbound state, and accordingly changes the Raman cross-section of the molecule. The direct bonding of the analyte to the metal can also result in new energy levels being induced within the molecule, and where these are in resonance with the excitation light, an enhancement effect can also be observed. Unlike the EM enhancement, CT enhancement is specific to the adsorbate and the metal.

1.4.3 SERS substrates

SERS requires that the substrate be structured on the nanoscale, as well as having plasmon resonance frequencies in the visible-NIR. One method is to use colloidal nanoparticles, typically of silver or gold. The synthesis method allows control over the effectiveness of the colloid as a SERS substrate, as the size and shape can affect the properties. These can be produced on a large scale making them an attractive option for many applications. A limitation with nanoparticles is the irreproducibility of the enhancement, as the nanoparticles need to aggregate to produce local hot spots. This can be overcome by selecting nanoparticles with a morphology where there are in-built hot spots, such as nanostars and nanoflowers.²¹⁻²³ Long-term stability may also be a factor, as the nanoparticles may be sensitive to light or temperature and may aggregate to an extent where they are no longer effective substrates.

Stable and reproducible nanostructured surfaces are therefore appealing options for SERS sensing. Commercially available substrates such as Klarite have been used for the detection of bioaerosols of *E. Coli*²⁴ amongst other applications. Researchers at the University of Southampton have also developed a robust and reproducible SERS platform called sphere segment void (SSV) substrates.²⁵⁻²⁷ SSVs are formed from the electrodeposition of gold over a hexagonally templated array of polystyrene spheres arranged on a microscope slide. This forms an array of smooth gold dishes that are able to diffract and concentrate the electromagnetic field leading to significant SERS enhancement factors ($\sim 10^6$ compared to conventional Raman techniques). As with nanoparticles, the properties of SSVs can be tuned. The diameter of the spheres and the thickness of the electrodeposited layer allows for control over the SERS properties.²⁸

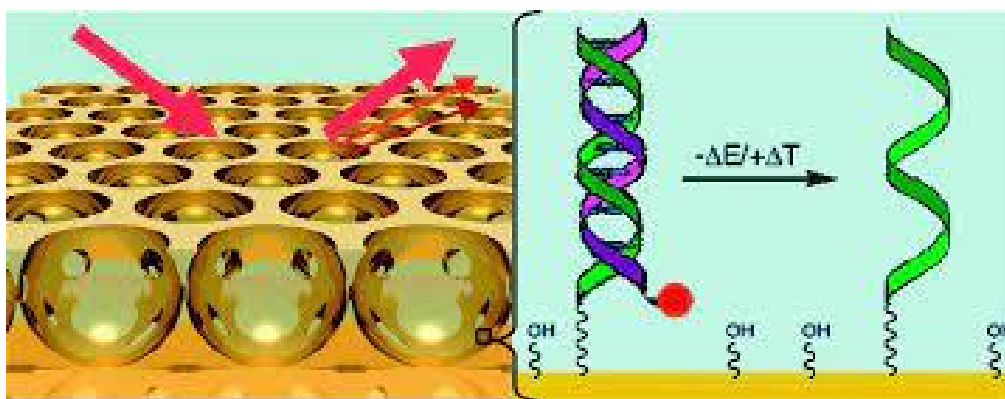


Figure 3 SERS E-melting procedure demonstrated on an SSV substrate by Mahajan *et al.* [29]. Left shows light incident on an SSV substrate, and shows Rayleigh and Raman scattered light. On the right, E-melting is depicted, showing that the labelled DNA strand dehybridises with $-\Delta E/+ \Delta T$ to leave a single strand on the gold surface.

Mahajan *et al.* describes how SSV substrates can be used to distinguish DNA mutations. A DNA strand was immobilised on the SSV surface as a capture strand. Complementary ssDNA was labelled with a fluorescent marker and the hybridisation monitored by surface enhanced resonance Raman spectroscopy (SERRS). The strands were then dehybridised by either temperature (T_{melting}) or electrochemically (E_{melting}). Differentiation between mutated and matching DNA strands was observed, with the mutated strands being removed more rapidly.²⁹

1.5 Waveguide enhanced Raman spectroscopy (WERS)

Waveguide enhanced Raman spectroscopy (WERS) occurs when an analyte is irradiated by an evanescent field, resulting in the inelastic scattering of light. An evanescent field is generated at the interface between a central waveguiding layer with refractive index n_w , and cladding layers n_s and n_c where $n_w \gg n_s, n_c$. Light from an excitation source is propagated over long distances (several cm) within the waveguide by total internal reflection. To satisfy boundary conditions, an evanescent field penetrates a short distance (~ 100 nm) into the cladding. Target molecules at the interface experience a strong electromagnetic field and scatter the light accordingly. Over long distances, the re-radiation enhancement effect builds continuously. The intensity of the electric field, re-

radiation, and a large area of irradiation all contribute to the waveguide enhanced Raman effect.

In the field of POC detection, WERS shows considerable promise. Waveguides can be extremely robust and stable over long periods of time and depending on the design – easy to fabricate. Light can be coupled without having to penetrate the sample, so the laser path is uninterrupted by interferences, and the spectra are target specific. Integrated optics reduce the need for bulk, so there is the potential for fully portable devices.

1.5.1 History of WERS

Waveguide enhanced Raman spectroscopy was first demonstrated in the 1970s by Levy,³⁰ who studied a 1 μm thick methylmethacrylate film deposited on glass. Shortly after, in a series of publications, Rabolt and Swalen demonstrated resonance enhanced WERS of Langmuir-Blodgett monolayers of Squarylene and Cyanine dyes on the surface of the Corning glass.^{31–34} Using polarisation controlled measurements, they were able to show the orientation of the dye adsorbed at the surface. This represented the first application to highly surface sensitive sensing platform. In this example, the light was confined within a waveguide layer, and the adsorbate molecules of interest were probed by the evanescent field in the superstrate.

In 1996, Kanger *et al.* showed that the sensitivity of the waveguide enhanced Raman system could be improved by three to four orders of magnitude compared to conventional Raman spectroscopy. The approach taken in this publication was to explore the impact of increasing the refractive index contrast between the waveguide and its sub- and superstrate. By using ZnO ($n = 2.0$) on SiO₂, the authors were able to obtain a Raman spectrum of a monolayer of bovine serum albumin (BSA) – the first demonstration of its kind using non-resonant techniques.³⁵ A key aspect of this work showed that spectra could be obtained with a suitable signal to noise ratio, in a short acquisition time relative to the time taken for protein adsorption, suggesting possible scope for studies on adsorption kinetics. In this work, a peak from C-H stretches was shown in the 3000 cm^{-1} region of the spectrum, which while weak, contained a shoulder showing the presence of multiple C-H environments. Other spectral features were not shown or considered for the BSA monolayer.

Chapter 1

Kanger later showed a method for determining the orientation of highly symmetric molecules on the waveguide, using polarised WERS and knowledge of the polarisability tensor of the target molecule.³⁶ Following on from the theory presented in Kanger's work, Wang showed the polarisation dependence of WER spectra originating from chemisorbed monolayers of TTCS and PTCS monolayers on a planar Ta₂O₅ waveguide. From this, he was able to deduce the adsorption angle of the molecules in the monolayers.³⁷ This was the first time that multi-featured monolayer spectra were collected in the absence of resonance effects. An additional point to note is that this was demonstrated on a planar waveguide. The fabrication of planar waveguides is relatively straightforward, but the evanescent field strength is lower for this configuration compared to others. Coucheron was able to show haemoglobin on a planar waveguide, but resonance WERS was employed in its detection.³⁸ Much recent work has focused on improving the waveguide configuration including planar, channel and rib waveguides.^{39–42} These will be briefly discussed in Section 1.5.2, and most demonstrations of these in the literature use simple, readily available solvents such as IPA and toluene, so the demonstration of monolayers on a planar waveguide is a notable advancement.^{43–48}

Dhakal *et al.* used Si₃N₄ spiral waveguides to show live measurement of DNA hybridisation, and also showed stepwise surface functionalisation with avidin.⁴⁹ In this work, the enhancement relative to conventional confocal Raman spectroscopy is shown, and there are attempts to quantify surface species according to dye labels present. Cy3 dye is used as a label for the complementary DNA (cDNA) strand, and Rhodamine Red dye is conjugated to avidin. While the spectra containing the dyes show the greatest response, there is evidence of the ability to observe typical linker chemistries close to the surface of the waveguide.

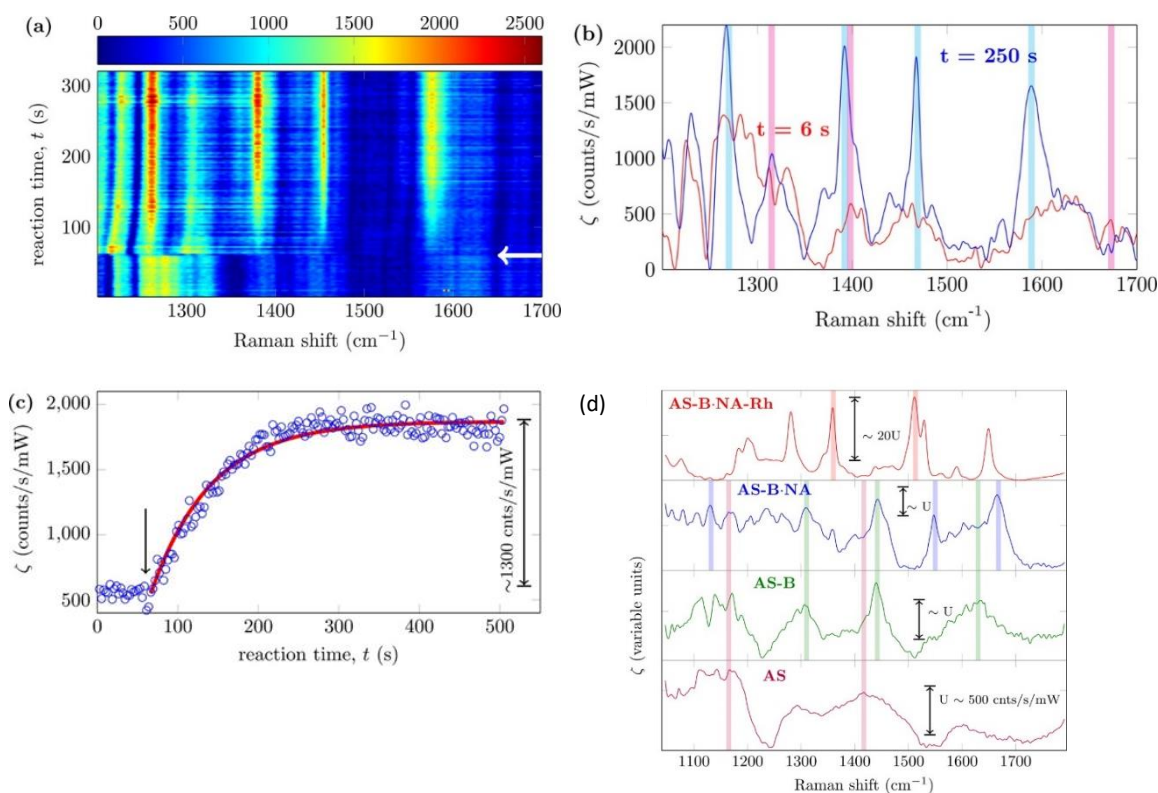


Figure 4 Work by Dhakal *et al.* [49] showing a) Raman spectrogram as a function of hybridisation time. At *t* = 60 s, cDNA-Cy3 was introduced; (b) WERS spectra after the addition of cDNA at 6 s (red) and after hybridisation at 120 s (blue); (c) The intensity of the Raman signal (counts s⁻¹ mW⁻¹) of the 1392 cm⁻¹ line of Cy3 as the hybridisation reaction occurs; (d) WERS showing the stepwise functionalisation of Si₃N₄ waveguide.

This demonstration used covalently adsorbed biorecognition molecules at the waveguide surface, able to specifically capture and detect the target molecule. In an alternative approach, Stievater *et al.* used hypersorbent polymers to capture ppb levels of gaseous threat simulant molecules such as DMMP. The group was also able to show the WERS spectra of urea and glucose which are both weak Raman scatterers.^{40,50–53} These studies and many of the most recent developments in the field use silicon nitride spirals and rib waveguides due to the increased interaction length and evanescent field intensity.

1.5.2 Fabrication considerations and choices

It is possible to tune the properties of the waveguide to optimise the efficiency and the flexibility in the application of the spectrometer. Material choices, coupling methodology, choice of collection method, excitation wavelength, waveguide thickness, and the

Chapter 1

number of propagating modes all have an effect. The optimal choices will differ depending on the type of analyte and the proposed application and will be discussed in this section.

In this work the choices have been made to optimise the system for detection of biological components– so one must consider the biocompatibility of the waveguide material. In addition, the chosen excitation wavelength must be selected to balance signal intensity while minimising autofluorescence in the biological media. 785 nm has been chosen as the excitation wavelength as the best compromise between the two factors. In a drive towards low-burden analysis, the options are considered that improve sampling methods and minimise the need for sample pre-treatment.

1.5.2.1 Wavelength

785 nm light has been chosen for this work. It is a commonly employed wavelength in Raman studies as there is limited sample autofluorescence at this wavelength, and the signal intensity remains appreciable. There is a balance to be found when considering the excitation wavelength due to the λ^{-4} dependence of the cross-section, but the shorter wavelengths result in greater background signals that may interfere with the measurement of target materials.

1.5.2.2 Coupling

There are multiple methods for coupling excitation light into a waveguide. These include high-index prisms, gratings, and end-fire coupling. These all have their benefits and limitations when considering coupling efficiency, alignment tolerance, fabrication costs, and the complexity associated with the fabrication. As the thickness of the waveguide is small (typically between 100-200 nm for single mode waveguides), it is difficult to efficiently couple the excitation laser into a propagating mode in the waveguide.

Prism coupled WERS devices have been demonstrated many times in the literature^{32,35,45} The estimated coupling efficiency using a prism is up to 30%. The high refractive index of the prism allows for coupling of the incident light into the waveguide mode with a high alignment tolerance. Integration of prism couplers into a portable device would add bulk, so may have limited use in miniaturised devices.

Grating couplers also have high alignment tolerance and coupling efficiencies of up to 50%. The incident laser can be coupled into the waveguide by illuminating the grating at the optimum angle of incidence – which is dependent on the grating depth, the periodicity of the grating, the laser wavelength and polarization, and the refractive indices of the waveguide material and the cladding. A benefit to grating coupling is that the laser may be coupled from underneath the substrate, leading to greater surface characterisation capability, and preventing non-sample scattering from material in the bulk. Microfluidics can be used to control sample delivery to the biosensor interface without interfering with the optics, thus there is an overall reduced need for sample pre-treatment when using gratings as a coupling method.

1.5.2.3 Materials

The choice of material is another important consideration when designing a WERS device. The material must be physically and chemically robust, biocompatible, and able to withstand the chemical pre-treatments that are required to provide a functional interface between the sensor and the target material. It should not degrade under normal environmental conditions such as humidity, temperature fluctuations, and light. It should also be able to transmit light through its core with minimal losses. To guide light effectively it should be a dielectric material with a large band gap. Therefore, for Raman spectroscopy, the material should be transparent in the visible to NIR range, and should have a high refractive index, which serves to sustain the intensity of pump and scattered light over long propagation distances, allowing the build-up and enhancement of the Raman effect. Other considerations include the availability and the methods for fabrication.

Raza *et. al* have investigated potential candidates for spectroscopy using 785 nm excitation, which include Si_3N_4 , TiO_2 , Al_2O_3 , and Ta_2O_5 .⁴⁶ The authors used the fundamental TE mode to investigate the Raman effect on each of the materials.

Table 1 Comparison of the refractive index, waveguide geometry, loss, and Raman collection efficiencies for four materials tested in [46]. The superstrate was air $n=0$ and excitation wavelength 785 nm.

Material	Refractive index (n_c)	Waveguide geometry ($w \times h$ (nm ²))	Loss, α_m (dB/cm)	η_{Analyte}	η_{BG}
Al ₂ O ₃	1.60	900 × 450	1.9–2.6	0.013	0.27
Si ₃ N ₄	1.89	700 × 220	2.0–3.1	0.053	0.49
Ta ₂ O ₅	2.11	500 × 220	4.8–5.4	0.13	0.61
TiO ₂	2.33	380 × 180	7.0–8.0	0.18	0.79

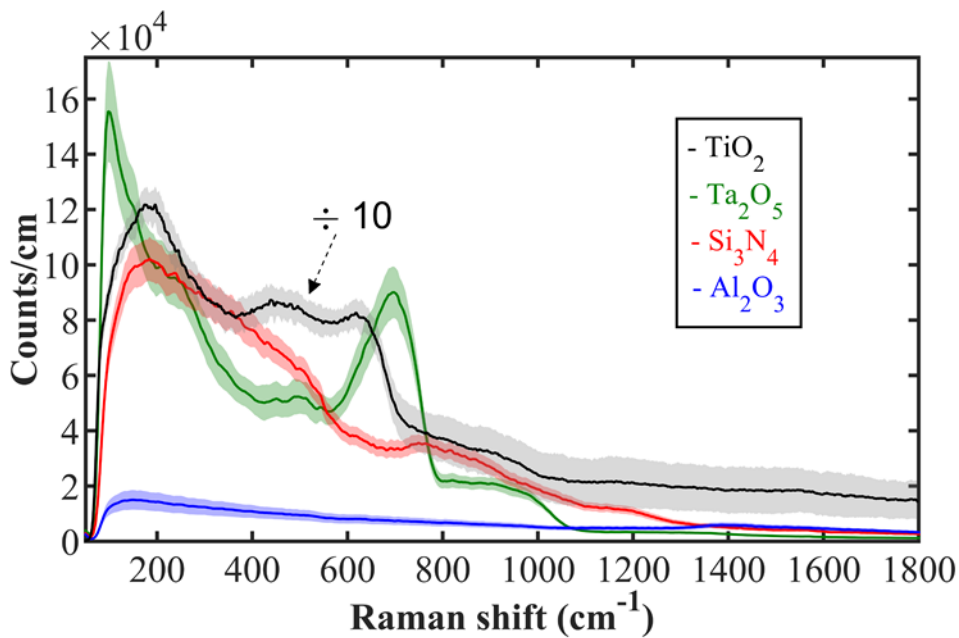


Figure 5 Spectra showing the Raman background from rib waveguides made from different materials (Raza *et al.*) This was conducted using a 785 nm laser and TE excitation. The top of the waveguide was clad in air. The spectrum of TiO₂ has had the intensity reduced by a factor of 10 for comparison purposes. [46]

These measurements were conducted in air and at 785 nm using rib waveguides. The appreciable background signal observed from TiO₂ appears to exclude it as a material for analysis at 785 nm despite its high refractive index. In a paper by Evans, WERS from a TiO₂ waveguide, clad with IPA ($n = 1.39$) using a 532 nm pump and TM polarisation was shown to be 50x more effective than Raza’s figure for unclad Si₃N₄ using 785 nm.^{46,48} While not a

direct comparison, this demonstrates the dependence of WERS on a range of variables. Lee *et al.* conducted a similar study on well-established photonic platforms, using TiO_2 , Al_2O_3 , and Si_3N_4 where the superstrate – and analyte – was toluene.⁴³ The refractive index of toluene ($n = 1.50$) is greater than air, so this study may be useful in considering the effect that analysis of organic and biological molecules may have on the waveguiding properties. The authors also considered both TE and TM polarisations. The findings were consistent with that of Raza *et al.*, TiO_2 demonstrates the worst performance, indicated by its low signal to noise ratio. TM polarisation gave spectra with improved signal to noise ratios.

Ultimately, Ta_2O_5 was chosen for this work because of its high refractive index, relatively low background, and chemical robustness.

1.5.2.4 Thickness

Optimisation of the thickness of the waveguide layer will allow for the maximum evanescent field intensity, maximum propagation distances, and maximum collection of Raman scattered light. The optimum thickness will be different for TE and TM light, so this must be taken into consideration as well. In general, thinner waveguides have stronger evanescent fields. Fabrication of thin film waveguides allows for the propagation of only the fundamental mode of each polarisation (TE_{00} and TM_{00}). This is known as a single-mode or monomode waveguide. These have several benefits over multimode waveguides such as greater intensity of the evanescent field, greater consistency in sample irradiation, less divergence, and improved coupling of Raman scattered light back into the propagating mode.

Calculations performed by the Optoelectronics Research Centre determined that for Ta_2O_5 waveguide films, and 785 nm light, the optimal thickness is around 109 nm for TE and 140 nm for TM with Si/ SiO_2 substrate and air superstrate.

1.5.2.5 Shape

The shape of the waveguide influences its function. The intensity of the electric field experienced by the analytes is one such factor, and the propagation losses and collection efficiency are additional factors to control.

Chapter 1

Figure 6 shows waveguide cross-sections with the simulated fundamental modal intensity distribution for planar, rib, and channel waveguides.⁴² In this calculation, Si_3N_4 waveguides are depicted with SiO_2 substrate and air superstrate. The TE (top) and TM (bottom) mode profiles are depicted. In this figure, red corresponds to high intensity modal distribution and dark blue correlates to a low intensity modal distribution. In the example of the TE planar waveguide depicted in (a) it can be observed that the light is heavily confined to the centre of the waveguide material. Here, only a very small intensity distribution is seen to penetrate the superstrate forming the interaction volume with the analyte. This is in contrast with (d) depicting the TM equivalent, where a greater electric field intensity can be observed beyond this interface, so the sensitivity of a device using TM slab waveguide may be greater. The electric field intensity is significantly more concentrated within channels, and around the interface of rib waveguides. For an equivalent length, the greater surface area and electric field intensity would make channel waveguides more sensitive than rib and planar waveguides.

Fabrication of a planar, or slab, waveguide is simple and integration into a device is straightforward, but the enhancement capabilities compared to rib and channel waveguides are limited. In this configuration, the analyte interacts with the evanescent field over a large area atop the waveguide material, and the Raman signal increases along the propagation length with reradiation enhancement effects. In practice, the length of the waveguide is limited by inherent loss in the material, from rough surfaces or defects, and in the length of waveguide chip that the proposed sensor can support. For a feasible portable device, this may be limited to several centimetres.

The manufacture of rib and channel waveguides is more challenging, and care must be taken to minimise roughness that would increase the losses. Otherwise, the benefits to signal maximisation should not be ignored. Rib waveguides confine light in two dimensions and can be implemented into spirals to greatly increase the interaction length if losses can be controlled.^{49,50} Channel waveguides can be designed to maximise the electric field within the analyte space, minimising background signals from the waveguide itself, but the width of the channel may limit mass transport.

For simplicity, only planar waveguides are used in this work, with the understanding that other geometries may produce better results, and that fabrication of these in the future is not a prohibitive step.

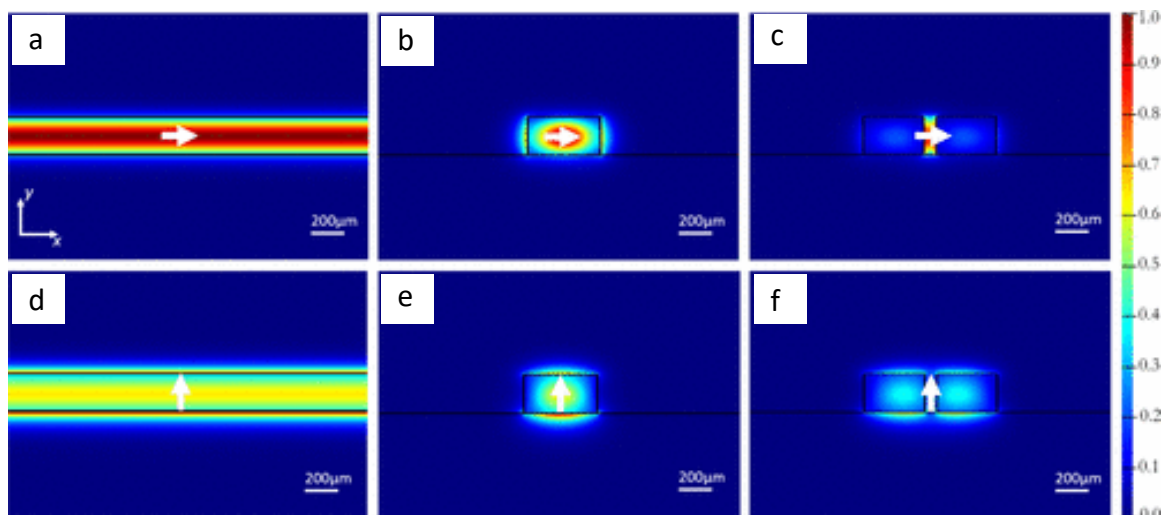


Figure 6 Cross-sections for various waveguide configurations overlaid with the simulated fundamental modal intensity distribution for planar (a, d), rib (b, e), and channel waveguides (c, f). TE (top) and TM (bottom) polarizations have been calculated. The planar waveguide exhibits pure TE and TM modes, while the rib and channel waveguides exhibit quasi-TE and quasi-TM modes. The arrows indicate the major E -field direction. [42]

1.5.2.6 Signal collection

As the scattered light will be shifted from the incident wavelength, the collection method must be capable of capturing a range of wavelengths. Using toluene as an analyte, Wang *et al.* showed the 40-fold greater efficiency of collecting scattered light from the end facet of a planar Ta_2O_5 waveguide compared to the more commonly used approach collecting from the top face of the waveguide.⁴⁵ Whilst increasing the efficiency of collection, an additional benefit of this approach is the improved ability to integrate end collection into miniaturised devices.

1.6 Summary of Raman spectroscopy for biosensing

SERS and WERS were the focus of this discussion, although these are not the only enhancement methods as RRS, SERRS, CARS, and TERS are also well-established methods.

Chapter 1

Though these are not the focus of this work, they can be extremely powerful in the right circumstances and have been summarised in many reviews.^{7,54,55} With SERS, a tremendous impact on biosensing advancements has been made. Typical enhancement factors of 10^6 - 10^7 are observed, and this can be pushed in excess of 10^{10} allowing single molecule detection where additional enhancements are taking effect. Most SERS methods require bulky and expensive equipment, operated on an optical bench for alignment purposes. Additionally, the reproducibility of SERS substrates remains a limiting factor, particularly in the case of nanoparticles. This can make it difficult to implement in a point-of-care setting.

WERS has the potential to be able to be implemented into a portable and cost-effective device. Whilst monolayer, or low concentration detection using this method is currently less developed than SERS, it is clearly a promising alternative. The large interaction volume and the intense excitation field originating at the surface of the waveguide itself increase the sensitivity of this method. Characterisation of analyte orientation is possible using polarization-dependent measurements, which could give more information than is available using SERS. The laser can be fixed at an angle to couple light into the waveguide using a grating and the collection optics can also be fixed. This means the user can simply add the waveguide to the spectrometer without having to focus on a particular spot using a microscope, which can be particularly challenging if the substrate is immersed in liquid. That is why this work – from a chemical perspective – focuses on altering the surface chemistry of the waveguide to give an adaptable platform capable of immobilising chosen biological elements.

1.7 Thesis structure

This work is part of a collaboration both within the University of Southampton, Southampton General Hospital (SGH), and the Defence Science and Technology Laboratory (Dstl). Researchers within the Optoelectronics Research Centre (ORC) at the University of Southampton were responsible for the theory, knowledge, construction, and optimisation of the WERS apparatus and sample chips. Researchers at SGH were looking for a platform that could be used in detecting *Bordetella Pertussis* – the causative agent of Whooping Cough – from clinically collected samples. This provided the DNA side of the project, where detection could be achieved through the hybridisation of capture and

target ssDNA. Dstl, as iCASE sponsor, was responsible for work related to using antibodies and immunoassays for detection of potential biological threat agents such as *Yersinia Pestis*. Both extra-mural partners had the aim of detecting the presence of disease in its early stages using a flexible platform, ensuring that an infected person could be treated more effectively and potentially limiting the spread of disease.

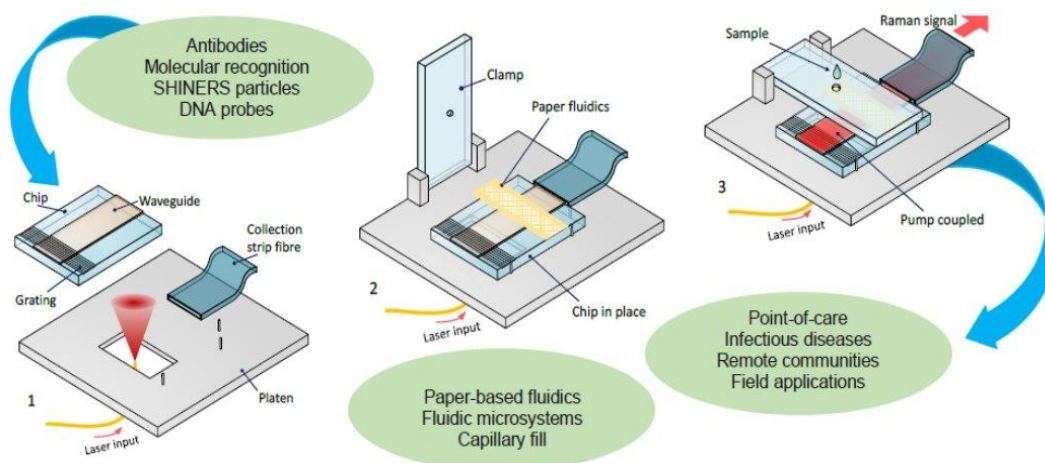


Figure 1: 1 Select chip; 2 Insert chip & fluidics; 3 Present sample; 4 Read answer

Figure 7 Project vision. The waveguide chip is shown as part of the device, including the biorecognition layer, microfluidics, and the laser coupling path.

The rest of this thesis will look at establishing a suitable surface chemistry for the immobilisation of recognition elements on the waveguide surface, assessing the suitability through analytical measurements. Work will lead towards establishing a standard for which to compare WERS spectra to in future measurements and enable the determination of detection limits and calibration. Plasmonic enhancement will also be investigated, before the culmination of the thesis in an immunoassay to demonstrate the effectiveness of the technology and its potential for further research and adoption in the POC field.

Chapter 2 will outline the methods and apparatus used in the generation and analysis of data.

Chapter 3 will explore the functionalisation of tantalum pentoxide (Ta_2O_5) substrates with organic phosphonic acid derivatives, and the effect that functionalisation has on the surface properties of the substrate. Approaches to biofunctionalization are also investigated using a bottom-up approach and attaching groups with a specific biological function to functional groups present on the phosphonic acid monolayer. The second part

Chapter 1

of the chapter will look at characterising monolayers of aromatic phosphonic acids using waveguide enhanced Raman spectroscopy. The prospect of using WERS to investigate monolayer orientation will be discussed.

Chapter 4 looks at establishing benzyl alcohol as a standard analyte for Raman spectroscopy amongst other common laboratory solvents, determining the Raman cross-sections of each, and comparing the measured results with computationally derived density functional results. Further proof will be provided by the inclusion of deuterated isomers. The second part of the chapter will use the WERS apparatus to validate the findings, looking at spectra from benzyl alcohol and deuterated benzyl alcohol.

Chapter 5 investigates different substrates for SERS, the enhancement factors achieved for different analytes on a nanostructured gold surface, silver nanostar colloids, and a combined effect. Silver nanostars are treated with different chemistries and Raman reporters and then functionalised with antibodies to assess the use of silver nanostars as Raman tags in immunoassays. A proof-of-concept paper fluidic device is used with the nanostructured gold SERS substrate to demonstrate a low-burden method for low volume sample introduction and pre-treatment.

Chapter 6 aims to provide a cohesive summary of the work involved in each chapter and suggests plans for future work with predictions of long-term impacts and direction.

Chapter 2 Methods

2.1 SERS substrate preparation

2.1.1 Sphere segment void (SSV) substrates

Sphere segment void substrates were prepared according to the method by Bartlett. Briefly, microscope slides, vapour deposition coated with a 10 nm chromium adhesion layer and 200 nm gold were cut into 13 x 19 mm sections. The substrates were cleaned by sonication in ethanol, followed by a short immersion in gold surface cleaning solution and then rinsed in ethanol, water and ethanol again. To improve the hydrophilicity of the substrate, the chips were left to soak in a 10 mM cysteamine solution for 48 h, followed by rinsing in ethanol, water and ethanol. The substrates were left to air dry. A thin layer cell was constructed using a trapezoid-shaped parafilm spacer and a glass cover slip on top of the gold substrate. 10 μ L of monodisperse polystyrene sphere solution (1.8%) was injected into the thin layer cell. The substrates were incubated at 14 $^{\circ}$ C for 48 h, tilted to 15 $^{\circ}$. This enabled the formation of a uniform hexagonally packed monolayer of polystyrene spheres forming a template for electrodeposition.

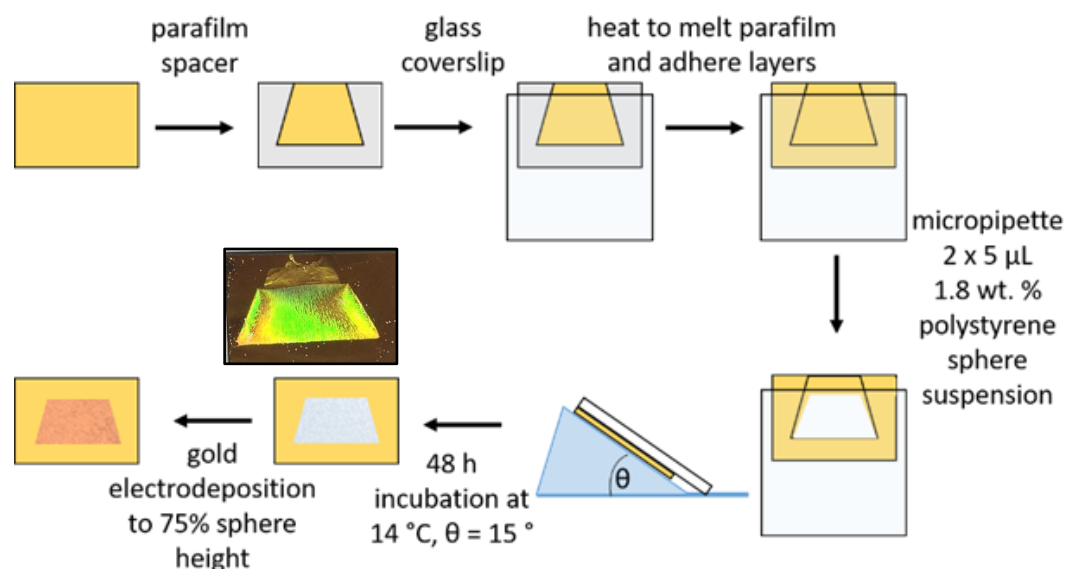


Figure 8 Diagram showing the stepwise process of producing SSV substrates with 600 nm polystyrene sphere standards. Inset photograph showing the opalescent surface produced from the array of polystyrene spheres.

Chapter 2

Gold was electrodeposited around the polystyrene template from a commercial plating solution and brightener. The potential was held at -0.72 V until the requisite amount of charge had passed, a factor dependent on the sphere size, template area and desired film height. Previous research had demonstrated that a film height between 70-80% that of the height of the 600 nm template was the most useful for SERS using a 785 nm laser, so the film thickness was grown to around 480 nm – estimated from the diameter of the cavities observed with SEM imaging.

The final step involved removing the template; this was achieved by soaking the substrates in DMF for 48 h, followed by rinsing in ethanol, water and ethanol and repeating this process twice. The resulting structure was a hexagonal array of gold dishes, characterised using SEM. Visually, the substrate appears as an opalescent surface, ranging from green to red depending on observation angle.

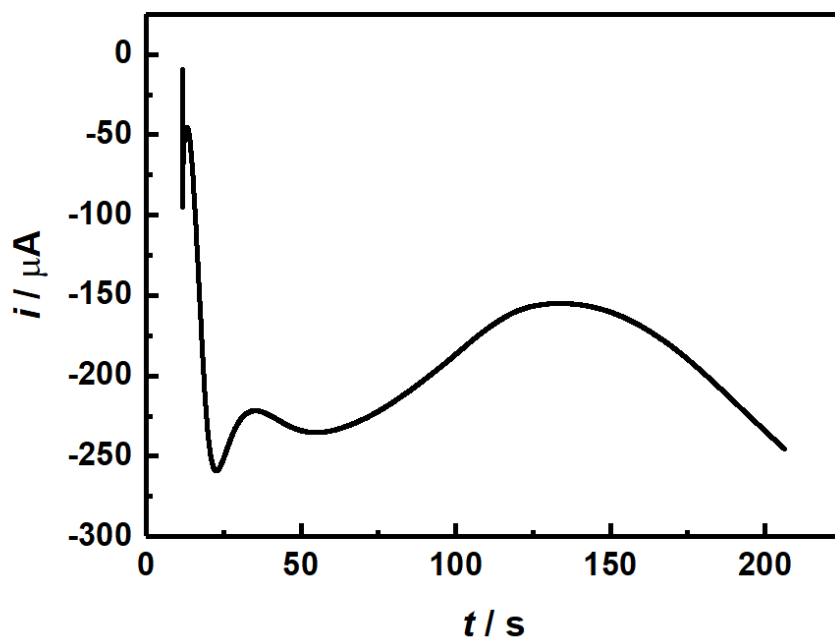


Figure 9 Chronoamperogram showing the typical response curve for the electrodeposition of gold around the 600 nm polystyrene sphere template. Potential -0.72 V.

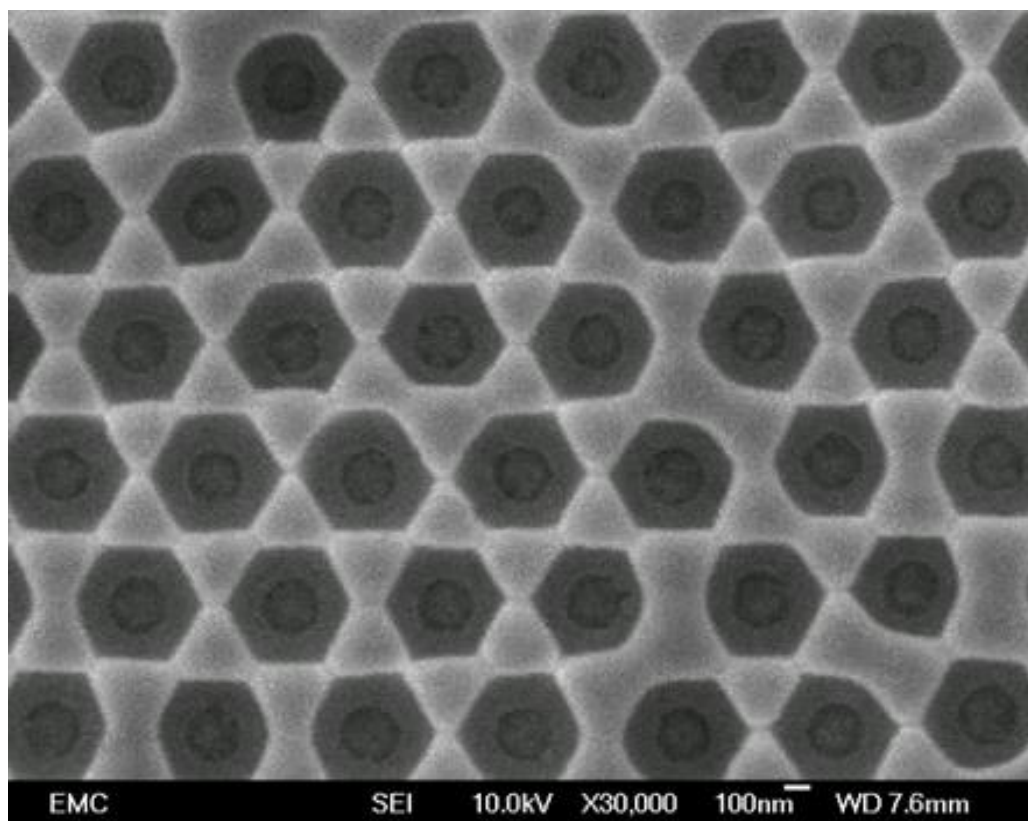


Figure 10 SEM image of an SSV substrate with 600 nm sphere template. Accelerating voltage 10.0 kV, 30000 \times magnification, scale bar 100 nm.

2.1.2 Silver nanostars (AgNS)

Silver nanostars were prepared according to the method described by Garcia-Leis *et al.*,²¹ under the guidance of Dr M. S. Zalaffi. In a 10 mL glass vial, sodium hydroxide (500 μ L, 5×10^{-2} M) and hydroxylamine (500 μ L, 3×10^{-3} M) were mixed under magnetic stirring at 700 rpm for 1 min. An aqueous solution of AgNO_3 (9 mL, 1×10^{-3} M) was added to the mixture dropwise, forming a grey colour. After 5 min, trisodium citrate (100 μ L, 4.5×10^{-2} M) was added and the suspension stirred for a further 15 min. The resulting colloid was dark grey in colour with pH 6.5. The following describes the analysis of three batches of silver nanostars. UV-visible spectrometry showed $\lambda_{\text{max}} = 377.7 \pm 0.7$ nm with a tail extending into the NIR region, confirming the presence of silver nanostars. The concentration of the prepared colloids was estimated using the Beer-Lambert law assuming $\epsilon = 1546$ as 3.99 μ M, 3.36 μ M and 4.44 μ M.

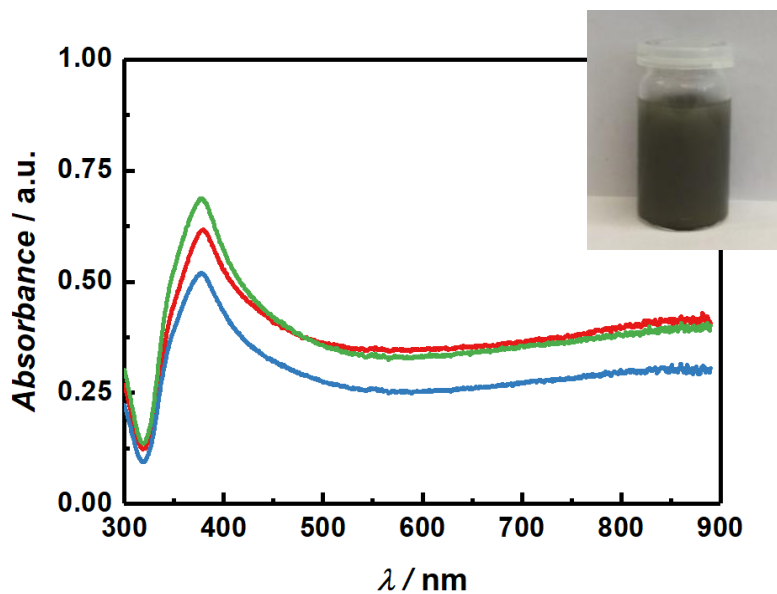


Figure 11 UV-vis spectra of three AgNS colloids showing absorption maxima at 380 nm and displaying a large tail in the visible to near IR region. Inset photograph of AgNS colloid.

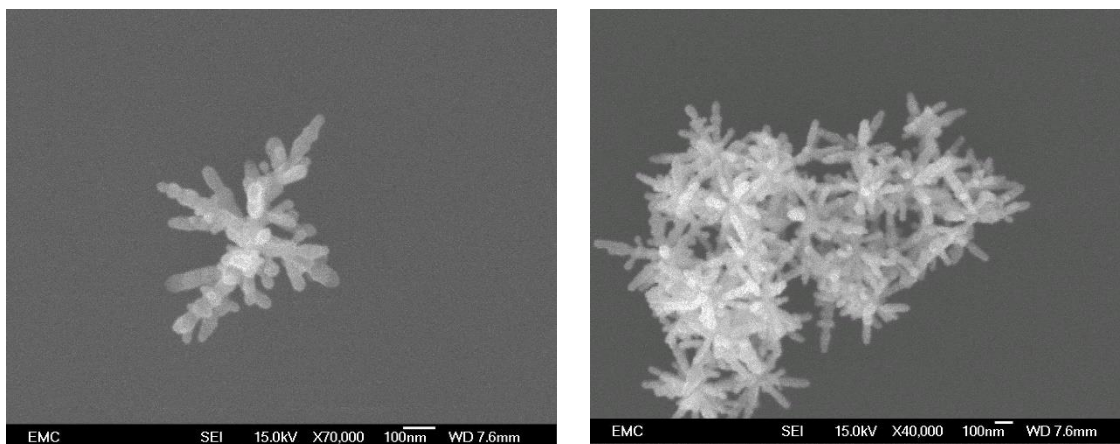


Figure 12 TEM images of silver nanostars. Left: showing an individual nanostar (accelerating voltage 15.0 kV, 70000× magnification, scale bar 100 nm); right: showing a cluster of nanostars (accelerating voltage 15.0 kV, 40000× magnification, scale bar 100 nm). Images collected by Dr A. Marti-Morant.

2.2 Surface modification strategies

2.2.1 Gold SSV functionalisation

Thiol SAMs on gold SSVs were formed by immersing the substrate in a 10 mM ethanolic solution of the thiol. The substrates were immersed for 48 h. Unbound, excess thiol was washed off by a thorough rinsing of the substrate with ethanol, water and repeated with ethanol before being dried in a stream of Ar.

2.2.2 Functionalisation of AgNS

For the enhancement factor determination 1 mL AgNS were mixed with 1 μ L of a 10 mM ethanolic solution of the thiol and incubated in the dark with agitation for 48 h.

For the antibody conjugates:

1 mL AgNS was centrifuged for 10 min at 6000 rpm, and the pellet resuspended in 1 mL water. This process was repeated three times. 0.1 mM solutions of thiobenzonitrile (TBN) and mercaptohexadecanoic acid (MHDA) were prepared in ethanol and mixed in equal volumes. 35 μ L of the TBN-MHDA mixture was added to 1 mL AgNS and then incubated in the dark with agitation for 48 h. The thiolated AgNS was centrifuged for 10 min at 6000 rpm and resuspended in 1 mL PBS three times.

1-Ethyl-3-(3-dimethylaminopropyl)carbodiimide (EDC) was prepared as a 40 mg/mL solution in 0.1 M MES buffer. *N*-hydroxysuccinimide (NHS) was prepared as a 110 mg/mL solution in 0.1 M MES buffer. 5 μ L of each was added to the thiolated AgNS, incubated in the dark with agitation for 20 min. The resulting mixture was centrifuged at 4000 rpm for 5 min, the supernatant removed, and the pellet resuspended in 1 mL PBS.

13 μ L, 2 mg/mL rabbit anti-BSA antibody was added to the AgNS and incubated with shaking for 2 h. 5 μ L hydroxylamine solution (50 wt. % in water) was added. The AgNS were centrifuged twice at 4000 rpm for 5 min, removing the supernatant and resuspending the pellet in 1 mL PBS.

The above outlined procedure was also used for the 5,5-dithio-bis-(2-nitrobenzoic acid) (DTNB) method. 0.1 mM DTNB solution was prepared in water, incubated with AgNS and activated towards the antibody as described.

2.2.3 Preparation of AgNS in SSV cavity substrates

The thiolated SSV substrate was immersed in the silver colloid and incubated with agitation overnight. The SSV substrate was removed, gently rinsed with water, and allowed to dry in air.

2.2.4 Functionalisation of Ta₂O₅

Prior to modification, Ta₂O₅ samples were cleaned and made hydrophilic by sonication for 15 min in a 0.5 M, 2:1 ethanol: water solution of K₂CO₃. This pre-treatment step served to form a clean and hydroxyl-rich Ta₂O₅ surface, allowing a condensation reaction to take place between the surface and the phosphonic acid molecule.

Two preparation methods for the phosphonic acid monolayers were employed.

In the immersion method, the phosphonic acid derivative was dissolved in the solvent and the freshly prepared Ta₂O₅ substrate was submerged for set lengths of time.

In the tethering by aggregation and growth (T-BAG) method, the clean Ta₂O₅ substrate was suspended vertically in a microcentrifuge tube containing solutions of the phosphonic acid. The solvent was left to evaporate for 1 week.

After forming the initial monolayer, the substrates were gently rinsed with the chosen solvent and were then transferred to an oven at 140°C for 48 h to allow the formation of covalent bonds between the phosphonate oxygen molecules and the Ta₂O₅ surface. The substrates were sonicated for 5 min each in the chosen solvent, then in the ethanolic K₂CO₃ solution and finally rinsed with water to remove non-chemisorbed multilayers and other possible contaminants.

2.3 Raman measurements

2.3.1 Assignment of spectra

This work uses the Wilson⁵⁶ notation to assign and describe the vibrational spectra of substituted benzenes. This method is commonly adopted in the relevant literature. This approach describes the normal modes of benzene in a consistent manner and is depicted in Figure 13, page 30. Extension of this notation to describe substituted benzene changes

the symmetry and affects the degeneracy of a number of the normal modes, and the vibrational frequency for a given mode can be predicted within a range taking into account the effect of substituent mass and the electronic effects. This notation has been used throughout this work for consistency, with the understanding that there are drawbacks when describing the normal modes and assigning spectra of substituted benzenes in this manner. Existing research that involves the assignment of the vibrations of substituted benzenes will often use the Wilson notation, or the notation described by Gardner and Wright.^{57,58} This alternate labelling scheme also provides information on the vibrational motions which the authors have detailed for monosubstituted⁵⁷ benzenes and *ortho*-disubstituted⁵⁸ benzenes.

2.3.2 SERS measurements

Except where otherwise stated, Raman spectra were recorded with a Renishaw InVia Raman microscope equipped with a 50× objective with NA = 0.75 in the backscattered configuration. Samples were irradiated using a 785 nm laser over one acquisition of 10 s. The selected laser power was dependent on the substrate and analyte, and spectra have been normalised to Counts $\text{mW}^{-1} \text{s}^{-1}$. To ensure reliability, measurements were taken across multiple spots on the same substrate.

2.3.3 Cross-section determination

The Raman cross-section was determined by filling a quartz cuvette (1 cm path length) with the analyte liquid and placing the cuvette in a 3D-printed custom holder to ensure the same measurement conditions across the different analytes. The samples were irradiated with a 785 nm, 10 mW laser for one scan with 10 s acquisition time, using a 5× objective with NA = 0.12. Five repeats were conducted.

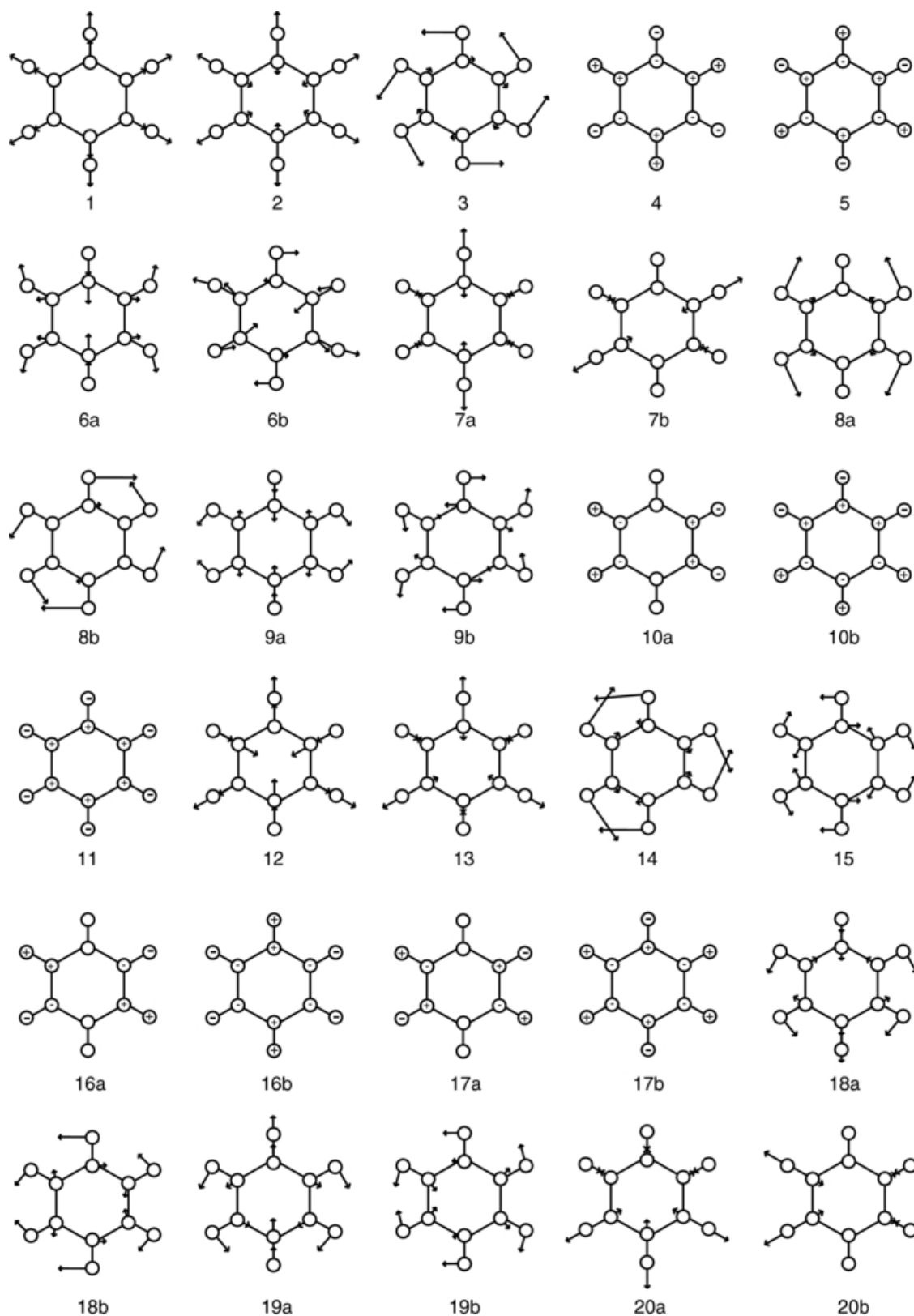


Figure 13 The Wilson modes of benzene as depicted by Gardner and Wright [57]. Arrows indicate atomic motion, the + symbol indicates movement out of the plane and towards the reader, and the - symbol depicts the opposite. Modes that are degenerate are shown by the labelling a and b.

2.3.4 WERS measurements

The WERS instrument consists of a 785 nm MatchBox laser, Wasatch Photonics WP 785 ER spectrometer, Rayleigh rejection filter, cylindrical lens, Ta₂O₅ waveguide, and a collection fibre assembled as shown in Figure 14. For the liquid WERS measurements, a 2 µL droplet was placed in the path of the guided beam with a 5 s acquisition time. Monolayer measurements were conducted by irradiating the sample for several minutes.

Prepared by Dr Ettabib, 110 nm Ta₂O₅ films were deposited on SiO₂ substrates using RF sputtering. The substrates were then annealed. At 633 nm, the refractive index of the Ta₂O₅ film is 2.12, and the loss is approximately 2-3 dB cm⁻¹. These figures are not expected to be too dissimilar for 785 nm. Gratings were written using e-beam lithography, etched through ion-beam milling and the substrates underwent plasma-ashing to remove the remaining photoresist. For the TE waveguide used in this work, the grating period is 571 nm with an etch depth of 42 nm.

785 nm light at 40 mW is coupled into the grating of the TE waveguide chip at 8° with 42% efficiency.

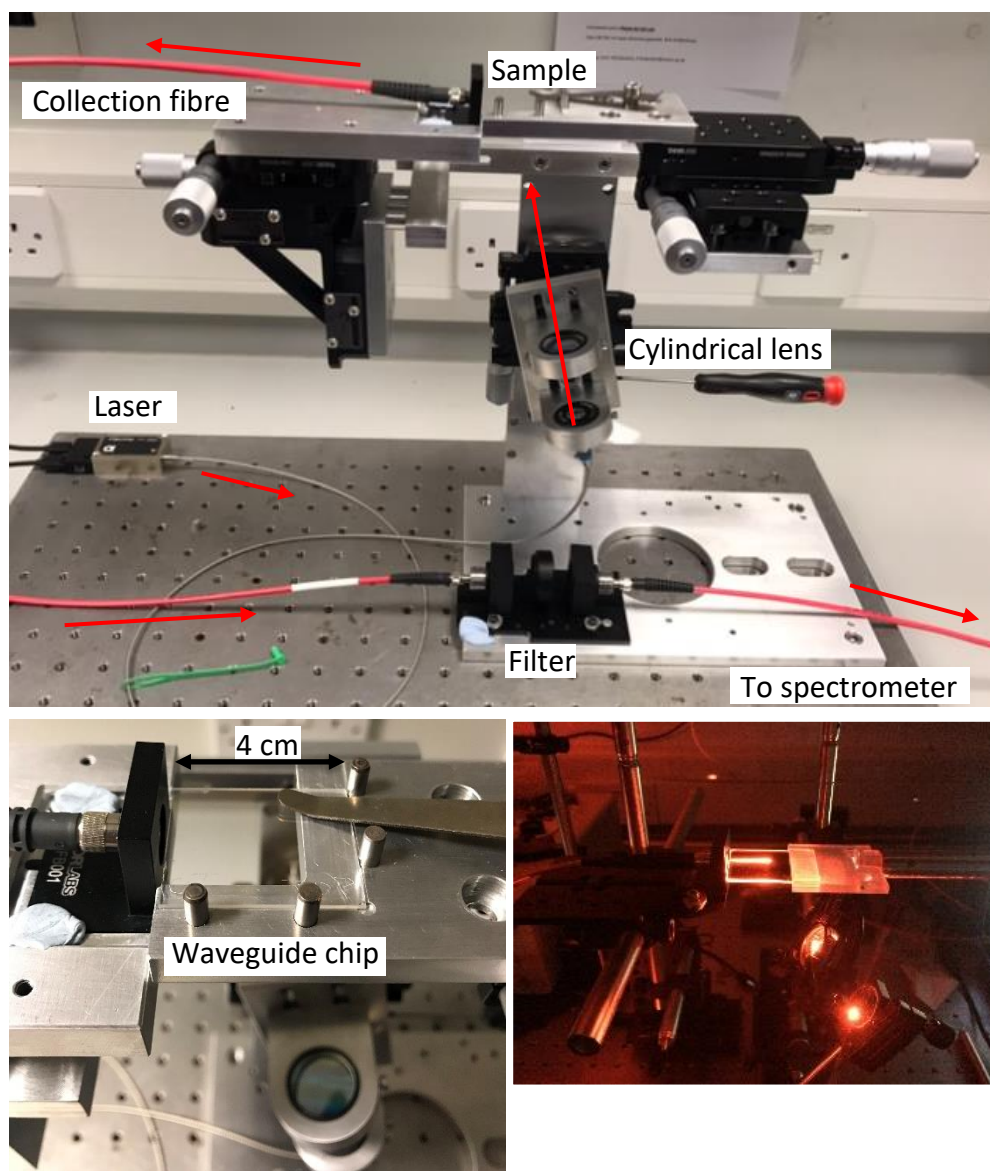


Figure 14 Photograph of the WERS apparatus showing the overall set-up, a close-up of the waveguide chip, and an example of 637 nm light being coupled into the waveguide for visualisation of the light path.

2.4 Additional characterisation methods

2.4.1 Contact angle measurement

Contact angle measurements were recorded on a Krüss DSA100 drop shape analyser (DSA). For static measurements, a 1 μL droplet was lowered onto the substrate surface. The angle formed between the water droplet and the substrate was measured using the circle-fitting tool on the Krüss software. The average value was taken from multiple

measurements on the same substrate where possible, or from single measurements taken on substrates exposed to the same chemical treatments.

For dynamic contact angle analysis, the substrates were mounted onto a glass slide using double-sided tape. The glass slide was fastened to the stage. A 5 μL droplet of water was placed on the surface and the sample stage was slowly tilted to 90° . The point at which the droplet began to move down the substrate was recorded as a photograph and the contact angle at the advancing and receding ends were measured.

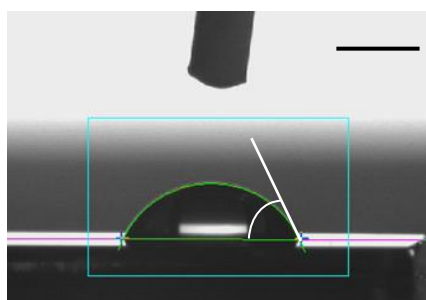


Figure 15 Contact angle measurements using Krüss DSA where the baseline is defined by the pink line, the droplet outlined by the green line and the region selected in the blue box. The contact angle is shown between the white line and the baseline.

2.4.2 Scanning electron microscopy (SEM)

SEM images were recorded on a Philips XL30 environmental scanning electron microscope with an accelerating voltage of 30 kV.

2.4.3 Transmission electron microscopy (TEM)

TEM images were collected using Hitachi HT-7700 TEM microscope.

2.4.4 Fluorescence microscopy

Fluorescence images were recorded using the Leica SP8 Lightning confocal microscope. Alexa-Fluor488 was used as the dye to allow for maximum resolution and imaging capability.

2.5 Wax printed fluidics

Wax-printed patterns were designed using Coreldraw and printed on Whatman No.1 chromatography paper using a Xerox ColorQube 8800DN wax printer. The paper was then heated to 110°C on a hot plate to allow the wax to permeate the paper and form a hydrophobic boundary. Chemical modification or pre-loading of the reactant was typically achieved by loading the area with a suitable buffer followed by the reagent of choice. The paper was allowed to dry before adding the sample to the inlet zone and lateral flow was used to carry the sample to the functionalised substrate surface.

2.5.1 Glucose tests

15 μL of glucose oxidase enzyme (5 mg mL^{-1}) in PBS (pH 7.4) was added to the incubation zone of the wax-printed paper and allowed to dry. The paper was then clamped against a 4-MPBA modified SSV substrate so that the outlet zone was in contact with the SERS-active surface. 30 μL of glucose (10 mM in PBS) was added to the incubation zone, which represents a high concentration within the clinical range. The glucose solution reacted with glucose oxidase to produce H_2O_2 . H_2O_2 produced from the enzymatic reaction was able to flow through the paper by capillary action and react with the 4-MPBA SAM. In each case, the reaction was given in excess of 1 hour. After the waiting period, the paper was removed from the substrate and the substrate was rinsed with PBS. The substrate was then dried under a stream of Ar before measuring the SERS spectrum.

2.6 Density functional theory (DFT)

In this work, Gaussian 9 and Gaussian 16 were used to perform the calculations.

GaussView6.1 was used to visualise the target molecule and input initial structures.

Unless stated otherwise in the text, the hybrid functional B3LYP was used with the basis set 6-311G ++(d,p).

2.6.1 DFT calculation of spectral properties

The molecular geometry of the target molecule was first optimised using Gaussian 16 at the B3LYP level of theory, using the basis set 6-311G++(d,p). The optimised structure was then subjected to a frequency calculation at the same level of theory, including Raman

calculations. This calculation predicted the Raman spectra, and for each vibrational mode, provided values for the reduced mass, Raman activity, depolarisation ratio and the atomic displacement. The frequencies given were scaled by 0.9668 to account for the exchange correlation overprediction inherent to DFT. Polarizability derivatives were given in the output as a string of numbers. These were tabulated (see Appendix A) and used to generate polarizability tensors.⁵⁹

Chapter 3 Phosphonic acid functionalisation

3.1 Overview

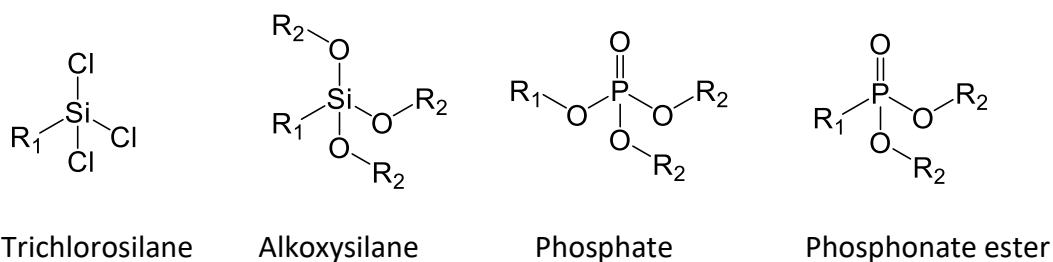
In this chapter, the effect of self-assembly conditions on the growth of octadecylphosphonic acid and phenylphosphonic acid SAMs will be investigated using Ta_2O_5 as the substrate. Ta_2O_5 is an optically dense dielectric that is transparent in the visible to NIR region of the electromagnetic spectrum. These properties make it a suitable material for a waveguide core. Understanding the degree of modification and the extent that the experimental conditions play a part in the molecular self-assembly is important in developing robust, well-packed and reproducible surfaces that can be used to immobilise biological receptors. The quality of the SAM will be assessed using water contact angles and contact angle hysteresis, whilst acknowledging that conclusions drawn could be supported by further analysis such as ellipsometry, AFM and XPS. The second half of the chapter will study the polarisability tensor and the information that can be learnt on the molecular orientation using polarised WERS.

3.2 Functionalisation of Ta_2O_5 with phosphonic acids

Self-assembled monolayers provide significant molecular control over surface properties, which can be achieved with minimal cost and preparation. The most studied system is that of thiols on gold and other noble metals,^{11,60} which is very useful in changing the work function and biocompatibility of the surface but the weak Au-S bond and monodentate configuration limit this somewhat in terms of long term stability. The conductive properties and opacity of gold make it an unsuitable material for the waveguides in this work. Metal oxides can react with a number of chemical groups including silanes, phosph(on)ates, carboxylates, unsaturated hydrocarbons and catechols with varying levels of success and stability. Many metal oxides are compatible with trichlorosilane and triethoxysilane molecules, where the Si head group reacts rapidly with surface hydroxyls. A series of condensation reactions occur with hydroxyl species forming multiple covalent bonds with the surface and forming crosslinks between adjacent silane molecules. This results in the formation of densely packed monolayers. Organosilanes are extremely sensitive to the solvent polarity, the solvent dryness, and the amount of

Chapter 3

adsorbed water on the substrate and can self-condensate to form disordered multilayers in non-ideal conditions. Some silanes are also vulnerable to hydrolysis and can be removed from the surface within a matter of hours. Despite these limitations, organosilanes have shown success in forming monolayers on biological implants and sensors,⁶¹ corrosion inhibitors, and in superhydrophobic textiles amongst many other uses.



R₁ = alkyl or aryl, contains the terminal functional group, R₂ = alkyl, aryl or hydrogen. Imparts the surface properties and functionalisation.

Figure 16 Self-assembling molecules that have been used to functionalise metal oxide surfaces, which include trichlorosilanes, alkoxysilanes, phosphates, and phosphonate esters.

Phosphates and phosphonates are a newer class of self-assembling molecules used where stability is required and form strong bonds with a range of metal oxides.^{62–71} As with silanes, these groups are able to form multiple covalent bonds with the surface through a heterocondensation reaction. However, phosph(on)ate molecules tend to form more robust SAMs and are less prone to multilayer formation. A number of methods to form phosph(on)ate SAMs have been investigated and include immersion, tethering by aggregation and growth (T-BAG),^{72–74} organosols,⁷⁵ adsorption from supercritical CO₂,⁷⁶ dip-coating,⁷⁷ and aerosol spraying.^{78,79} The chemisorption of phosphonic acids has been shown to be strongly dependent on the oxide type, as well as temperature, pH, concentration and solvent.^{64,79–81} Figure 17 shows the condensation reaction for phosphonic acids and metal oxide surfaces. Route 1 shows the pathway for Lewis acidic oxides and route 2 shows the pathway for Lewis basic oxides. Work by the Gooding group has shown the effect of solvent polarity and temperature on the formation of some aryl and alkylphosphonic acids on indium tin oxide (ITO) and showed that polar solvents hindered SAM formation by outcompeting the phosphonic acids for ITO binding sites.⁶⁴ A

large number of hydroxyl groups are required on the oxide surface for efficient functionalisation.⁸² The packing density of phosphonic acids has been reported as 3.5-4.7 groups nm⁻² which is in line with the density observed for analogous silanes.⁸³

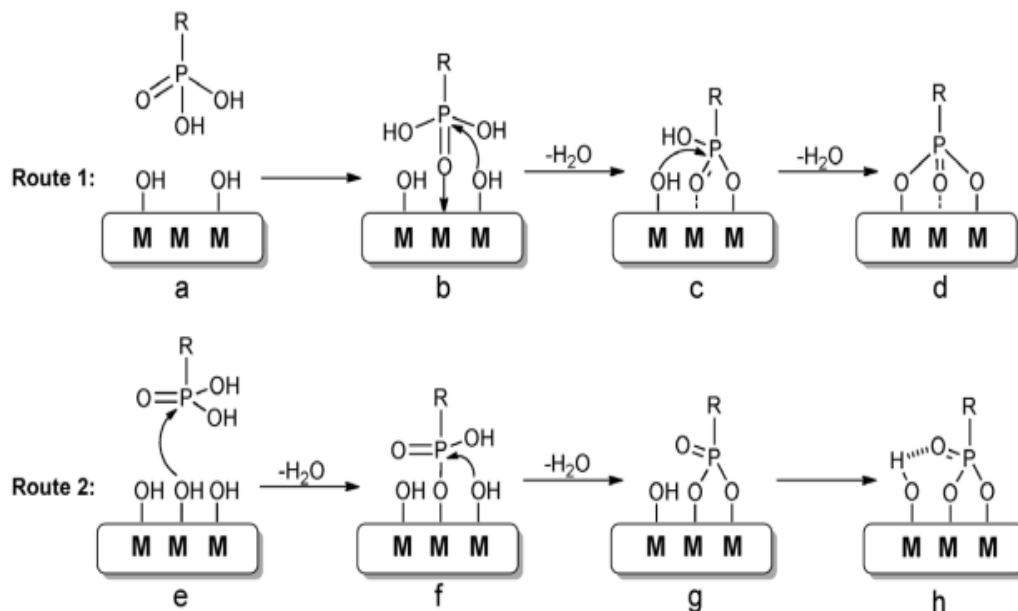


Figure 17 Mechanism of phosphonic acid attachment to Lewis acidic (top) and Lewis basic (bottom) oxides. Image from [89].

Reactive terminal groups have been used to graft receptors for biofunctionalisation. With the phosph(on)ate headgroup anchoring the molecule to the oxide surface in a tails-up configuration, there is a choice of terminal functional groups that have been demonstrated. This includes the amino group,^{64,84,85} carboxyl group,^{64,86-88} and a constrained triple bond for azide click chemistry.⁸⁹ A review by Queffelec provides some excellent further examples.⁷⁶ Some functional groups are not compatible with phosph(on)ates – Hotchkiss has described the difficulty in synthesising phosphonic acid epoxides, which is a readily used moiety in homologous silane SAMs.^{86,90-92} Mixed SAMs have also been formed where one moiety is responsible for providing antifouling behaviour, and the other is used to immobilise the receptor. Using phosphonic acids on ITO, Lu *et al.* formed hydrophilic oligoethylene glycol layers functionalised with either CH₃ or OH groups.⁸⁷ Using DSC/DMAP coupling chemistry, the labelled protein BSA-Alexa647 was immobilised selectively to the OH-terminated molecules.⁸⁷ Fluorescence microscopy was used to assess the distribution of the protein at the surface as a function of the OH:CH₃ ratio.⁸⁷

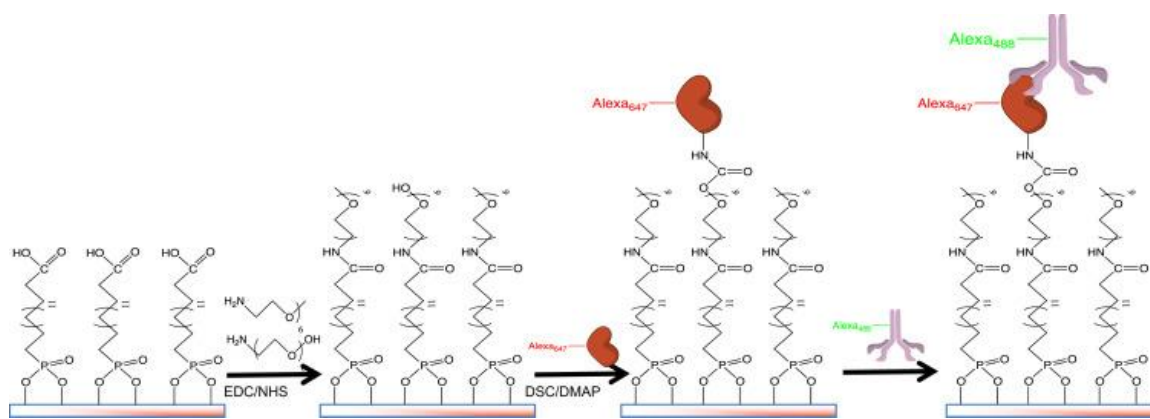


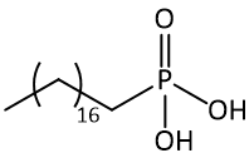
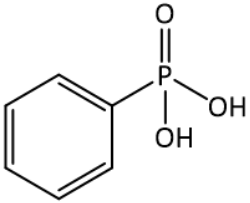
Figure 18 Stepwise biofunctionalisation of ITO with fluorescently labelled proteins. The carboxylic acid monolayer is activated using EDC/NHS coupling to form a mixed monolayer with CH₃ and OH terminal groups. DSC/DMAP is used to attach labelled BSA through the OH groups. Image from [87]

There have been few reports of phosphonic acid monolayers on Ta₂O₅,^{86,90,91} and none detailing any direct characterisation. Alkylphosphate monolayers on Ta₂O₅ have been characterised using a range of methods including contact angle analysis, XPS, AFM, ToF-SIMS, NEXAFS, and microdroplet density measurements.^{62,63,65,70} Using these methods has shown that alkylphosphates rapidly form monolayers with the tails-up configuration at a 30-35° tilt angle, and with the adsorbates spaced ~0.5 nm apart. The tilt angle of alkylphosphonic acids on other oxides has been reported as high as 45°.⁹³

The molecules listed in Table 2 were chosen to modify Ta₂O₅ in an attempt to observe the change in surface properties when forming a SAM from aliphatic and aromatic molecules using different methods. The long chain phosphonic acid, ODPa, has been used as a reference when determining the quality of a SAM on a metal oxide material. This is because its length enables strong intermolecular interactions and the CH₃ terminal group imparts hydrophobic character. SAM coverage can be estimated from water contact angle measurements. A more densely packed SAM will give a higher contact angle, whereas a defective SAM may allow water to penetrate the layer and reduce the contact angle. The contact angle hysteresis is the difference between the advancing and receding contact angles as the stage is tilted. A small hysteresis (< 10°) is indicative of a well-packed SAM. The contact angle measured with different terminal groups presents more of a challenge when trying to determine SAM quality as polar functional groups will interact with the water or hydrogen bond to an unknown extent. In this case, contact angle goniometry is

often used in combination with other surface techniques Two attachment methods for SAMs of phosphonates on metal oxides have been investigated: immersion and tethering by aggregation and growth (T-BAG). These have been assessed using THF and EtOH. The choice of solvent for the SAM assembly is critical, as the polarity of the solvent can affect the SAM growth.

Table 2 The phosphonic acids chosen for this study are octadecylphosphonic acid and phenylphosphonic acid. The length of the molecule, the supplier and purity of the supplied reagent are included in the table.

Phosphonic acid	Length / nm	Supplier	Purity
Octadecylphosphonic acid (ODPA) 	2.5	Sigma-Aldrich	97%
Phenylphosphonic acid (PPA) 	0.8	Sigma-Aldrich	98%

3.2.1 Immersion method

Ta₂O₅ wafers were cut into strips (1 × 0.5 cm). As received, the substrates had contaminated surfaces indicated by a contact angle of ~80°. To maximise the quality of SAM formation the substrate needed to be cleaned and hydroxylated. This was achieved using the ethanolic K₂CO₃ cleaning method described in Section 2.2.4.

The resultant contact angle of freshly cleaned Ta₂O₅ was <5°. The very low angle indicates a highly hydrophilic surface that should interact strongly with the self-assembling molecules. The freshly cleaned substrates were incubated in ODPA solutions in THF (1 mM, 0.1 mM) and EtOH (0.1 mM). After the selected length of time, the substrates were removed, rinsed with the corresponding solvent, and placed in an oven for 48 h at 140 °C.

Chapter 3

This encouraged the formation of covalent bonds between the monolayer and substrate. After removing the substrates from the oven, they were cleaned using the steps in Section 2.2.4. This was to remove any weakly bound multilayers. The water contact angle was measured on the substrates immediately after this final rinsing step.

Figure 19 shows the contact angle and hysteresis values for substrates immersed in ODPA solutions in THF (0.1 mM, 1 mM) and EtOH (0.1 mM) at 5 min, 60 min, 24 h and 1 week. After short incubation times (5 min, 60 min), the variation in contact angle and hysteresis values was large for all testing conditions, indicating poor OPDA coverage. Figure 19 demonstrates the low contact angle associated with an incomplete ODPA SAM and a very large standard deviation that can also be attributed to non-uniform coverage. With increasing immersion time, the ODPA solutions from THF showed a significant increase in contact angle, with only a small deviation in repeat measurements suggesting a more uniform SAM coverage. The contact angle hysteresis was above 10° for both THF samples, described as the cut-off point for a uniform monolayer.⁹⁴ For the ODPA SAMs formed from ethanolic solution, the contact angles remained hydrophilic with a significant deviation between results. This agrees with the idea that more polar solvents compete with the phosphonic acid by interacting strongly with the oxide, preventing uniform adsorption of the phosphonic acid.⁶⁴

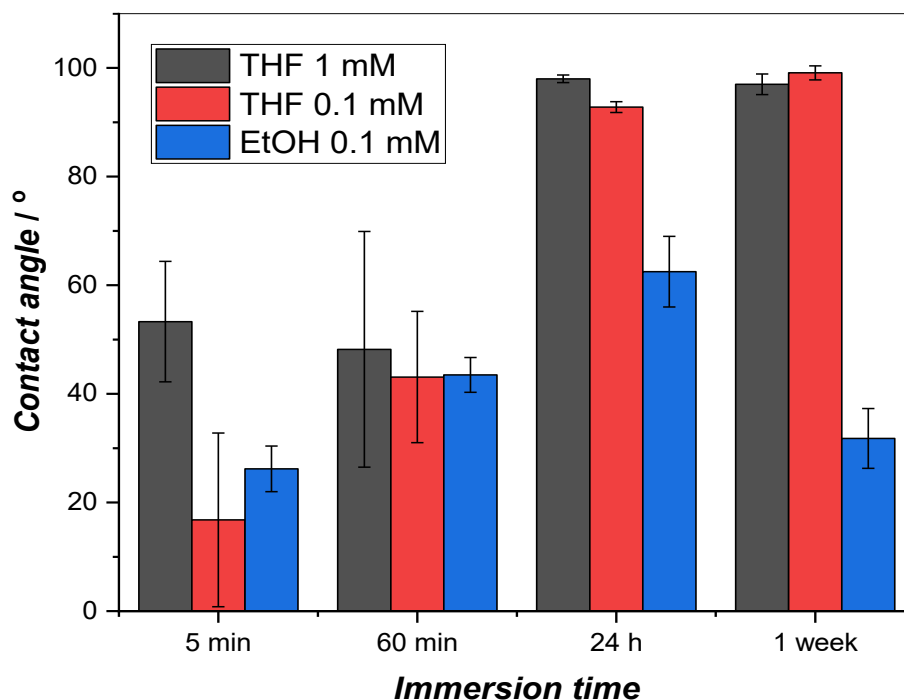
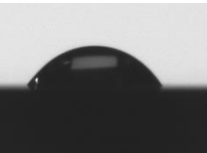
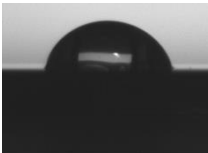
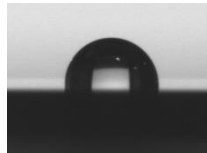
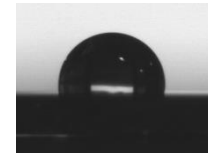


Figure 19 Graph showing the change in water contact angle with respect to the functionalisation of Ta_2O_5 with ODPA. The contact angle with the error bar showing standard deviation is shown. At least three repeats were conducted for each measurement condition.

A representative image of the water contact angle analysis for each experimental condition is included in Table 3. Only one image is presented for each condition, with the understanding that, particularly with shorter immersion times, the standard deviation is significant.

Table 3 Pictures of 1 μ L droplets of water on Ta_2O_5 substrates after being subjected to ODPA solutions for 5 min, 60 min, 24 h, and 1 week.

ODPA solution	Immersion time			
	5 min	60 min	24 h	1 week
THF 1 mM				

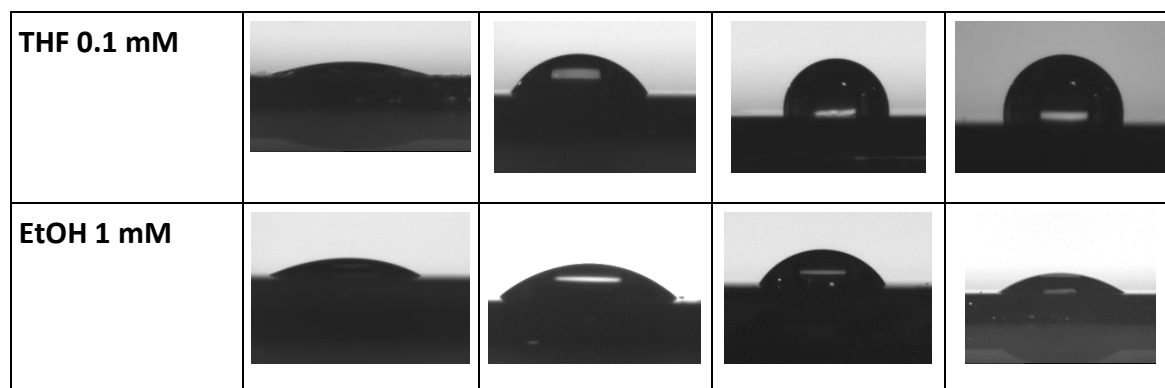


Table 4 Contact angles and hysteresis values for ODPA SAMs on Ta₂O₅ after 24 h immersion.

ODPA solution	Contact angle after 24 h / °	Hysteresis / Δ°
1 mM in THF	98.0 ± 0.7	11.4 ± 1.3
0.1 mM in THF	92.8 ± 1.0	11.4 ± 0.2
0.1 mM in EtOH	62.5 ± 6.5	19.2 ± 6.6

Table 5 Contact angles and hysteresis values for ODPA SAMs on Ta₂O₅ after 1 week immersion

ODPA solution	Contact angle after 1 week / °	Hysteresis / Δ°
1 mM in THF	97.0 ± 1.9	10.1 ± 0.8
0.1 mM in THF	92.8 ± 1.0	10.7 ± 1.9
0.1 mM in EtOH	31.8 ± 5.5	19.8 ± 0.7

Whilst ODPA SAMs from THF did form a hydrophobic surface, the resulting contact angle was much lower than expected. ODPA SAMs on other oxides give values exceeding 100°. Octadecylphosphate SAMs on Ta₂O₅ give a coverage of 113 ± 2°. ⁶² As there is no measurement of an ODPA SAM on Ta₂O₅, the value of 113° has been selected to signify a full-coverage SAM assuming that the properties of ODPA and octadecylphosphate SAMs are analogous. Cassie's law can be used to predict the coverage of a SAM using contact angle analysis (Equation 3.1).

$$\cos\theta = f_1\cos\theta_1 + f_2\cos\theta_2 \quad (3.1)$$

Where θ is the measured contact angle of the SAM, θ_1 is the hypothetical contact angle of the perfect SAM, θ_2 is the contact angle of the freshly cleaned substrate, f_1 is fractional SAM coverage, f_2 is fractional substrate area ($1-f_1$).

Table 6 Fractional coverage of ODPA SAMs on Ta₂O₅ calculated using the Cassie equation.

ODPA solution	Fractional coverage after 1 week
1 mM THF	0.81
0.1 mM THF	0.75
0.1 mM EtOH	0.11

It is clear that for this method of self-assembly, THF performs as a better solvent than EtOH. This has been shown previously as a result of strong solvent-oxide interactions when the solvent is highly polar. Thus, phosphonic acid head groups attach in a disordered manner. Phosphonic acids are believed to rapidly form discrete islands on the oxide surfaces which then coalesce with time.⁹³ The more concentrated THF solution shows a dramatic increase in hydrophobicity within 5 minutes with a large standard deviation, which may agree with the island growth mechanism as there are localised areas of ODPA but a lack of homogeneity. At 24 h, the surface is much more hydrophobic, and the standard deviation is low.

SAMs of phenylphosphonic acid are more difficult to characterise than n-alkylphosphonic acids with wettability measurements alone. However, 1 mM solutions of phenylphosphonic acid in water, EtOH and THF were prepared, and the monolayers prepared as for ODPA. The contact angles after 1 week immersion time are shown in Table 7. The value of the PPA contact angle resembles that of phenylsilanes and phenylphosphonic acids on ITO when prepared in EtOH and THF.^{64,95,96} Long-chain SAMs are stabilised and form dense monolayers by intermolecular forces, which does not occur in the phenyl derivatives, and so these SAMs can be more disordered which explains the large contact angle hysteresis.

Table 7 Contact angle and hysteresis of phenylphosphonic acid SAMs formed after 1 week in water, ethanol and THF. Hysteresis value not recorded for THF due to substrate size.

Solvent	Contact angle / °	Hysteresis / Δ°
Water	27.1 ± 1.9	26.1 ± 4.9
Ethanol	59.0 ± 1.3	24.7 ± 12.1
THF	71.8 ± 0.7	-

3.2.2 Tethering by aggregation and growth (T-BAG) method

The second method was the tethering by aggregation and growth method (T-BAG) described by Hanson.⁷⁴ In this method, the freshly cleaned substrate is held vertically in a solution of phosphonic acid and the solvent is allowed to evaporate. The phosphonic acid molecules orient themselves at the solvent-air interface to form well-ordered monolayers on the oxide substrate. Once the substrate was no longer suspended in the solution, it was rinsed with the corresponding solvent and annealed at 140 °C for 48 h. Then the substrate was sonicated in the potassium carbonate solution followed by water and dried under Ar before measuring the contact angle.

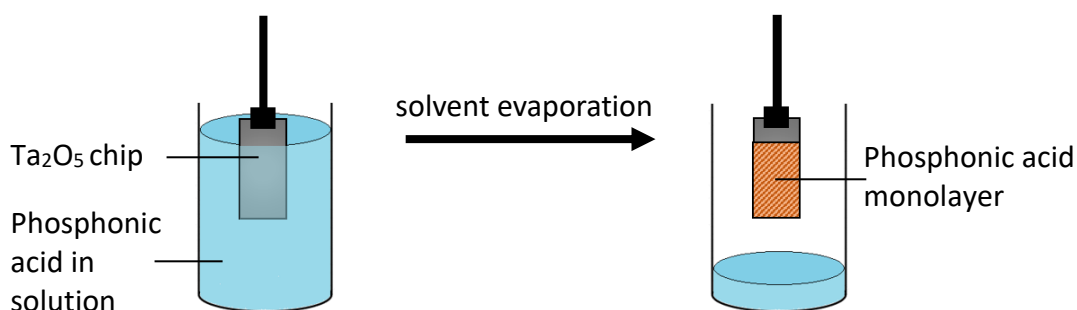


Figure 20 The set-up of the tethering by aggregation and growth (T-BAG) method. The Ta₂O₅ wafer is suspended vertically in a solution of the target phosphonic acid solution, the solvent is left to evaporate, forming a functionalised Ta₂O₅ substrate.

As with the immersion method, THF and EtOH were chosen as the solvents representing a mildly polar and highly polar solvent system. The THF-based SAMs were formed much quicker than the EtOH SAMs as the solvent was left to evaporate at room temperature. This meant that there was a higher chance of the EtOH SAMs or the substrate to become contaminated. As only small volumes of the ODPA solution were used in this initial experiment, the concentration increase as the solvent meniscus passes over the substrate may influence the overall quality of the SAM. The critical micelle concentration (CMC) of ODPA in THF is 100 mM, and 0.2 mM in EtOH.⁹⁷ For each of the THF solutions, the final concentration was well below the CMC. Only the 0.01 mM and 0.001 mM EtOH solutions stayed under the CMC. A white film was visible on the Ta₂O₅ substrate treated with the 1 mM ODPA solution in EtOH indicating the formation of micelles or multilayers. This was

removed with the cleaning steps, although any residual roughness may have led to the hydrophobicity of this sample.

Table 8 The contact angles and hysteresis for ODPA SAMs formed on Ta₂O₅ using the T-BAG method. ODPA solutions were in EtOH and THF with initial concentrations of 1 mM - 0.001 mM.

Solvent	Initial concentration / mM	Contact angle / °	Hysteresis / Δ°
THF	1	94.8 ± 4.5	6.4 ± 5.7
	0.1	93.2 ± 1.6	12.0 ± 1.5
	0.01	82.8 ± 0.9	12.7 ± 1.8
	0.001	68.7 ± 4.7	12.0 ± 0.7
EtOH	1	102.8 ± 2.3	9.0 ± 0.1
	0.1	92.4 ± 2.4	10.3 ± 0.6
	0.01	93.2 ± 1.6	10.0 ± 0.8
	0.001	76.5 ± 1.1	13.5 ± 1.0

For the 1 mM and 0.1 mM samples in THF the contact angle and hysteresis is in agreement with that in the immersion method, resulting in a hydrophobic surface. At lower concentrations the contact angle falls. For EtOH the contact angles greatly exceed the values obtained using the immersion method. Even at low concentrations (0.01 mM) the contact angle is in line with the more concentrated THF samples. The hysteresis values for the 1 mM – 0.01 mM samples are low which would indicate a densely packed monolayer. With only contact angle data it is difficult to determine the effect of exceeding the critical micelle concentration as the SAMs from EtOH solutions appear to be of equal or superior quality to the THF samples. As EtOH is a cheaper, more readily available, and environmentally friendly solvent than THF, it would be beneficial if good quality SAMs could be produced from EtOH. The ability to use lower phosphonic acid concentrations is also beneficial when considering the scalability of the method.

3.3 WERS characterisation of phosphonic acid monolayers

Contact angle analysis showed that stable self-assembled monolayers of phosphonic acids can be formed on Ta₂O₅. Measurement of the contact angle to assess surface coverage is difficult when functional groups are present that may interact with water. Further characterisation of these monolayers could be conducted by ellipsometry,⁹⁴ X-ray photoelectron spectroscopy (XPS)^{64,95}, atomic force microscopy (AFM), and ideally

waveguide enhanced Raman spectroscopy. Analysis with infrared or confocal Raman microscopy is not applicable for this characterisation due to the small number and thin monolayer of molecules and transparent substrate.

For WERS analysis, two self-assembling molecules were selected. For TE polarized WERS, *m*-nitrophenylphosphonic acid (NPPA) was selected. For TM polarized WERS, *p*-cyanophenylphosphonic acid (CNPPA) was selected. These were selected as the molecules possess a distinctive, polarizable functional group with a vibration parallel to the direction of the electric field, increasing the potential signal intensity as a result of the Raman selection rules. Due to time restraints and the impacts related to Covid-19, it was not possible to fabricate chips optimised for TM excitation, so both analytes were used only on the TE chips.

The WERS spectrum of NPPA monolayer on Ta₂O₅ waveguide is shown in Figure 21, shown by the bold lines. The lighter lines represent the background measurements, which take into account the waveguide and substrate before functionalisation, with air as the superstrate. The spectrum is largely dominated by the background, but emerging peaks at 1350 cm⁻¹ and 1175 cm⁻¹ may be tentatively assigned to NPPA, originating from the NO₂ symmetric stretch and C-H ring deformation, respectively. These have been highlighted with an asterisk in Figure 21. These features were not present in background measurements, even conducted with longer acquisition times (up to five minutes) and were not present in measurements of bulk solvents recorded on the same waveguide chip before the addition of NPPA. The weakness of the bands may be a result of damage to the waveguide surface from repeated use, resulting in increased surface and end facet roughness, increasing the loss, and reducing the signal collection efficiency. The laser power was also relatively low (6.3 mW for a 785 nm laser) compared to previous demonstrations of WERS, even with shorter excitation wavelengths.

Within the time frame of this work, it was not possible to obtain additional chips or a higher-powered laser. While the weakness of the spectrum restricts any in-depth analysis of the monolayer, it does show promise of WERS in low-concentration analysis, given an optimised system. This is the first indication of WERS of a monolayer using a planar waveguide and 785 nm excitation. The benefit of this system is that the chip can be easily placed into the device without needing to adjust any components, and the laser is

coupled into the waveguide effectively. The detector is thermoelectrically cooled so there is no requirement for liquid nitrogen. These are overall qualities of a low-burden detection system.

Spectra collected from the CNPPA monolayer with TE excitation gave no indication of any surface species.

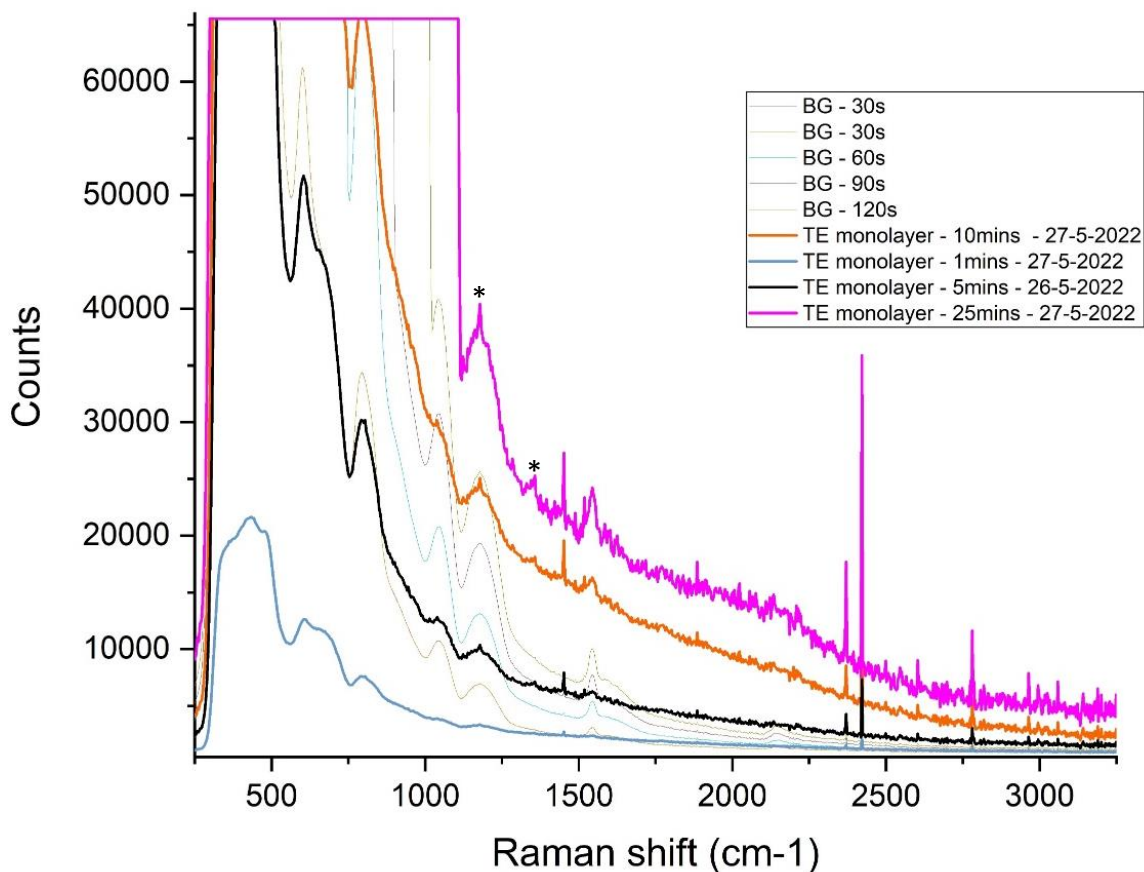


Figure 21 WER spectra of NPPA monolayers on Ta_2O_5 waveguide (bold lines), also showing the background (pale lines) of an unmodified chip, in the TE configuration. The background and sample spectra have been collected with various acquisition times, and potential sample peaks have been indicated with *. The excitation wavelength is 785 nm, with 6.3 mW power in the waveguide.

Assuming that with sufficient time and optimisation the quality of the spectra could be improved, it may be possible to characterise the adsorbed species and their behaviour in more depth. Previous work³⁶ showed that knowledge of the polarizability tensor of a target molecule could be used in conjunction with polarized WERS measurements using TE and TM excited modes to determine the orientation of a target molecule on the waveguide. The polarizability tensor α is a 3x3 matrix that relates the electric field vector

Chapter 3

of the incident light (x_i, y_i, z_i) to the electric field vector of the Raman scattered light (x_s, y_s, z_s) .

$$\begin{pmatrix} x_s \\ y_s \\ z_s \end{pmatrix} = \begin{pmatrix} \alpha_{xx} & \alpha_{xy} & \alpha_{xz} \\ \alpha_{yx} & \alpha_{yy} & \alpha_{yz} \\ \alpha_{zx} & \alpha_{zy} & \alpha_{zz} \end{pmatrix} \begin{pmatrix} x_i \\ y_i \\ z_i \end{pmatrix} \quad (3.2)$$

In the work by Kanger and Otto, the orientation analysis was only conducted for highly symmetrical molecules (D_{4h}), where the tensorial properties are known or can be readily calculated. For larger or more complex molecules, it may become necessary to employ computational methods such as density functional theory (DFT) to generate the polarizability tensor.

To use the polarizability tensor to characterise the surface adsorption behaviour, the relationship in Equation 3.3 is used. This states that the overall power of a Raman signal emitted from a given vibration depends on the polarization of the incident and scattered electric field and on the polarizability tensor. The scattered electric field refers here to the direction of the collection polarizer.

$$I \propto |e_s \cdot \alpha_k \cdot e_i|^2 \quad (3.3)$$

Rotating the incident and scattered light normal or parallel to the surface yields information on the depolarization ratio, ρ , giving an insight into the orientation of dipoles at a surface.

$$\rho = \frac{I_{\perp}}{I_{\parallel}} \quad (3.4)$$

This can be expanded into Equation 3.5.³⁶

$$\rho = \frac{\int_0^{2\pi} \int_0^{2\pi} \int_0^{\pi} |e_s^{\perp} \cdot (R(\psi\phi\theta) \cdot \alpha_k \cdot R^{-1}) \cdot e_i^{\perp}|^2 d\psi d\phi d\theta}{\int_0^{2\pi} \int_0^{2\pi} \int_0^{\pi} |e_s^{\parallel} \cdot (R(\psi\phi\theta) \cdot \alpha_k \cdot R^{-1}) \cdot e_i^{\parallel}|^2 d\psi d\phi d\theta} \quad (3.5)$$

Where e_s and e_i relate to the scattered and incident light vectors both parallel and perpendicular to the surface axis. The Raman tensor of vibrational mode k is defined in the molecular frame as α_k and is transformed into the measurement frame by $R(\psi\phi\theta)$ (Where $R(\psi\phi\theta) = R(\psi)R(\phi)R(\theta)$). R^{-1} represents the transpose of the matrix $R(\psi\phi\theta)$.

$$R(\psi) = \begin{pmatrix} \cos \psi & \sin \psi & 0 \\ -\sin \psi & \cos \psi & 0 \\ 0 & 0 & 1 \end{pmatrix} \quad (3.6)$$

$$R(\phi) = \begin{pmatrix} \cos \phi & \sin \phi & 0 \\ -\sin \phi & \cos \phi & 0 \\ 0 & 0 & 1 \end{pmatrix} \quad (3.7)$$

$$R(\theta) = \begin{pmatrix} 1 & 0 & 0 \\ 0 & \cos \theta & \sin \theta \\ 0 & -\sin \theta & \cos \theta \end{pmatrix} \quad (3.8)$$

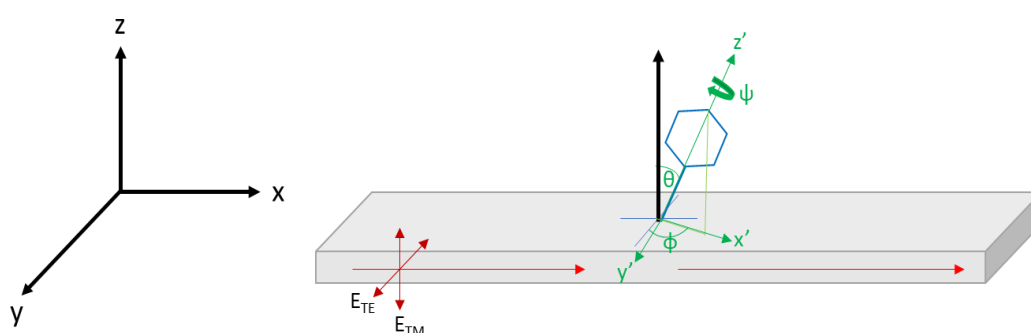


Figure 22 A depiction of the planar waveguide and molecular axes, showing the tilt, rotation and azimuthal angles.

In Equation 3.5, it is shown that the depolarization ratio is a function of the tilt, rotation and azimuthal angles of the adsorbate, depicted in Figure 22. Assuming that the rotation and azimuthal angles are averaged out by random rotations, the equation can be simplified to consider only the tilt angle. A plot of the depolarization ratio *versus* the tilt angle can be produced where ϵ_i , ϵ_s , and α_k are known. This plot would provide a calibration curve with which to compare experimentally derived polarized WERS data to estimate the tilt angle of the adsorbate in question.

The molecules of interest in this work were CNPPA and NPPA. Both possess C_1 symmetry, and the polarizability tensors are unknown. In *Principles of Surface Enhanced Raman Spectroscopy*, Le Ru and Etchegoin describe the derivation of the polarizability tensor from the polarizability derivatives given as an output from a Gaussian^(TM) density functional calculation.⁵⁹ This process has been conducted for CNPPA and NPPA. From the predicted spectra (Figure 24 and Figure 27), a number of key vibrational modes were identified. Factors involved in choosing the vibrational modes were the predicted

scattering strength and the isolation of the bands. Only simple, well-characterised vibrations were selected. Bands related to the phosphonic acid headgroup were excluded as adsorption to the substrate would have a significant effect on the electronic properties of this group.

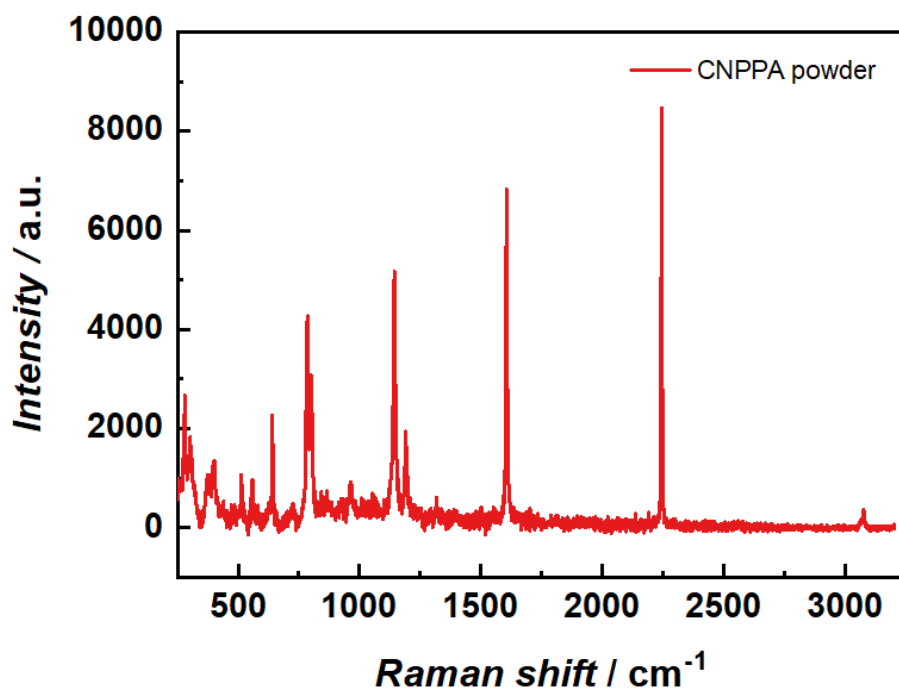


Figure 23 The Raman spectrum of CNPPA powder. The spectrum was collected using 785 nm excitation, 1 mW, and an acquisition time of 10 s.

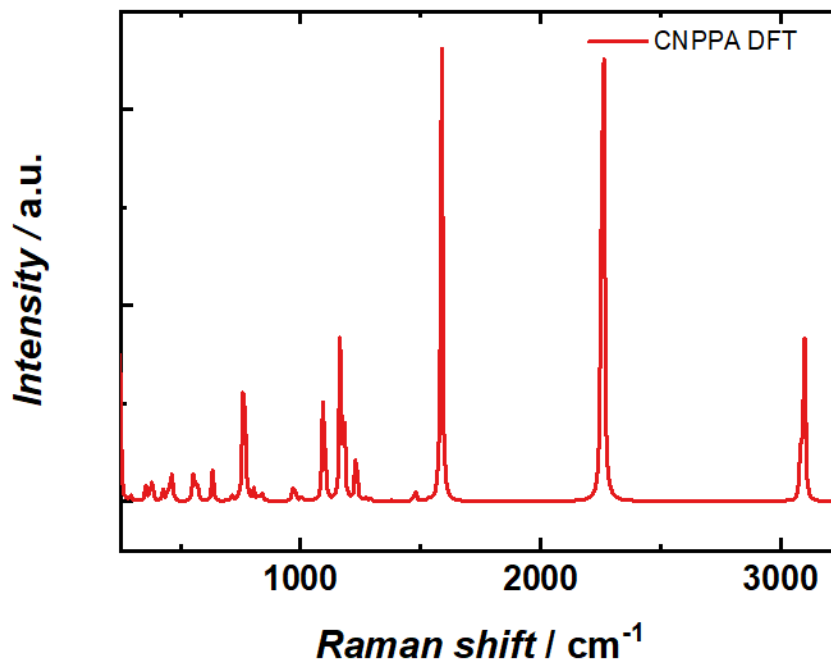


Figure 24 DFT Raman spectrum of a single molecule of CNPPA. This was calculated at the B3LYP 6-311G++(d,p) level of theory. The Raman shift was scaled by a factor of 0.9668 to account for the exchange correlation.

Figure 23Figure 24 depict the Raman spectrum of CNPPA collected using the Raman microscope and theoretically using DFT, respectively. These spectra are similar, and show the characteristic nitrile stretch at approximately 2250 cm^{-1} , the C=C stretch at approximately 1600 cm^{-1} and other characteristic modes for benzene derivatives further into the fingerprint region. DFT calculations performed at this level of theory have therefore been deemed appropriate for use in further characterisation work. Differences in the intensities of the bands observed for the two methods arise from the orientation of crystal regions and the reduced CCD efficacy at large shifts when using NIR excitation. Some differences are intrinsic to DFT.

Table 9 shows the calculated Raman tensors for the selected vibrational modes. The atomic displacement is limited to two decimal places, and the resulting Raman tensor is also bound by this limitation. However, this should not significantly hinder the estimation accuracy of the adsorption tilt angle.

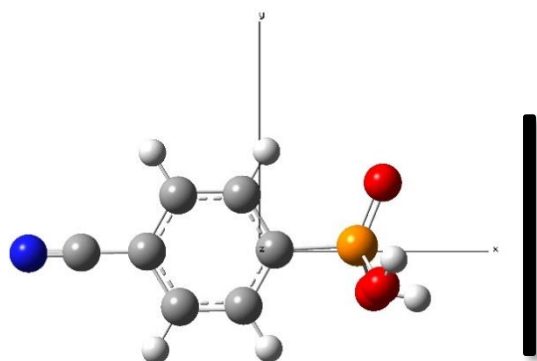
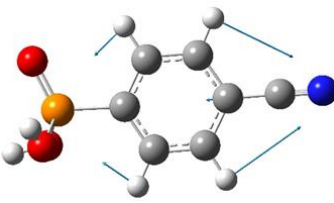
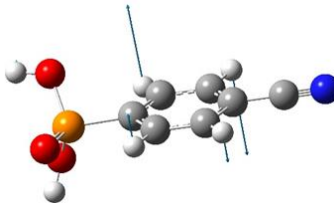
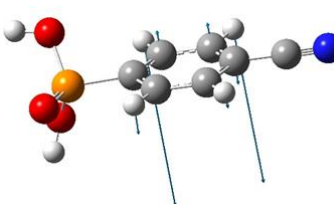
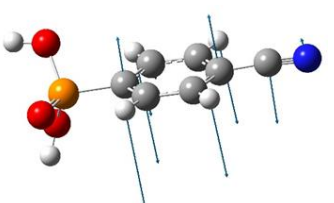


Figure 25 Structure and coordinate axes for CNPPA. The expected surface plane where CNPPA would be expected to adsorb when forming a monolayer is shown by the black line. This is representative only, as the adsorption angle is yet to be fully determined.

Table 9 DFT predictions for each vibrational mode of CNPPA and the calculated Raman tensor.

Frequency / cm^{-1}	Reduced mass	Raman activity / $10^{-36} \text{ m}^2 \text{ cm sr}^{-1}$	Depolarisation ratio	Vibrational pattern	Raman tensor / $\text{\AA}^2 \text{ amu}^{-1/2}$
2336	12.6794	628.2611	0.2900		$\begin{pmatrix} -7.13 & 0.12 & -0.04 \\ 0.12 & -0.32 & 0.00 \\ -0.04 & 0.00 & -0.26 \end{pmatrix}$
1642	5.5107	196.1953	0.4812		$\begin{pmatrix} -4.05 & 0.11 & 0.01 \\ 0.11 & 0.82 & -0.02 \\ 0.01 & -0.02 & 0.07 \end{pmatrix}$

1206	1.4317	48.9026	0.1604		$\begin{pmatrix} -1.86 & 0.05 & 0.00 \\ 0.05 & -0.71 & 0.01 \\ 0.00 & 0.01 & -0.07 \end{pmatrix}$
984	1.3252	0.2524	0.6913		$\begin{pmatrix} -0.02 & 0.00 & 0.08 \\ 0 & -0.02 & 0.00 \\ 0.08 & 0.00 & -0.01 \end{pmatrix}$
849	1.4487	0.6382	0.7117		$\begin{pmatrix} 0.03 & -0.02 & 0.15 \\ -0.02 & 0.04 & 0.01 \\ 0.15 & 0.01 & 0.01 \end{pmatrix}$
579	3.4424	1.5499	0.7306		$\begin{pmatrix} -0.04 & 0.01 & -0.24 \\ 0.01 & 0.00 & 0.01 \\ -0.24 & 0.01 & 0.01 \end{pmatrix}$

The process was repeated for NPPA. Using the same level of theory and basis set, the output structure of the nitro group was depicted as two double N=O bonds, which should be taken into consideration when assessing the vibrational properties predicted.

The Raman spectrum of NPPA is shown in Figure 26, showing the spectrum in the 1250-1450 cm^{-1} range. A significant fluorescent background was observed under all measurement conditions tested, preventing full characterisation of the material by obscuring vibrational features. A peak can be observed at approximately 1350 cm^{-1} which has been attributed to the symmetric NO_2 stretch.

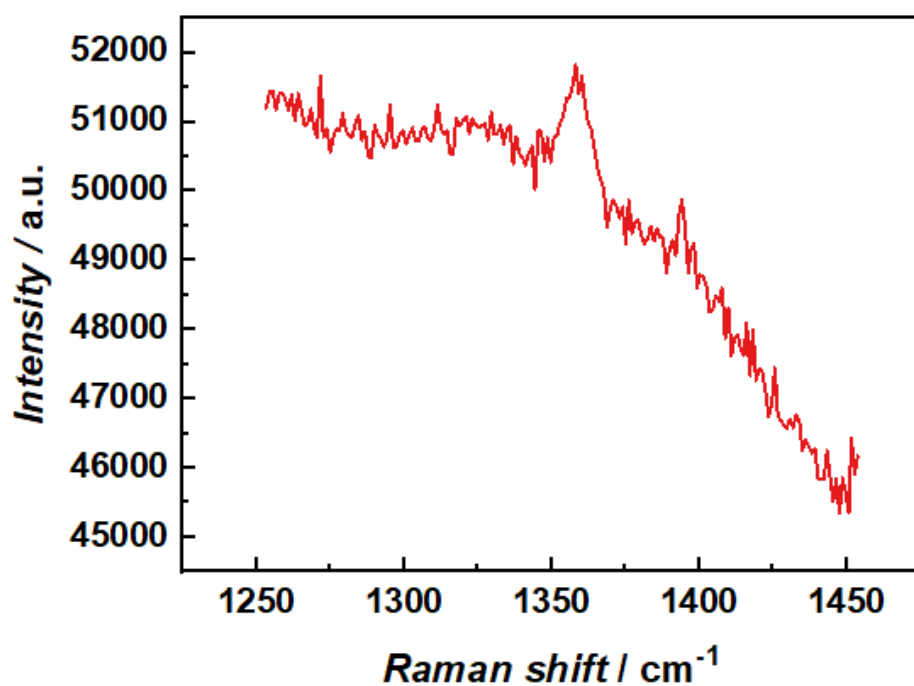


Figure 26 The Raman spectrum of NPPA powder. A significant fluorescent background was observed, obscuring Raman features. The spectrum is shown for the range 1250-1450 cm^{-1} which features the symmetric NO_2 stretch.

Where the fluorescent background cannot be avoided, for example by using an alternate excitation wavelength, DFT provides a method for generating a predicted spectrum and for assigning bands. The DFT generated spectrum is shown in Figure 27.

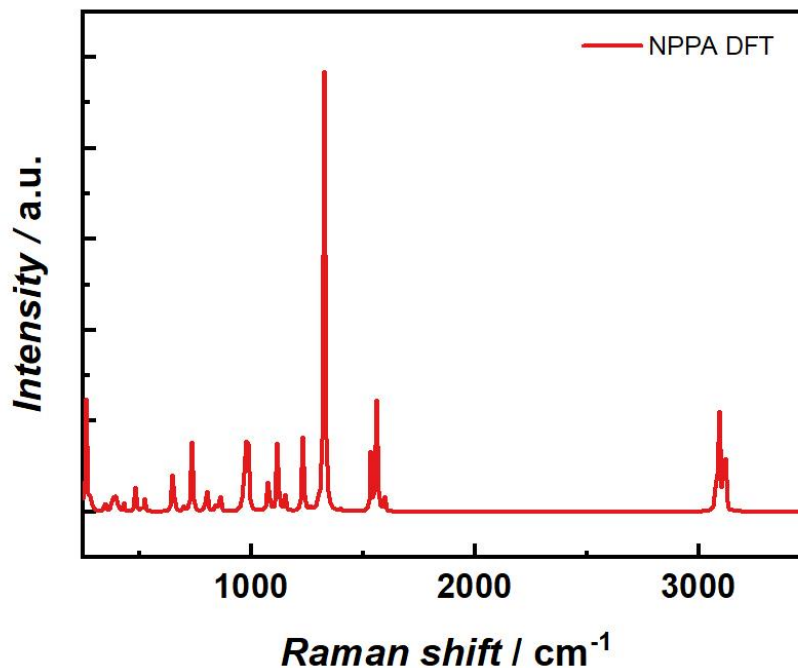


Figure 27 DFT Raman spectrum of a single molecule of NPPA. This was calculated at the B3LYP 6-311G++(d,p) level of theory. The Raman shift was scaled by a factor of 0.9668 to account for the exchange correlation.

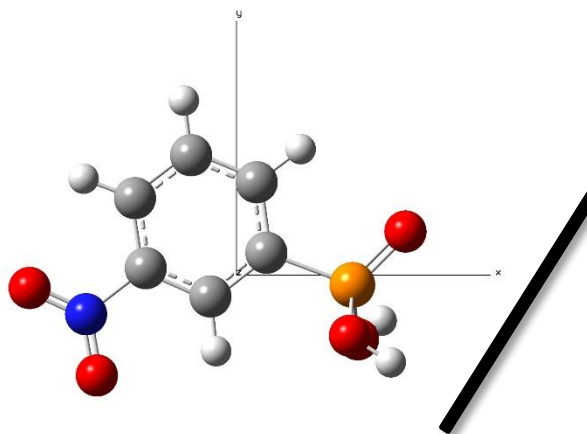
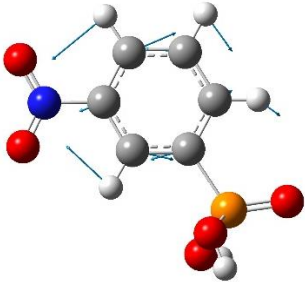
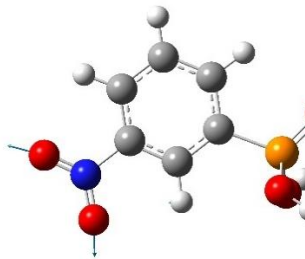
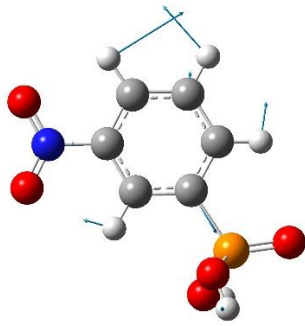
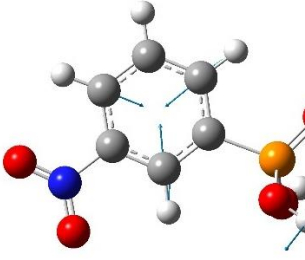


Figure 28 Structure and Cartesian axis of NPPA used in this calculation. Note the two N=O double bonds. A representative surface plane showing where NPPA would be expected to adsorb in a monolayer is depicted by the black line, although the angle is yet to be determined through a combined theoretical and experimental approach.

Table 10 Raman tensors of selected vibrational bands of NPPA

Frequency / cm^{-1}	Reduced mass	Raman activity / 10^{-36} $\text{m}^2 \text{cm} \text{sr}^{-1}$	Depolarisation ratio	Vibrational pattern	Raman tensor / Å^2 $\text{amu}^{-1/2}$
1562	5.99	48.71	0.6357		$\begin{pmatrix} 0.75 & 1.39 & 0.02 \\ 1.39 & 0.25 & 0.00 \\ 0.02 & 0.00 & -0.07 \end{pmatrix}$
1326	14.04	154.97	0.4007		$\begin{pmatrix} 2.67 & 1.31 & 0.01 \\ 1.31 & 1.43 & 0.02 \\ 0.01 & 0.02 & -0.01 \end{pmatrix}$
1119	3.79	23.45	0.1119		$\begin{pmatrix} 1.08 & 0.19 & -0.01 \\ 0.19 & 0.66 & 0.00 \\ -0.01 & 0.000 & 0.12 \end{pmatrix}$
982	4.9111	32.9094	0.0636		$\begin{pmatrix} -0.02 & 0.00 & 0.08 \\ 0 & -0.02 & 0.00 \\ 0.08 & 0.00 & -0.01 \end{pmatrix}$

Although in the absence of clear WERS spectra, the calculated tensors cannot currently be used to assess the tilt angle of adsorbates from polarized WERS measurements, their validity has been assessed by performing self-consistency checks. The values in the tensors are used to generate the depolarization ratio and Raman activity and are compared to the values predicted from the DFT output file. Gaussian reports the atomic displacement at two decimal places, which the tensors are reliant on, so minor rounding effects are seen when performing the self-consistency checks. Otherwise, good agreement is observed.

DFT may also be used to predict the spectral changes observed from the adsorption of an analyte on a surface. This requires some optimisation, as the inclusion of surface atoms increases the computational time significantly, but the inclusion of more information into the calculation allows for a better prediction of all the adsorption effects.

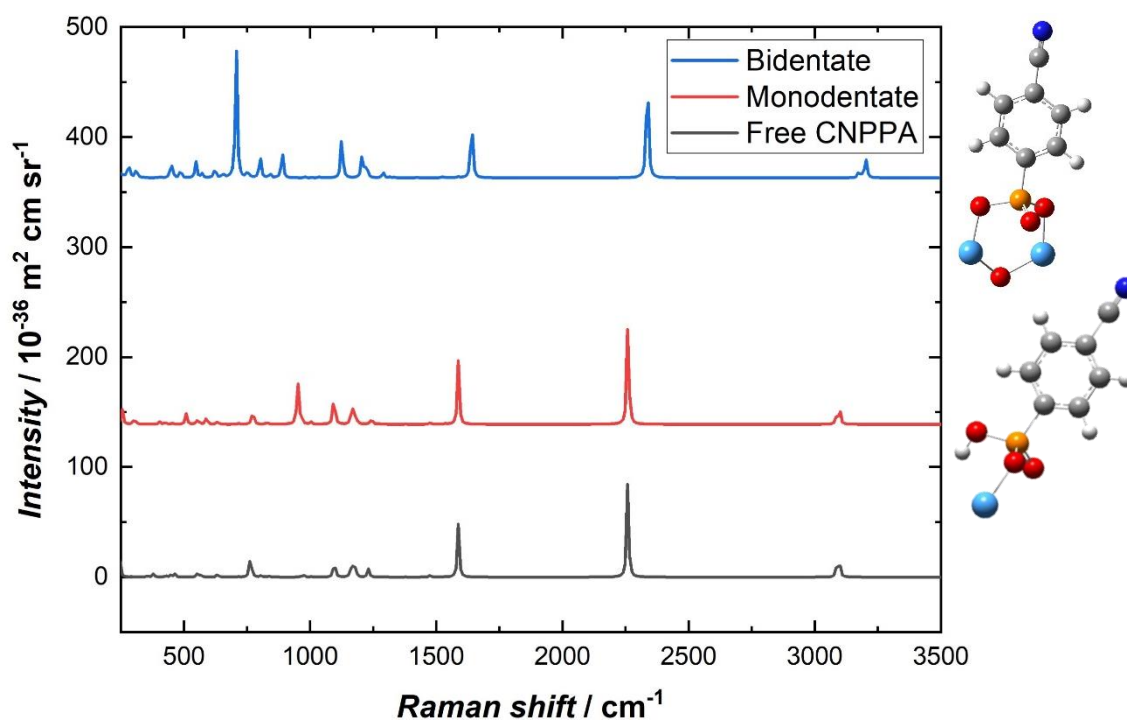


Figure 29 Spectra showing the DFT predictions of free (bottom), monodentate (middle) and bidentate (top) coordinated CNPPA to Ta atoms.

Figure 29 shows the predicted spectra from the coordination modes pictured. A split basis set was used for the calculation, with the Lanl2dz basis used for Ta atoms, and 6-311G++(d,p) used for C, N, O, P, and H atoms. Free CNPPA shows the spectrum of the

unbound molecule. Monodentate refers to the situation where one CNPPA oxygen atom is bonded to one Ta atom. The bidentate configuration here refers to two CNPPA oxygen atoms bonded to separate Ta atoms, which are bridged by an oxygen atom, representing the Ta₂O₅ surface. This only provides a very limited picture of the true surface, but in the future may provide a useful reference for characterising adsorption behaviour from WER spectra from the intensity ratios and positions of bands.

3.4 Formation of functional interfaces

Self-assembled monolayers with reactive functional groups can be modified in a ground-up approach to provide additional and controlled surface properties. One research area is in biosensors, where modification of the initial monolayer can be used to introduce anti-fouling properties, or to immobilise biological recognition units. Introduction of these functional units to a pre-existing monolayer allows for greater control over the spatial distribution of the biological molecules, which may optimise their function. The range of options for the functional group(s) presented by a self-assembled monolayer means that choices can be made to maximise the immobilisation efficiency, adsorption strength, and retain the structure and function of the biological molecule.

In unpublished work, Dr Marti-Morant used confocal fluorescence microscopy as evidence that functional SAMS on Ta₂O₅ had been created, following the methodology described earlier in this chapter. 12-aminododecylphosphonic acid was used to generate a primary amine-presenting surface. To this, a succinimidyl ester of AlexaFluor488 dye was conjugated. This was observed by the fluorescence at the surface, which remained after several washing steps. Very little fluorescence was observed where the dye was incubated with unfunctionalised Ta₂O₅. In the control, no fluorescence was observed. In further work, a mixed dibenzocyclooctyne (DBCO) and -CH₃ presenting monolayer was produced. The DBCO group underwent rapid cycloaddition with azidylated AlexaFluor488. The optimal CH₃: DBCO ratio, with the greatest fluorescence intensity was determined to be 17:3. This is because the steric bulk of the dye molecule AF488 inhibits access to the surface when densely packed. This ratio could be used to guide future work where bulky biological receptors are immobilised on the surface.

The success of this work is significant as it confirms the successful functionalisation of Ta_2O_5 by phosphonic acids following the method described in this chapter, and shows that a bottom-up approach to developing biofunctional interfaces has merit.

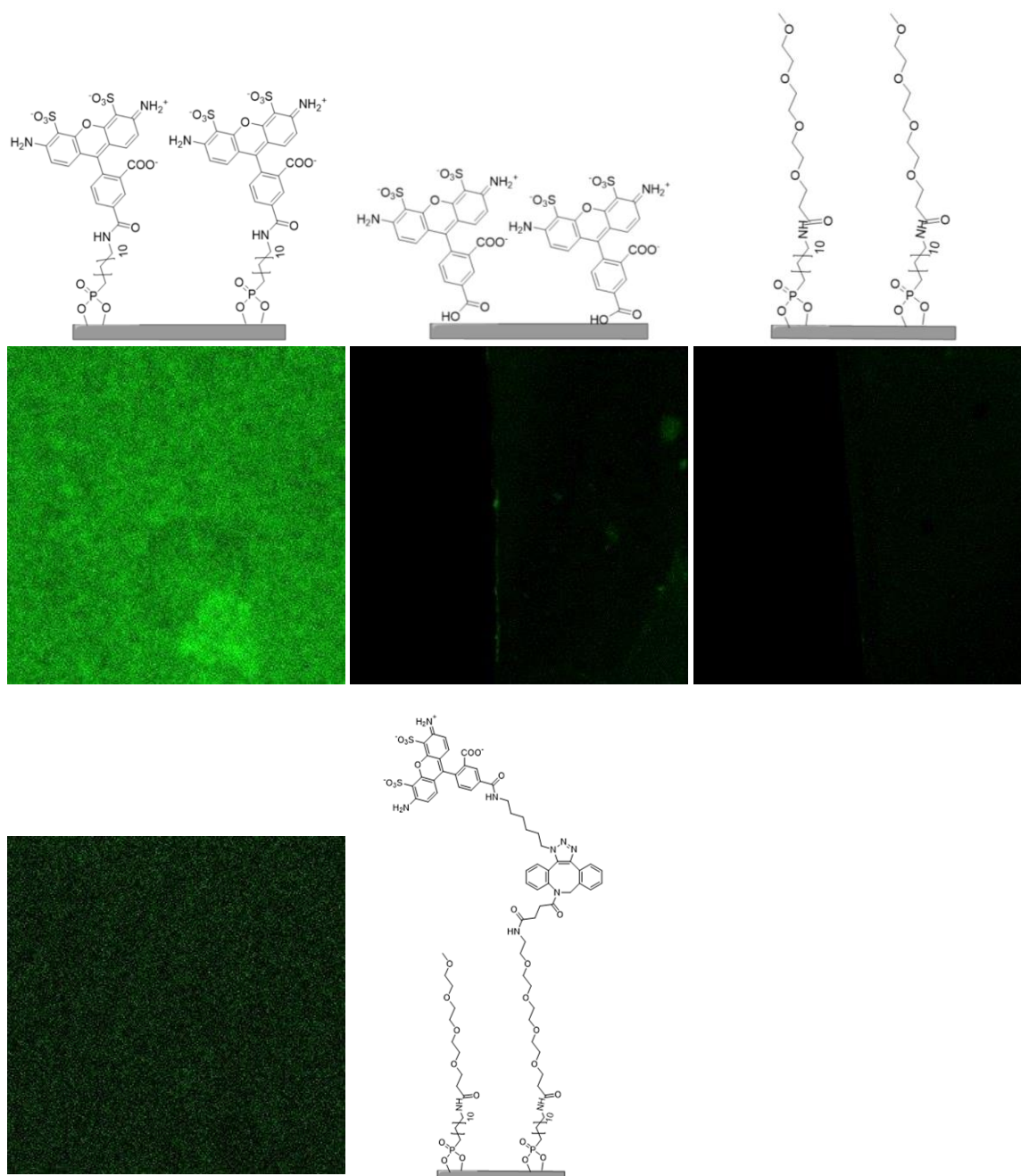


Figure 30 Confocal fluorescence images of Ta_2O_5 with different surface chemistries. The substrates were incubated with AF488 dye. Top left shows the covalent linkage of AF488 to the surface and shows the highest density of dye. Top middle shows where dye was introduced to the surface, but subsequently washed away. Top right shows a phosphonic acid monolayer in the absence of

dye. Bottom left shows the mixed monolayer, where some dye is covalently linked. A low level of fluorescence is observed.

In a second example, a SAM of phosphonohexadecanoic acid (PHDA) was formed from immersion in a 1 mM solution in THF, using the pre- and post-treatment methods described in Section 2.2.4. The water contact angle of the functionalised Ta₂O₅ substrate was 81°. An untreated Ta₂O₅ substrate has a similar contact angle, and it is difficult to distinguish the PHDA SAM from an untreated substrate. To determine whether a monolayer had been formed, the carboxylic group was activated with EDC/NHS chemistry and oligoethyleneglycol-containing (OEG) molecules were introduced. The intention was to observe a change in the surface properties of Ta₂O₅ while introducing a group known for its anti-fouling properties.

m-dPEG₈-amine (NH₂-EO₇-OCH₃) and amino-dPEG₈-OH (NH₂-EO₇-OH) are both hydrophilic linkers containing an oligoethyleneglycol part (EO₇). These were grafted to the carboxylic acid-presenting surface using EDC/NHS coupling chemistry, altering the ratio of NH₂-EO₇-OCH₃ and NH₂-EO₇-OH to observe any effects on the contact angle as the number of terminal -CH₃ groups increased. While the water contact angle has decreased with respect to the PHDA-modified surface, there is no discernible difference when altering the ratio of the OH and CH₃ functional groups. This could be due to the flexibility of OEG chains, which may overlap or be laying flat instead of exposing the end group. Nevertheless, the decreased contact angle, which continued to be observed after several rinsing cycles suggests a covalent bond to the surface.

Table 11 The contact angle measured as a function of the ratio of -OCH₃ to -OH terminated oligoethylene glycol units is increased

NH ₂ -EO ₇ -OH:NH ₂ -EO ₇ -OCH ₃	Water contact angle/ °
100:0	65.8
75:25	63.8
50:50	60.5
25:75	66.9
0:100	67.2

3.5 Summary

Phosphonic acid derivatives have been shown to functionalise Ta₂O₅ substrates, as determined by the measurement of the water contact angle on what is assumed to be the

self-assembled monolayer of the phosphonic acid. Low hysteresis values (< 10 degrees) indicate a well-packed surface, which would be unlikely to observe in the case of multilayer formation or where excessive defects occur. XPS or ellipsometry may provide an additional confirmation that only a monolayer is present, although these studies have not been conducted for this work. WERS indicated the presence of adsorbed material but was inconclusive. Finally, the stepwise functionalisation of Ta_2O_5 was demonstrated using fluorescence microscopy and contact angle analysis.

The packing of the phosphonic acid monolayers is observed to be optimised by lower polarity solvents, assuming the solubility of the phosphonic acid within the chosen solvent. Two strategies were used to form phosphonic acid monolayers – immersion of the substrate within a solution of the phosphonic acid derivative, and suspension of the substrate in a solution where the solvent is left to evaporate. The timescale between the two methods is comparable. While both methods imparted similar levels of hydrophobicity to the surface using THF, the T-BAG method appeared to provide preliminary evidence for a method that would functionalise metal oxides with phosphonic acids in polar solvents. This may become useful when the phosphonic acid is insoluble in low-polarity solvents. A larger scale study would have to be conducted to assess the feasibility of the T-BAG method, as it is practically more difficult to implement and requires larger quantities of the phosphonic acid to produce significant volumes of the solution to limit the increase in phosphonic acid concentration as the solvent evaporates. An additional consideration is the limited commercial availability of these materials, which may make the obtaining of large quantities prohibitive. While the longer-term stability of the monolayers formed from the two methods was not investigated, useful insights in the development of phosphonic acids as a self-assembled molecules have been gained. Further research is required on these materials before they can be adopted on the same level as organosilanes.

The WER spectrum of a monolayer of *m*-nitrophenylphosphonic acid on a planar Ta_2O_5 waveguide was collected using TE excitation and the WER spectrometer produced as a part of this work. While long acquisition times were required, peaks were weakly present amongst the background signal. Difficulty with further developing the technique arose from the lack of access to facilities for fabrication and analysis. With repeated use, the surface of the waveguide and the end facets became roughened and damaged, increasing

Chapter 3

the propagation losses beyond reasonable amounts. A fresh waveguide chip used with the WERS system may provide more of an insight into where optimisations need to be made. In a fully optimised system, the WERS spectra may be used in conjunction with polarized excitation and collection, with knowledge of the Raman tensor to provide an insight into the orientation of adsorbates. This could be used to guide applications and understanding of the kinetics involved in the formation of self-assembled monolayers or monitor conformational changes of receptor molecules at the surface upon changing experimental conditions. Finally, only WERS from a TE chip was demonstrated in this work, the predicted surface enhancements from a TM chip are greater.

This chapter has demonstrated that surface sensitive, waveguide enhanced Raman spectroscopic platforms can be produced, and tailoring of the surface chemistry towards the desired application is possible by changing the reaction conditions and choice of molecule.

Chapter 4 Raman cross-section analysis of liquid analytes across spectrometer platforms

4.1 Overview

In this chapter, the Raman scattering cross-section (σ) is determined using a 785 nm laser for a series of bulk, organic liquids. Density functional theory (DFT) has been used in conjunction with conventional Raman spectroscopy to verify the results and aid in the assignment of the spectra. This chapter also identifies and develops the concept of using benzyl alcohol as a spectroscopic standard, replacing cyclohexane and toluene as more typical standards. Development of new spectroscopic instruments requires that methods for validating the function and calibration are sought, which is often a time-consuming process. The analyte should therefore be non-volatile and safe to work with over long periods of time, whilst also giving a unique and strong signal. Hence, benzyl alcohol and deuterated benzyl alcohol have been a primary focus.

The expectation is that calculation of the cross-section of benzyl alcohol will enable the determination of enhancement factors provided by WERS through comparison with the results obtained by conventional Raman spectroscopy. The WERS spectra of *m*-diethynylbenzene, benzyl alcohol, and deuterated benzyl alcohol are demonstrated in the latter parts of the chapter.

4.2 Raman cross-section of bulk organic liquids

4.2.1 Introduction

The Raman cross-section (σ) relates the power (P) of scattered light to the incident power density (S_{inc}) through the equation:⁵⁹

$$P = \sigma S_{inc} \quad (4.1)$$

This can be considered as a measure of the efficiency of Raman scattering, determining the intensity of the collected signal.

Chapter 4

There are two forms of the Raman cross-section: absolute and differential.^{59,98}

Measurement of the absolute Raman cross-section requires specialist apparatus as it collects scattered light at every emission angle. As such, it has only been determined for a small number of simple molecules. The differential Raman cross-section ($d\sigma/d\Omega$) is much more readily determined and collects scattered light in a specific direction relative to the incident angle. This is commonly selected at 90° scattering and 180° back-scattering configurations. The Raman power can then be described as a product of the incident power density, the solid angle of collection ($\Delta\Omega$) and the differential Raman cross-section.⁵⁹

$$P = \frac{d\sigma}{d\Omega} \Delta\Omega S_{\text{inc}} \quad (4.2)$$

Factors affecting the cross-section include the excitation wavelength and the refractive index of the analyte or solvent used, and this cross-section varies with the choice of vibrational modes. A large cross-section is typically observed in large, highly polarizable molecules such as in conjugated π -systems, whereas small, hard molecules such as water possess small cross-sections. Knowledge of the cross-section allows the user to be able to determine enhancement factors when comparing normal and enhanced spectroscopic techniques, and also allows for the calibration and assessment of the detection limits for the spectrometer.

Calculation of the relative Raman cross-section relies on the measurement of a “standard” analyte, which has a known differential cross-section. The known cross-section is defined for a specific vibrational mode or set of modes. Comparison of the integrated peak intensities (I) for the standard relative to the chosen analyte allows for the determination of relative Raman cross-section using Equation 4.3. Here, the concentration of the analytes are known, and the measurement conditions are identical.^{59,99}

$$\left(\frac{d\sigma_R}{d\Omega}\right)_{\text{Analyte}} = \left(\frac{d\sigma_R}{d\Omega}\right)_{\text{Reference}} \frac{I_{\text{Analyte}} [\text{Reference}]}{I_{\text{Reference}} [\text{Analyte}]} \quad (4.3)$$

It is possible to determine the relative cross-section for both pure liquids,⁹⁸ and where the analyte is in solution with an internal standard.⁹⁹ In the internal standard method, the reference is assumed to have no interaction with the analyte. This is often not strictly the

case and error may be introduced.¹⁰⁰ The standard must also be chosen so that its characteristic bands do not overlap with those of the analyte. Simple solvents such as water, acetonitrile and chloroform are often chosen for this purpose.

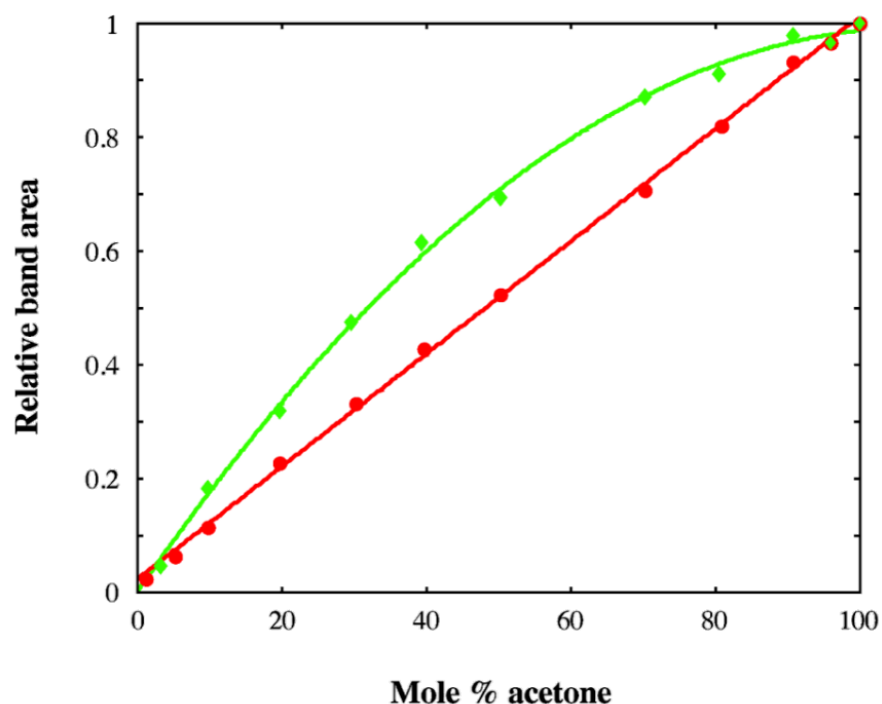


Figure 31 Graph from [99] showing the dependence of the cross-section on environmental factors, in this case, the increasing concentration of acetone. Green represents C=O and red the C-H stretching modes of acetone dissolved in the standard, acetonitrile.

Acosta-Maeda et al. determined the relative Raman cross-sections of a number of pure organic liquids using a pulsed 532 nm excitation source.⁹⁸ To do this, the authors first performed an intensity calibration using a halogen-tungsten lamp and an integrating sphere, approximating a black body radiator. The spectral intensity counts were converted to spectral radiance by dividing the counts by the response function. The intensity calibration allows for correction of measurement artefacts from the spectrometer. Using Equation 4.4, the authors were able to calculate the differential Raman cross-section of cyclohexane.

$$\beta = \frac{L_{\lambda} \Delta \lambda A}{PN(r)_x} \quad (4.4)$$

Chapter 4

Where β is the differential Raman cross-section, $L\lambda$ is the spectral radiance [$\text{W sr}^{-1} \text{cm}^{-2}$], $\Delta\lambda$ is the FWHM of the peak [nm], A is the area [cm^2], P is the laser power [W], $N(r)$ is the number density of molecules in molecules per unit volume, and x is the sample path length.⁹⁸

The authors determined the cross-section of the cyclohexane 801 cm^{-1} mode to be $4.55 \times 10^{-30} \text{ cm}^2 \text{ sr}^{-1} \text{ molecule}^{-1}$ and $5.62 \times 10^{-29} \text{ cm}^2 \text{ sr}^{-2} \text{ molecule}^{-1}$ for the C-H stretching region.⁹⁸ Both these values were very close to previously measured values. The cross-section for acetonitrile was determined at 920 cm^{-1} and 2253 cm^{-1} as 5.63×10^{-31} and $2.87 \times 10^{-30} \text{ cm}^2 \text{ sr}^{-1} \text{ molecule}^{-1}$, respectively.⁹⁸

McCreery and Choquette have worked towards intensity calibration and determination of the spectrometer response function using standard reference materials.^{101,102} For 785 nm excitation, the NIST SRM 2241 provides an ideal standard.¹⁰² This material is made up of chromium-doped glass and gives a broad, luminescent response which has been characterised extensively.¹⁰² Experimentally, it is easier for the user to calibrate the intensity of the spectrometer by finding its response function using this standard when compared to the complex set-up required when using a tungsten lamp apparatus.^{101,102} By using the glass standard, it is possible to more accurately recreate the measurement conditions used when measuring the analytes. Use of these intensity standards has allowed for quantitative analysis between different spectrometers to be carried out. Rodriguez et al. have shown the intensity calibration using SRM 2241 to create a spectral library of pharmaceutical agents.¹⁰³ By applying the intensity calibration procedure to hand-held spectrometers, the author was able to quickly identify the substance using a hit-quality-index, or percentage matching of the hand-held spectrum to the library result measured using the master spectrometer.¹⁰³ The response function has not been taken into account in the work shown in this chapter, but can be readily implemented in the future.

Density functional theory can also be used to predict the cross-sections of molecules. This can allow for geometry optimisation, calculation of force-constants and depolarisation ratios, as well as reporting Raman activities (R_k) for individual modes. R_k can be used to calculate the Raman cross-section using the equation:⁵⁹

$$\frac{d\sigma_k}{d\Omega} = 5.8 \times 10^{-46} \frac{[10^7/(\lambda_L) - (\bar{\nu}_k)]^4}{(\bar{\nu}_k)} L_M(R_k) \left(1 - \exp\left(\frac{-hc\bar{\nu}_k}{k_B T}\right)\right)^{-1} \quad (4.5)$$

Where λ_L is the wavelength of the incident laser [nm], $\bar{\nu}_k$ is the Raman shift [cm⁻¹], R_k is the Raman activity [A⁴ amu⁻¹], c is speed of light [m s⁻¹], k_B is Boltzmann's constant, T is the temperature [K], and L_M is the correction factor that accounts for the refractive index.

Eight analytes have been chosen for this study: cyclohexane, acetonitrile, isopropyl alcohol (IPA), toluene, benzyl alcohol, benzyl-d₇ alcohol, benzenethiol, and *m*-diethynylbenzene. These have been chosen as common solvents with strong, characteristic Raman spectra, with the exception of benzyl-d₇ alcohol and *m*-diethynylbenzene which have been chosen out of interest for their unique spectral properties. Table 12 shows the relevant properties of these analytes, which aid the discussion of their relevance in Raman analysis.

Table 12 The liquid analytes used in this work and their key physical properties. Values have been taken from Sigma-Aldrich.

Analyte	Purity / %	Refractive index	Vapour pressure / Pa at 20°C	Density / g mL ⁻¹	Flash point / °C	BP / °C
Acetonitrile	99.8	1.344	9706	0.786	6	82
Benzenethiol	97.0	1.588	190	1.073	50	169
Benzyl alcohol	99.0	1.539	7	1.045	101	203-205
Benzyl-d ₇ alcohol	99.0	1.537	12.5 (25°C)	1.113	96	203-205
Cyclohexane	99.5	1.426	10266	0.779	-20	81
Isopropyl alcohol	99.5	1.377	4400	0.785	12	82
<i>m</i> -diethynylbenzene	97.0	1.582	46.7 (25°C)	0.949	73	188
Toluene	99.5	1.496	2933	0.865	4	110-111

4.2.2 Experimental cross-section determination

A quartz cuvette was completely filled with the analyte and was then sealed. The cuvette was then placed horizontally inside a 3D-printed custom holder to ensure identical conditions between measurements. The Raman spectra of the analytes were obtained using a Renishaw 2000 Raman spectrometer and a Leica DMLM microscope fitted with a $\times 5$, 0.12 NA objective. Light was collected in the backscattered geometry. Except where stated, each measurement used a 785 nm laser at 10 mW power, and an acquisition time of 10 s. Five repeats were taken for each sample. A reference sample of the empty cuvette was taken, and the spectrum removed from the analyte spectra to give a flat baseline.

Benzyl alcohol and its deuterated analogue were chosen to offer a safer, more convenient analyte for the testing of Raman spectrometers when compared to standards such as toluene, IPA and cyclohexane. Benzyl alcohol is a readily available laboratory solvent with minimal associated health hazards and has a low vapour pressure. As a substituted benzene ring, it is highly polarizable, and should be expected to exhibit a relatively large cross-section comparable to toluene. Benzyl- d_7 alcohol allows for observation of frequency shifts arising from the greater reduced mass of the bonds. The Raman cross-section of this analyte has not yet been reported, so is crucial to determine.

m-diethynylbenzene (*m*-DEB) and benzyl- d_7 alcohol were only available in a small quantity at the time of measurement. As a result, Raman spectra featuring this analyte were taken from focussing the light onto a droplet of the analyte placed on a microscope slide. The interaction volume, evaporation, distance, cuvette barrier, and the effects of the curved surface of the droplet will have an effect on the collected light. Therefore, comparisons between the two collection methods should be made with caution. However, these two analytes have been included in the discussion for interest and completeness. There was a greater scattering response from this *m*-DEB compared to the other analytes in this study, limiting the laser power to 1 mW whilst keeping the remaining measuring conditions identical.

In Figure 32 and in Table 13 to Table 16 the data collected for the individual samples is displayed. The tables have been split to show the relative cross-sections for different vibrational modes. After normalising the spectra to counts $\text{mW}^{-1} \text{s}^{-1}$ and removing the

blank reference from the spectra, Origin software was used to integrate the area under each band. The spectra were then normalised to the cyclohexane C-C stretching mode at 802 cm^{-1} with a cross-section of $1.430 \times 10^{-30}\text{ cm}^2\text{ molecule}^{-1}\text{ sr}^{-1}$ for 785 nm excitation.⁸³ The results appear to follow the expected trend, with the larger, aromatic molecules possessing larger cross-sections compared to the smaller, aliphatic molecules.

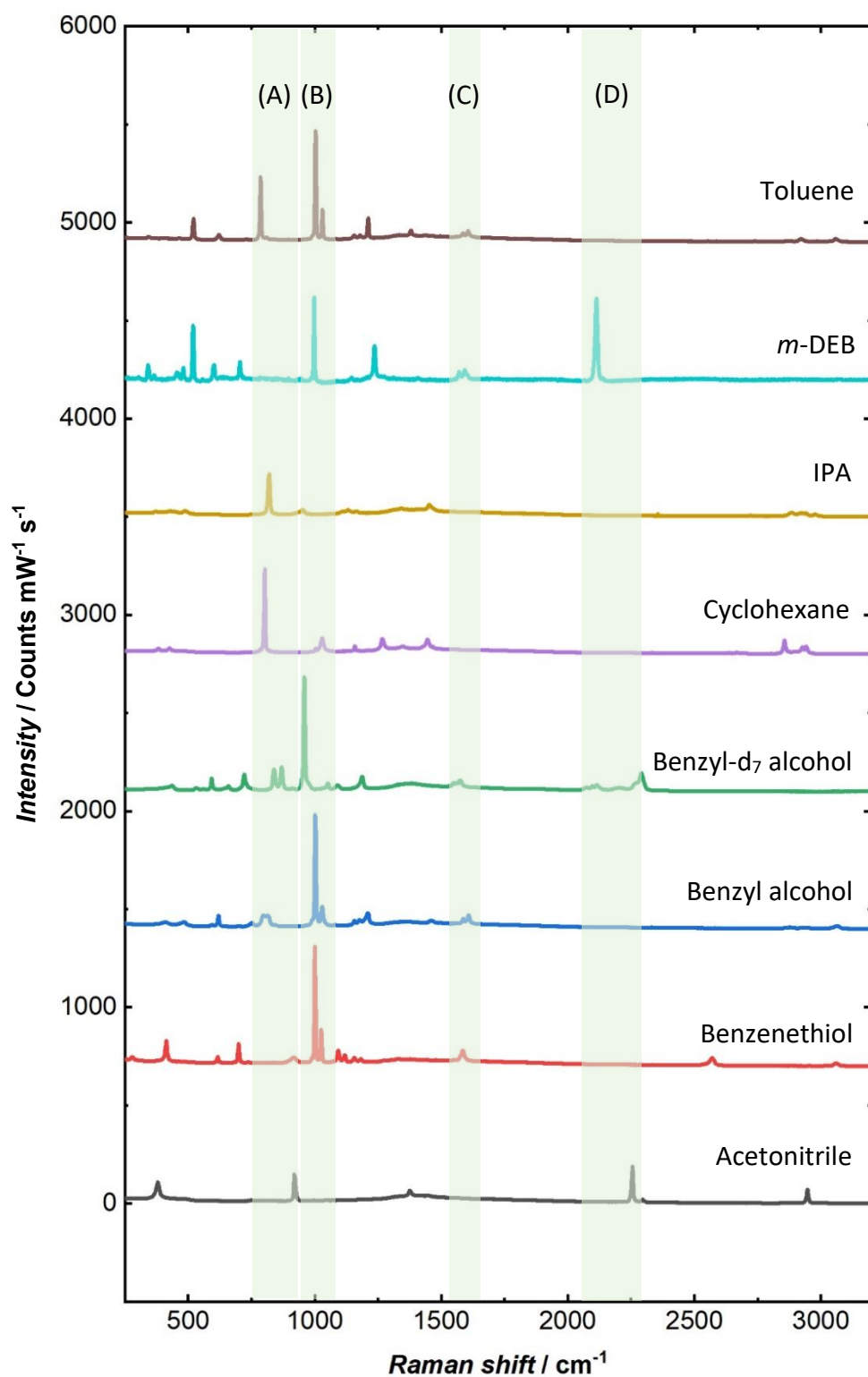


Figure 32 Raman spectra of the selected analytes which have been offset for clarity. Note: *m*-DEB and benzyl- d_7 alcohol were not measured under the standard conditions and have been scaled for visual purposes. The regions of interest are highlighted as (A) C-C stretching, (B) ring breathing, (C) C=C stretching, (D) triple bond stretching.

Table 13 Experimentally determined relative cross-sections of the liquid analytes, focussed on the C-C stretch (A) in Figure 32. Cyclohexane C-H stretch has been included. Peak intensity is the average over five measurements, showing the standard deviation.

Analyte	Peak centre / cm^{-1}	Concentration / M	FWHM / cm^{-1}	Integrated peak intensity	Relative Raman cross section / $10^{-30} \text{ cm}^2 \text{ molecule}^{-1} \text{ sr}^{-1}$
Acetonitrile	920	19.15	7.31	1164.49 ± 11.80	0.323 ± 0.003
Cyclohexane	802	9.26	5.05	2496.09 ± 34.10	1.430
Cyclohexane (C-H)	2900	9.26	27.63	2405.52	1.378
IPA	820	13.06	7.85	1855.65 ± 223.36	0.754 ± 0.09

Equation 4.3 was used to calculate the relative cross-sections from the average value of the integrated peak intensity of each of the analytes. It should be noted that although the 802 cm^{-1} peak of cyclohexane was used as the standard for the whole spectral region, there will be some errors as a result of the instrument response function which has not been corrected for. This is particularly evident in the C-H stretching region, which should have an integrated intensity $8.4\times$ that of the C-C stretch. The poor response of the CCD detector in this region when using 785 nm excitation leads to lower than expected intensities being recorded.

Table 14 Experimentally determined cross-sections of the ring-breathing mode 12 of the aromatic analytes, (B) in Figure 32.

Analyte	Peak centre / cm^{-1}	Concentration / M	FWHM / cm^{-1}	Integrated peak intensity	Relative Raman cross section /
---------	--------------------------------	-------------------	-------------------------	---------------------------	--------------------------------

					10^{-30} cm^2 $\text{molecule}^{-1} \text{ sr}^{-1}$
Benzenethiol	1002	9.74	4.77	3557.97 ± 244.22	1.820 ± 0.12
Benzyl alcohol	1002	9.66	5.49	4124.69 ± 23.11	2.265 ± 0.01
Toluene	1003	9.39	4.83	3262.27 ± 240.66	1.843 ± 0.14
<i>m</i> -DEB	998	7.52	4.84	3215.05	2.268

The ring-breathing mode 12 is very intense for mono, and meta-disubstituted benzenes.¹⁰⁴ Hence, it has been chosen to compare the four aromatic analytes. *m*-DEB has a ring-breathing mode with a cross-section greater than that of toluene and benzenethiol as a result of the increased conjugation given by its two acetylene substituents. Additionally, the larger substituent on benzyl alcohol is responsible for the increase the cross-section of the 1000 cm^{-1} mode relative to benzenethiol and toluene.

Table 15 Experimentally determined cross-sections of the aromatic C=C stretches.(C) in Figure 32.

Analyte	Peak centre / cm^{-1}	Concentration / M	FWHM / cm^{-1}	Integrated peak intensity	Relative Raman cross section / 10^{-30} cm^2 $\text{molecule}^{-1} \text{ sr}^{-1}$
Benzenethiol	1586	9.74	12.99	804.87 ± 43.77	0.438 ± 0.02
Benzyl alcohol	1600	9.66	18.13	708.15 ± 10.79	0.389 ± 0.01
Toluene	1598	9.39	19.11	456.28 ± 46.86	0.258 ± 0.03
<i>m</i> -DEB	1585	7.52	26.33	2767.749	1.952

The vibrational modes 8a and 8b correspond to C=C stretching modes within the aromatic ring. The intensity of these bands is related to the electronic properties of the substituent. The intensity of vibration 8a increases with conjugation, or where electron-

withdrawing substituents are used. The monosubstituted benzenes all display similar results, but the mass of the sulfur atom gives benzenethiol a slightly higher intensity. For meta-substituted benzenes, having identical substituents increases the intensity of this vibrational pair, explaining why the cross-section is greater for *m*-DEB in this selection of analytes.¹⁰⁴

Table 16 Experimentally determined cross-sections for the triple bond stretches. (D) in Figure 32.

Analyte	Peak centre / cm^{-1}	Concentration / M	FWHM / cm^{-1}	Integrated peak intensity	Relative Raman cross section / $10^{-30} \text{ cm}^2 \text{ molecule}^{-1} \text{ sr}^{-1}$
Acetonitrile	2256	19.15	7.27	1889.40 ± 11.12	0.523 ± 0.01
<i>m</i> -DEB	2114	7.52	10.95	10925.08	7.707

Table 16 shows the large contrast between relative cross-sections measured in the triple-bond stretching region for acetonitrile and *m*-DEB. The more polarizable ethynyl group compared to the nitrile group may explain a small contribution to this difference. However, the conjugation of the $\text{C}\equiv\text{C}$ triple bond to the aromatic ring structure is likely responsible for most of the difference. In contrast, the nitrile group is attached to a small, non-polarizable CH_3 group. If benzonitrile were investigated, then it would be expected to possess a cross-section between these two extremes.

The integrated area of the C-H region has not been investigated in detail as the bands are very weak and often overlapping. This led to a significant deviation between repeats, making it difficult to determine a meaningful average. The aromatic C-H stretch remains at $3060\text{-}3070 \text{ cm}^{-1}$ for the aromatic analytes suggesting that this vibration is relatively unaffected by the substituent in terms of frequency or intensity. Between $2900\text{-}3000 \text{ cm}^{-1}$, the symmetric CH_3 stretch can be observed for toluene and the C-H asymmetric stretches for IPA and cyclohexane. Below 2900 cm^{-1} , the symmetric C-H stretches are observed for IPA and cyclohexane. The benzyl alcohol CH_2 stretches also appear in this region.

4.2.3 DFT determination of cross-section

DFT calculations were performed using Gaussian 09 software, using the B3LYP 6-311G++(d,p) basis set. No specific molecular axes were specified, and the molecules were treated as isolated molecules at 298 K. Molecules of interest were constructed using GaussView 6.1.1 software, and then the geometry was optimised using Gaussian and B3LYP 6-311G++(d,p) basis set. After the optimisation procedure, the molecules were subjected to a frequency calculation using the same basis set to give the predicted spectra and Raman activity for each vibrational mode. The molecules studied included: acetonitrile, benzenethiol, benzyl alcohol, benzyl-d₇ alcohol, benzonitrile, cyclohexane, toluene, *m*-DEB, and isopropyl alcohol.

To aid comparison between molecules, the data have been considered separately for each vibrational mode or region. The Raman activity was converted to Raman cross-section using Equation 4.5. To differentiate between gas phase molecules and the liquid samples studied here a correction factor has been applied. The correction factor is related to the refractive index n by:⁵⁹

$$\text{Correction factor} = \left(\frac{n^2 + 2}{3} \right)^4 \quad (4.6)$$

Using Equation 4.6, the cross-section of liquids is scaled up from the corresponding gaseous cross-section. For most simple solvents, this has a value from around 2.5-5.

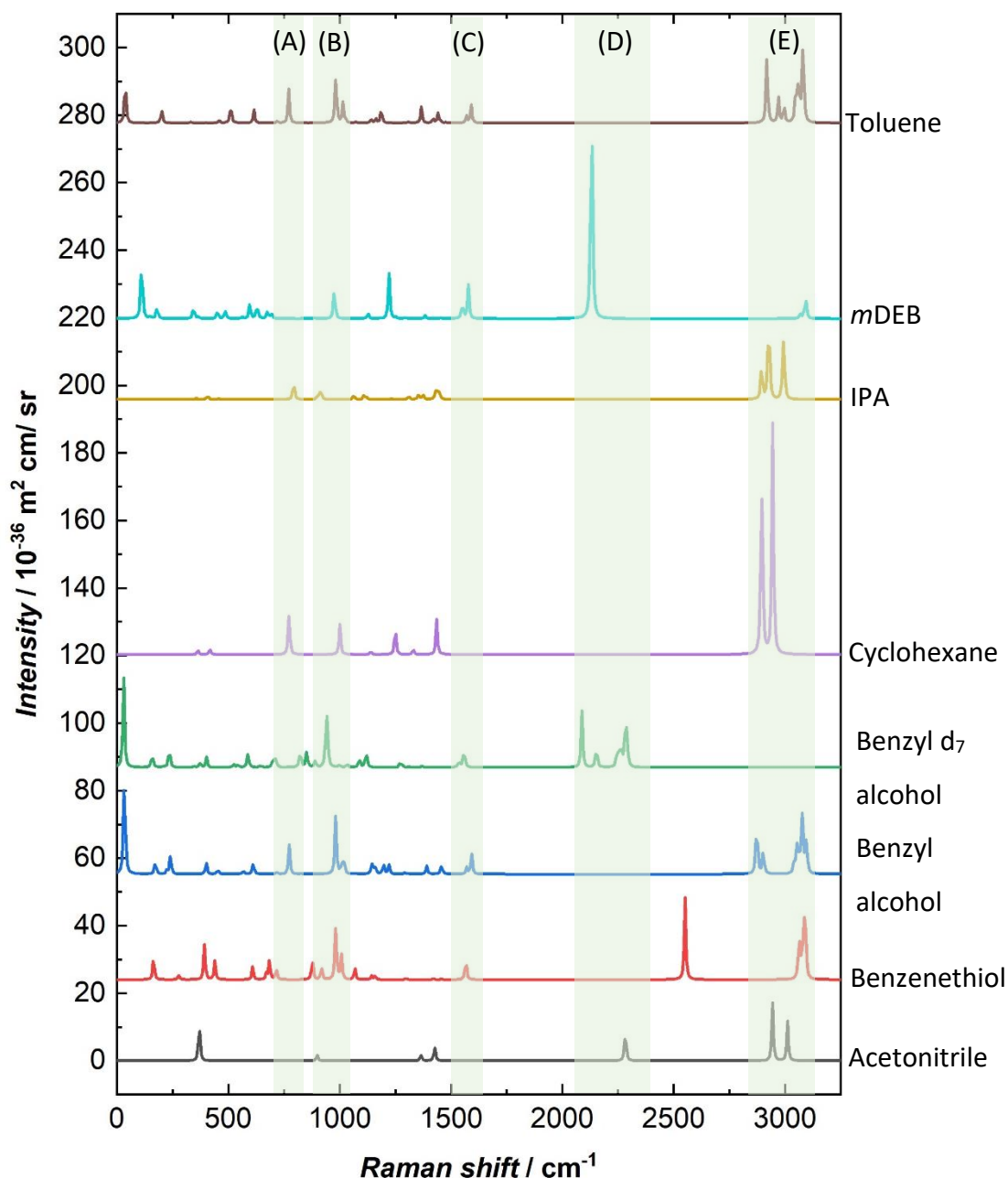


Figure 33 DFT Raman spectra of the solvents included in this study, using the B3LYP hybrid functional and 6-311G++(d,p) basis set. The spectra are offset for clarity, and the frequency has been scaled by 0.9668. The intensity of the spectrum of *m*-DEB has been divided by a factor of 4 to allow greater visualisation of the remaining spectra. Here (A) shows C-C stretching, (B) shows ring breathing, (C) is C=C stretching, (D) shows triple bonds and C-D stretching, and (E) is C-H stretching.

Table 17 DFT calculations of the Raman cross-section using hybrid functional B3LYP and 6311G++(d,p) basis set. Showing the cross-sections for the aliphatic C-C stretch. (A) in Figure 33.

Analyte	Peak position / cm^{-1}	Raman activity / $\text{\AA}^4 \text{amu}^{-1}$	Refractive index	Correction factor	Raman cross section / $10^{-30} \text{cm}^2 \text{sr}^{-1}$
Acetonitrile	930	3.74	1.34	2.59	0.118
Cyclohexane	798	21.58	1.43	3.30	1.05
IPA	818	9.27	1.38	2.87	0.381

Table 17 shows the calculated cross-section of the C-C stretching mode of the aliphatic analytes. This is larger in cyclohexane, where the size and number of C-C bonds is greater compared to IPA and acetonitrile. The DFT calculations predict the cross-sections in the order MeCN < IPA < cyclohexane matching the order found in the experimental procedure. A limitation in these DFT calculations was that intermolecular interactions were not accounted for, providing over- or underestimates for the DFT cross-sections. Correcting for this would require significant computational time, but an increase in the cross-section has been observed for a toluene molecule “solvated” in toluene using a minimal basis set (data not shown).

Table 18 DFT calculations of the Raman cross-section using hybrid functional B3LYP and 6311G++(d,p) basis set. Showing the cross-sections for the aromatic ring-breathing.(B) in Figure 33.

Analyte	Peak position / cm^{-1}	Raman activity / $\text{\AA}^4 \text{amu}^{-1}$	Refractive index	Correction factor	Raman cross section / $10^{-30} \text{cm}^2 \text{sr}^{-1}$
Benzenethiol	1014	46.76	1.59	5.19	2.62
Benzonitrile	1016	47.38	1.53	4.38	2.24
Benzyl alcohol	1016	38.04	1.54	4.51	1.85
Benzyl- d_7 alcohol	973	38.45	1.54	4.51	1.98
<i>m</i> -DEB	1010	85.99	1.58	5.05	4.72
Toluene	1017	35.19	1.50	4.03	1.53

Table 18 shows the characteristic ring-breathing mode for the aromatic analytes. This is the most intense ring band observed in the experimental and calculated data. Here, the cross-section increases in the order: toluene < benzyl alcohol < benzyl- d_7 alcohol < benzonitrile < benzenethiol << *m*-DEB. This contrasts with the experimentally determined order of benzenethiol \approx toluene < benzyl alcohol \approx *m*-DEB. It is possible that this mode is sensitive to environmental changes, which would explain the differences for DFT versus experimental values.

Table 19 DFT calculations of the Raman cross-section using hybrid functional B3LYP and 6311G++(d,p) basis set. Showing the cross-sections for the aromatic C=C stretches. (C) in Figure 33.

Analyte	Peak position / cm^{-1}	Raman activity / $\text{\AA}^4 \text{amu}^{-1}$	Refractive index	Correction factor	Raman cross section / $10^{-30} \text{cm}^2 \text{sr}^{-1}$
Benzonitrile	1641	91.65	1.53	4.38	2.15
Benzenethiol	1621	54.41	1.59	5.19	1.54
Benzyl alcohol	1636	35.87	1.54	4.51	0.871
Benzyl- d_7 alcohol	1600	33.89	1.54	4.51	0.853
Toluene	1634	31.02	1.50	4.03	0.675
<i>m</i> -DEB	1583	51.36	1.58	5.05	1.47

For the vibrational modes centred around 1600 cm^{-1} , the cross-sections are reported in the order: toluene < benzyl- d_7 alcohol < benzyl alcohol < *m*-DEB < benzenethiol < benzonitrile. This agrees with the experimental results.

Table 20 DFT calculations of the Raman cross-section using hybrid functional B3LYP and 6311G++(d,p) basis set. Showing the cross-sections for the triple bond stretches.(D) in Figure 33.

Analyte	Peak position / cm^{-1}	Raman activity / $\text{\AA}^4 \text{amu}^{-1}$	Refractive index	Correction factor	Raman cross section / $10^{-30} \text{cm}^2 \text{sr}^{-1}$
Acetonitrile	2363	71.76	1.34	2.59	0.529
Benzonitrile	2333	437.43	1.53	4.38	5.59
<i>m</i> -DEB	2205	1975.75	1.58	5.05	32.3

The cross-section for the analytes containing triple bonds increases in the expected order, with the large cross-section of the *m*-DEB $\text{C}\equiv\text{C}$ triple bond vibrations being of particular significance.

Table 21 DFT calculations of the Raman cross-section using hybrid functional B3LYP and 6311G++(d,p) basis set. Showing the cross-sections for the C-H stretching region (E) in Figure 33.

Analyte	Peak position / cm^{-1}	Raman activity / $\text{\AA}^4 \text{amu}^{-1}$	Refractive index	Correction factor	Raman cross section / $10^{-30} \text{cm}^2 \text{sr}^{-1}$
Acetonitrile	3081	314.10	1.34	2.59	1.33
Benzenethiol	3177	554.91	1.59	5.19	4.40
Benzonitrile	3186	539.70	1.53	4.38	3.59
Benzyl alcohol	3087	836.64	1.54	4.51	6.15
Benzyl-d ₇ alcohol	2265	379.78	1.54	4.51	5.28
Cyclohexane	3026	1400.86	1.43	3.30	7.90
IPA	3035	706.31	1.38	2.87	3.43
<i>m</i> -DEB	3071	599.51	1.58	5.05	4.99
Toluene	3104	956.86	1.50	4.03	6.21

The cross-sections for the C-H (or C-D) stretching region are presented in Table 21. Whilst the accuracy of the experimentally derived cross-section of the cyclohexane C-H stretch limits its comparison to the DFT value, comparison of the DFT cross-section of $7.9 \times 10^{-30} \text{cm}^2 \text{sr}^{-1}$ with the measured C-C cross section of $1.05 \times 10^{-30} \text{cm}^2 \text{sr}^{-1}$ resembles the ratio given by McCreery of 8.4:1, validating the technique.

4.2.4 Comparison between DFT and experimental results

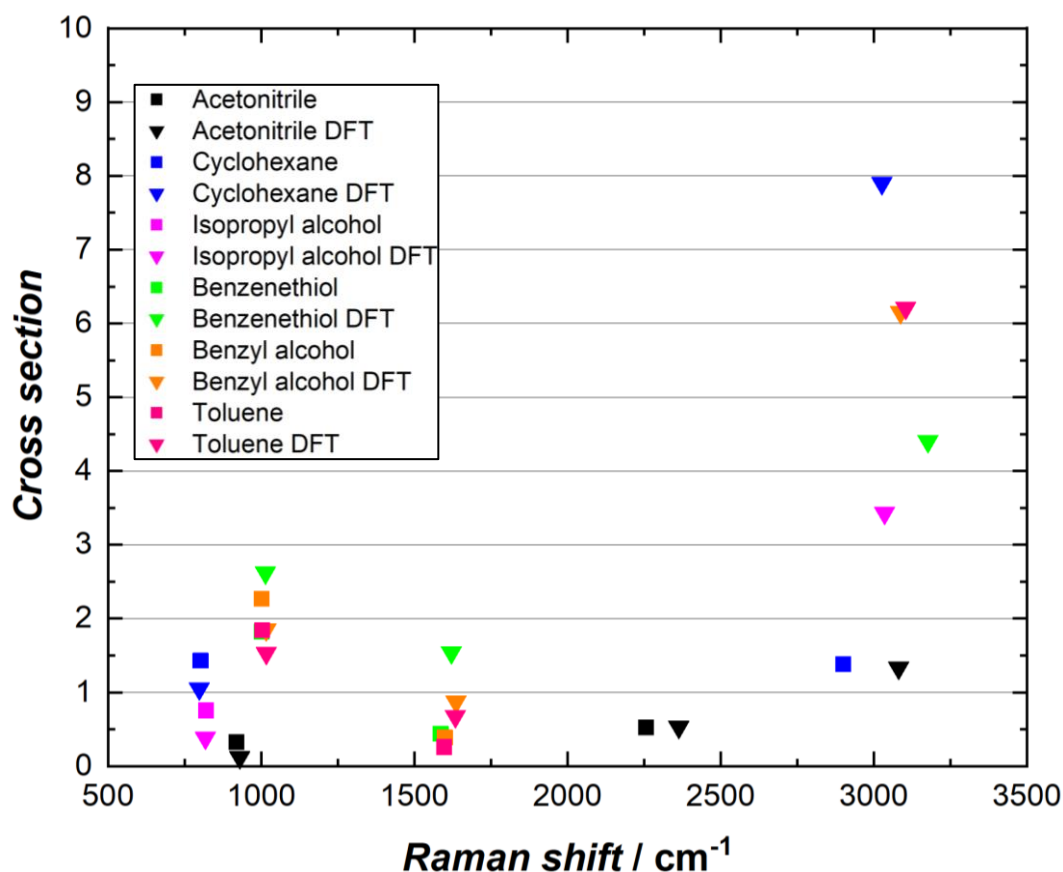


Figure 34 Graph showing the differences in the Raman cross-section calculated using DFT (triangles) and laboratory measurements (squares). The similarity of the two methods validates the DFT approach as a way of determining Raman cross-sections. Only cyclohexane has data for both experimental and DFT cross-sections in the C-H stretching region at approx. 3000 cm^{-1} .

The DFT and laboratory measurements correlate with each other and tend to follow the same trend, particularly at lower wavenumbers. There is a significant deviation between the measured results and the theoretical at greater wavenumbers, this is due to the collection efficiency of the CCD at longer wavelengths. Using the 785 nm excitation source, a shift of 3000 cm^{-1} correlates to a wavelength of over 1 micron, which is beyond the Si sensitivity range. This could be corrected for using a NIST standard to account for the work function of the spectrometer but would be specific and non-generalisable. Choosing a shorter excitation wavelength would also solve the problem, however, for this work, 785 nm excitation is of particular interest as it gives a limited background response with the Ta_2O_5 waveguide and for biological media.

Chapter 4

Other differences between the DFT and measured data result from the overestimation of the electron exchange correlation, which is a limitation intrinsic to DFT calculations, this means that the predicted Stokes shift is often greater than what is observed. The DFT data have been calibrated according to the basis sets used, but there are still some minor discrepancies. Factors that have not been accounted for with the DFT calculations are intermolecular forces and hydrogen bonding, the excitation wavelength, and temperature.

More in-depth studies could be carried out, using more computational resources and solvating the analytes, which may result in the DFT more closely resembling the experimental data. However, the data are sufficient for this project and reasonable confidence may be used in predicting trends in the absence of normalised, highly controlled measurements – which may not be possible for scarcely available or reactive compounds, and for establishing whether a potential analyte is worth investigating. Overall, the agreement is very good.

4.3 WERS spectra of bulk organic liquids

WERS spectra were recorded using the apparatus as described in Section 2.3.4. An additional external filter was required at the end of the collection fibre as the internal pump filter of the spectrometer was not able to successfully remove the pump light. Before addition of the analyte, a background was recorded with the waveguide exposed only to air. This provided a characteristic spectrum with a large signal observed at low wavenumbers.

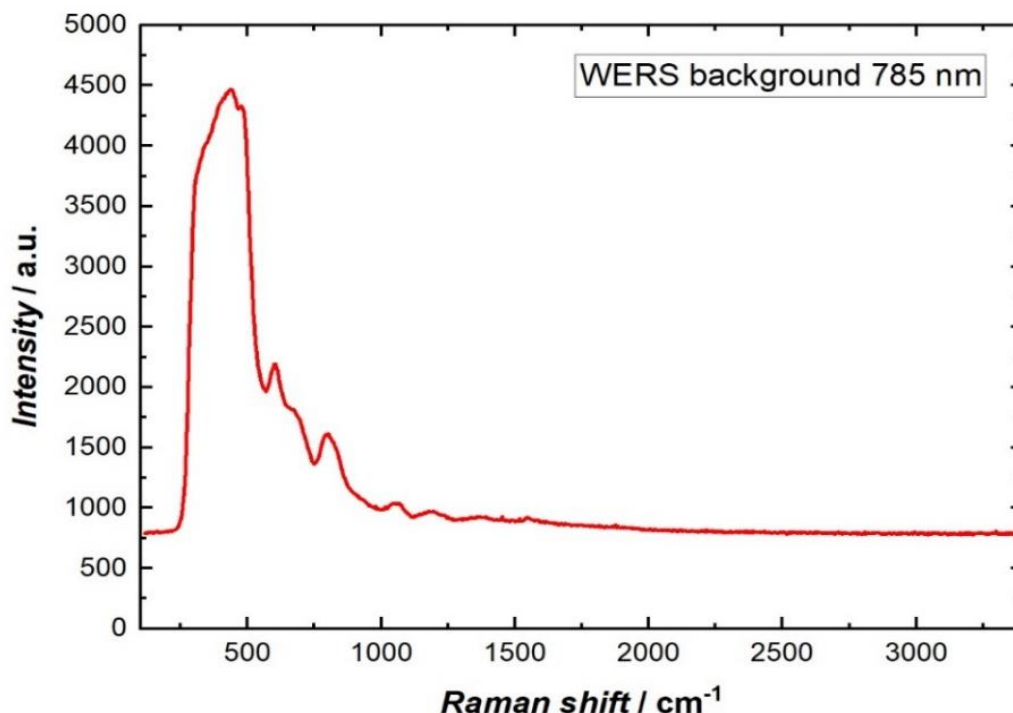


Figure 35 WERS background signal observed from a Ta₂O₅ waveguide chip exposed to air with 785 nm excitation. A significant background is observed between 250-1000 cm⁻¹ intrinsic to vibrations in Ta₂O₅.

4.3.1 *m*-Diethynylbenzene

m-Diethynylbenzene (*m*-DEB) was chosen as the first analyte for WERS spectroscopy at 785 nm. The aromaticity combined with two acetylene substituents give rise to a strong Raman signal observed over a wide vibrational frequency range. The WERS background shown in Figure 35 has a significant background within the fingerprint region of many molecules, which may interfere with their detection. *m*-DEB contains two carbon-carbon triple bonds which scatter light in the silent region of the spectrum. A study by King *et al.* has discussed the vibrational assignments of *o*-, *p*-, and *m*-diethynylbenzenes and their deuterated analogues in detail.¹⁰⁵ Figure 36 shows the spectra of *m*-DEB measured using Raman and WERS techniques, which has been scaled and offset for clarity.

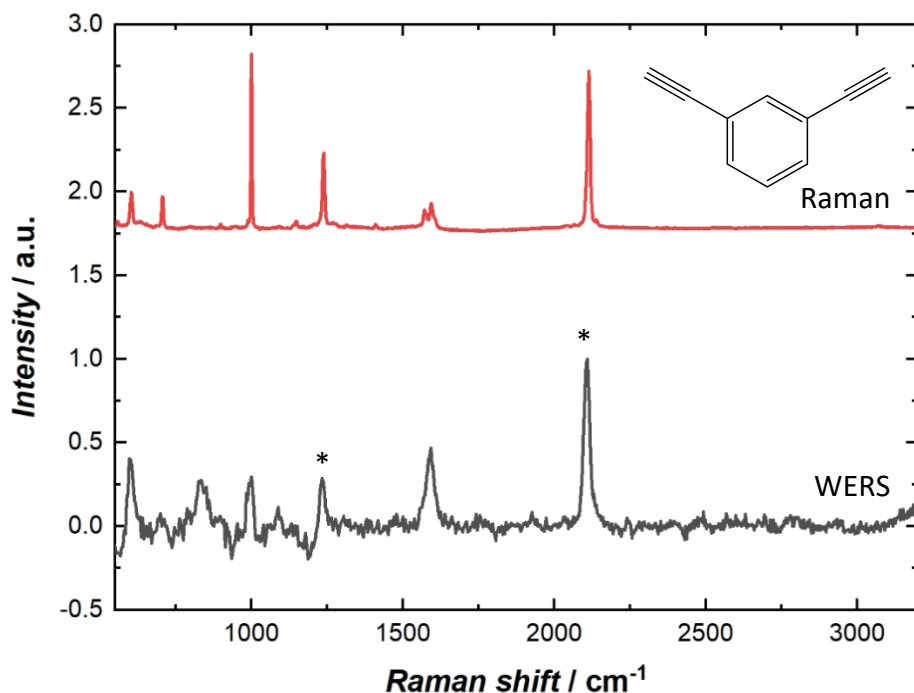


Figure 36 Raman and WERS spectra of *m*-diethynylbenzene. For WERS, a 2 μL droplet of *m*-DEB was placed on the surface of a Ta_2O_5 waveguide. 785 nm light was coupled into the waveguide using a grating. The acquisition time was 5 s. For Raman, a droplet of *m*-DEB was placed on a microscope slide.

There was a significant background signal towards the lower frequency range in both the Raman and WERS measurements of *m*-DEB, which has been attributed to fluorescence. The WERS spectrum shown is based on a single measurement and a 5 s acquisition time, although the spectrum was observed with acquisition times as low as 0.7 s. 5 s was the maximum time possible without saturating the detector. The Raman spectrum is an average of three measurements with a 1 mW, 785 nm excitation source, and 10 s acquisition time. The main peaks observed in the Raman spectrum are clearly visible in WERS, although the relative intensities are affected and there is a slight downshift in frequency for the substituent bands (highlighted with *) in the WERS spectrum.

Table 22 *m*-DEB vibrational frequencies and assignments made by King.(ref) The shift is that recorded in the Raman spectrum, with the WERS results in brackets where the two differ.

Raman shift / cm^{-1}	Assignment
2113 (2108)	$\nu(\text{C}\equiv\text{C})$
1594	8b
1568	8a
1238 (1235)	13
1087	18a
999	12
705	1
602	16a

The broad signal at around 700 cm^{-1} which is present in WERS does not appear to arise from a vibrational mode of *m*-DEB.¹⁰⁵ It is likely that this is a signal from the waveguide that is not removed by background subtraction. This could arise as a result of the refractive index change when placing a droplet of the analyte on the waveguide compared to the reference spectrum that was taken in air. With this analyte, the relative intensity of the WERS bands is different to that in conventional Raman measurements. It is possible that some of the discrepancy is due to subtraction of the fluorescence background, which would explain why the general trend is a loss of intensity towards the lower frequency region. However, these differences may indicate an interaction at the surface of the waveguide inducing an orientation of the molecule, which would be averaged in the bulk.

The frequency of the triple bond stretching mode shifts from 2113 cm^{-1} in Raman to 2108 cm^{-1} in WERS measurements. The signal observed near 1600 cm^{-1} covers a broad range from $1549\text{-}1624 \text{ cm}^{-1}$ with two clear features in the Raman and one clear feature in WERS. This is likely a resolution limit of the WERS spectrometer, as a shoulder can be observed, and there is no apparent shift between the WERS and Raman scattered frequencies. The C-X stretching mode is also affected with WERS versus Raman measurements; the

frequency is downshifted by 4 cm^{-1} for WERS. The frequency of the out of phase ring breathing mode remains at 999 cm^{-1} for both measurements, however the intensity is much lower for WERS. The 602 cm^{-1} band appears in both, but is twice as intense as in WERS when using the ratio of this peak to the triple bond peak. The 705 cm^{-1} feature is also very weak in WERS.

The peaks that have shifted in the WERS are related to the substituent stretching modes, which may indicate that there is some interaction with the Ta_2O_5 surface in the WERS measurements. IR studies demonstrate the interaction of hydroxyl species on an acidic metal oxide support with the C-C triple bond of acetylene, methylacetylene and *tert*-butylacetylene resulting in a small red shift in the frequency on adsorption compared to the free molecule.^{106,107} There is no evidence to suggest the formation of a hydrogen bond between the acetylene hydrogen and oxygen sites on the Ta_2O_5 substrate. The fact that the characteristic aromatic bands remain unshifted suggests that the primary interaction with the surface is with the acetylene functionality and not through interactions with the ring π -system.¹⁰⁸ As the intensity of vibrational modes 1 and 12 is low in the WERS spectrum, this could indicate an orientation of the ring parallel to the waveguide surface, although this is unclear.

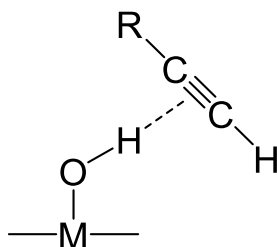


Figure 37 The proposed interaction between the alkyne and weakly acidic hydroxyl sites

4.3.2 Benzyl alcohol

The Raman spectra of benzyl alcohol (BA) and benzyl- d_7 alcohol (d_7 BA) are shown in Figure 38 to illustrate the frequency shifts that occur upon deuteration. With WERS, the background measurement was taken in air and subtracted from the final spectrum. The spectra have been normalised to the ring-breathing mode at 1002 cm^{-1} for BA and 959 cm^{-1} for d_7 BA and offset for visual purposes. As expected, very clear distinctions can be made between BA and d_7 BA as a result of deuteration. This is observed in both the Raman and WERS spectra. Unlike with *m*-DEB, the relative intensities of the bands in the WERS

and Raman spectra are similar. However, the WERS and Raman frequencies differ for both analytes.

The C-H vibrational modes can be seen in the 2870-3070 cm^{-1} region for BA. At 3065 cm^{-1} , the aromatic C-H stretch is observed. This shifts to 3059 cm^{-1} using WERS and is a very weak band.¹⁰⁹ For WERS, this band is weak because the scattered light at this frequency is poorly guided by the waveguide. With 785 nm excitation, scattering from a C-H vibration corresponds to light at 1027 nm, which makes it difficult to collect and detect a signal. Bands associated with the methylene hydrogens are observed only in the Raman. In d_7BA , the substitution of D for H results in a large frequency shift to lower wavenumbers. The resulting bands are more intense and can be observed in both the Raman and WERS spectra. The aromatic C-D vibration appears at 2271-2291 cm^{-1} . The bands between 2076-2116 cm^{-1} represent the CD_2 stretches.¹⁰⁹

The C=C stretching modes are visible in BA at 1608 cm^{-1} and 1589 cm^{-1} , and a small shift is observed in d_7BA at 1577 cm^{-1} and 1550 cm^{-1} . With Raman, these can be resolved into a pair representing the 8a and 8b modes. The C-C-H ring deformation band (18a) at 1029 cm^{-1} is clearly resolved from the ring breathing mode (12) at 1002 cm^{-1} in the BA Raman spectrum. With WERS, the 18a band is visible as a shoulder, and the two bands are downshifted by 2-3 cm^{-1} . The equivalent bands for d_7BA are at 959 cm^{-1} and 870 cm^{-1} . The remaining bands are shifted to a greater extent from the Raman to the WERS spectra which may be occurring due to interaction or hydrogen bonding with the surface.

Whilst the resolution of the WERS spectrometer may be a limiting factor for some applications, it has been shown to be a useful tool capable of giving good quality spectra that is sensitive enough to detect bands with low scattering cross-sections. Requiring only short acquisition times, this could be used to observe the adsorption kinetics of monolayers or proteins. Further improvements in the filtering of the excitation and scattered light may allow for longer acquisition times and improved signal to noise ratios. Benzyl alcohol has been shown to be a valuable solvent choice as the droplet remained in place for multiple measurements without evaporation, and spectra with several characteristic features was obtained in Raman and WERS measurements.

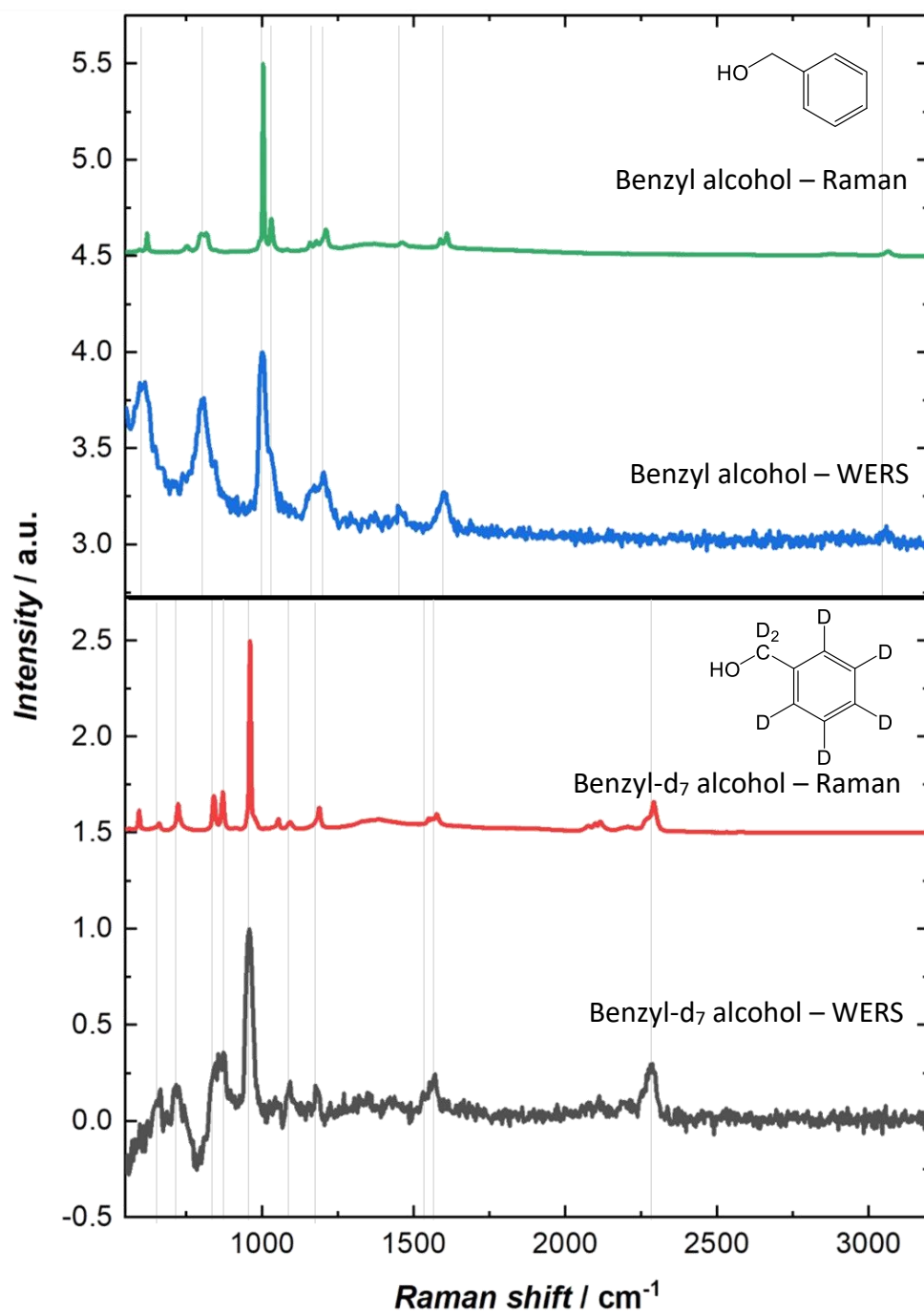


Figure 38 Overlaid Raman and WERS spectra showing benzyl alcohol and deuterated benzyl alcohol. The spectra have been scaled and offset for clarity, and lines have been added to aid comparison between peaks.

Table 23 The Raman shifts and assignment of benzyl alcohol. The figure in brackets represents the shift using WERS.

Raman shift / cm^{-1}	Assignment
3065 (3059)	2
1608 (1600 br)	8a
1590 (-)	8b
1460 (1448)	19b
1208 (1202 br)	v(C-CO)
1179 (1170 br)	9a
1158 (-)	15
1029 (1027)	18a
1002 (999)	12

Table 24 The Raman shifts and assignment of benzyl- d_7 alcohol. The figure in brackets represents the shift using WERS.

Raman shift / cm^{-1}	Assignment
2291-2271 (2287-2262)	2
1575-1549 (1568-1527)	8a, 8b
1186 (1181)	β (C-D)
1091 (1091)	β (C-D)
1052 (-)	v(C-CO)
959 (958)	12
870-841 (871-842)	18a

4.4 Summary

The Raman responses of several common laboratory solvents were investigated in this work. These were chosen due to their application in spectroscopic analyses, with cyclohexane, toluene, and IPA being used often as standards. Benzyl alcohol was identified as a suitable alternative to the more volatile and more hazardous solvents employed as standards and was later used as an example of using a standard solvent in the development of a new spectroscopic instrument. Cross-sections were determined through laboratory measurements, and computationally using DFT, with good levels of agreement between the two techniques. Discrepancies between the two methods occur where intermolecular interactions are not accounted for using the DFT method described here, and where there was a lack of response from the spectrometer at larger shifts. It is possible to account for intermolecular interactions using DFT, but this would increase the computational time. The response function of the spectrometer may also be accounted for using NIST SRM standards. However, for the bands of interest, these techniques provide useful and complementary information.

Small droplets of *m*-DEB, benzyl alcohol and deuterated benzyl alcohol were placed on the WERS instrument, and multi-featured spectra were obtained within a short length of time. These measurements were conducted where the maximum exposure time was 5 s before saturation occurred, the later acquisition of new optical components allowed this time to be extended and higher quality spectra to be obtained. This resulted in spectra with greater resolution and improved signal to noise. The improved results are depicted in Figure 39, noting that the data have been processed by background subtraction, a non-local means (NLM) de-noising algorithm, and spectral deconvolution. The WERS spectrum of *m*-DEB was not conducted using the refined instrument, nor were other solvents tested.

With the current set-up, conventional Raman spectroscopy is still capable of delivering higher quality spectra than the WERS spectrometer, even with the greater interaction length. This is partially due to instrumental factors – the resolution capability is not as high with the WERS spectrometer, limiting spectral detail. In addition, larger shifts are more difficult to observe with WERS, as inelastically scattered light is transmitted less effectively within the waveguide which is optimised for transmitting 785 nm light. This is

compounded by the reduced ability of the CCD to detect light with wavelengths above 1 μm . Addition of bulk solvents with high refractive indices is not within the optimal parameters for this WERS device, which is designed to work in air and aqueous solutions. With optimisation of the input laser, improving the collection efficiency, improving the waveguide, and filtering problems it is possible that WERS can reach the spectral quality of conventional Raman, with the potential to exceed its capability for surface-sensitive monitoring.

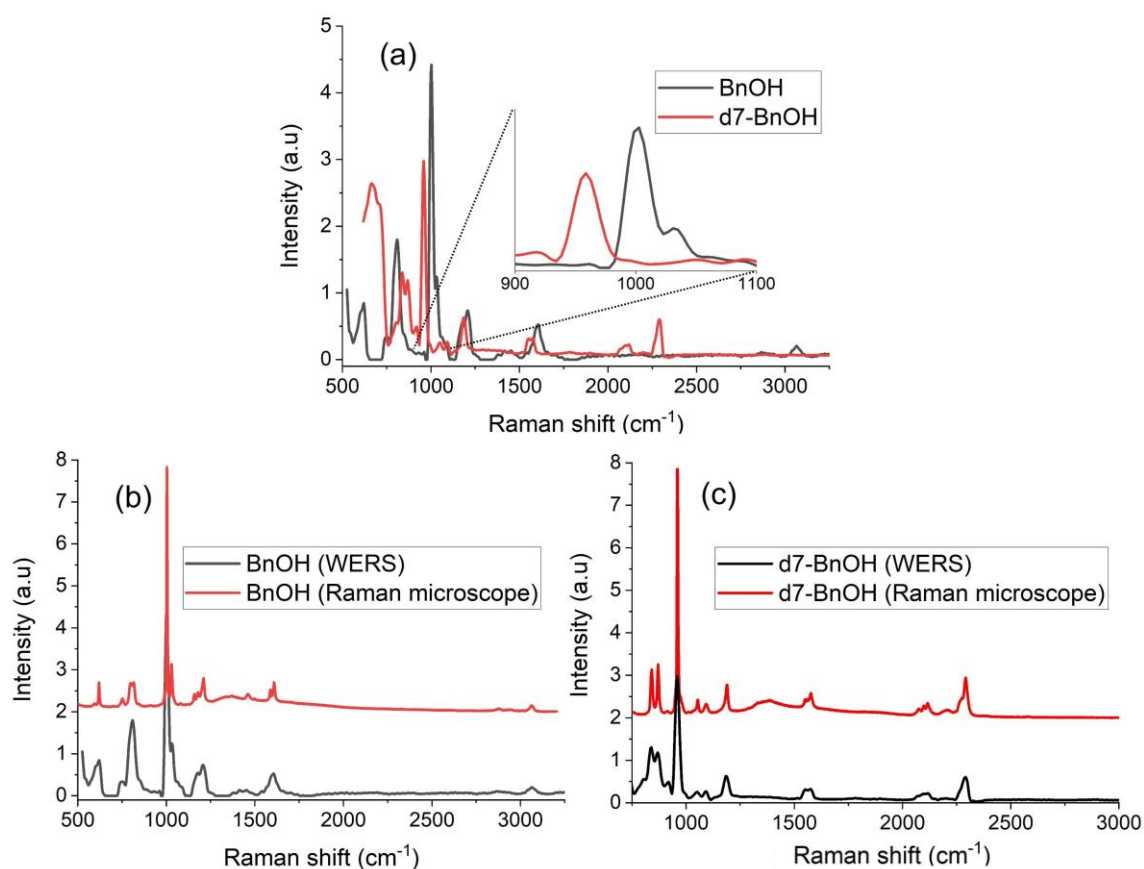


Figure 39 Raman and WERS spectra of benzyl alcohol and deuterated benzyl alcohol using 6.3 mW 785 nm laser. Spectra have been de-noised according to a non-local means algorithm and the background subtracted. Image taken from Ettabib *et al.* Grating-incoupled waveguide enhanced Raman sensor.

Chapter 5 SERS studies

5.1 Overview

This chapter looks at two types of SERS substrates, and how they interact synergistically together. Silver nanostars will be looked at, including the synthesis, a calculation of the enhancement factor achievable, and attempts at functionalisation. A gold sphere segment void (SSV) substrate will also be used, and its interaction with silver nanostars investigated with benzenethiol, aminobenzenethiol and nitrobenzenethiol will be looked at. The gold SSV substrate will also be used as a Raman enhancing substrate to show progress towards low-burden applications using paper fluidics.

Silver nanostars and gold SSV substrates have been produced and the SERS enhancement factor has been calculated for benzenethiol adsorbed on these substrates. In an effort to increase the enhancement factor, AgNS were deposited on the SSV substrate in an attempt to produce hot spots and create a combined enhancement effect within the SSV cavities. *p*-aminobenzenethiol has been used as an additional SERS analyte to increase the affinity of the SSV for AgNS, and to observe the enhancement of b_2 bands. The idea of using WERS and AgNS together is also proposed as a potential method for increasing the sensitivity of the WERS device, although ideally this technique would provide sufficient enhancement alone. Antibody-Raman tags are also produced, and a simple glucose sensor is shown.

5.2 Introduction to SERS substrates

SERS substrates, as discussed in the introduction, are typically composed of noble metals such as silver or gold. In order for plasmon modes to be supported, and for the SERS effect to arise, the metal must be rough at the nanostructure level. This means appropriately sized nanoparticles meet the criteria, as do roughened solid substrates. The roughening can be achieved through lithographic, electrochemical, etc. methods. With both nanoparticles and metallic surfaces, there is difficulty in reproducibility. Gold is particularly favoured as it forms biocompatible and stable nanoparticles and surfaces, although silver can give a greater theoretical enhancement.

5.2.1 Sphere segment void (SSV) substrates

Sphere segment void (SSV) substrates were devised in the University of Southampton as a method for creating reproducible, highly enhancing (10^6), robust surfaces. They have been used for a number of studies with DNA, and in defence research applications. They are produced by electrodepositing gold around a hexagonal array of polystyrene sphere standards (600 nm), then removing the template. This leaves a large surface area array of smooth, gold cavities like a honeycomb. Through careful selection of the deposition height, it is possible to channel incident light into the cavities by Bragg and Mie diffraction. As the incident light is amplified, so is the scattered light, leading to greatly enhanced Raman of items in the cavities.

5.2.2 Silver nanostars (AgNS)

The level of enhancement afforded by nanoparticulate material in SERS is strongly dependent on the materials used, the size and morphology of the nanoparticle. Nanoparticles with spherical morphology are simple to produce and have widely been used in SERS, but the lack of intrinsic hotspots requires that the nanoparticles be aggregated before an adequate signal enhancement is observed. The aggregation generates a number of hotspots at the junction between adjacent nanoparticles where the electromagnetic field enhancement is greatest. This type of aggregation is difficult to reproduce, and difficult to prevent from deactivation completely; in other words, the long-term stability of these substrates is low. Silver nanoparticles (AgNPs) in particular, are vulnerable to oxidation and over-aggregation. Controlled SERS substrates based on AgNPs are highly desirable due to the large LSPR intensity, meaning intense Raman signals may be produced.

In 2013, Garcia-Leis *et al.* proposed the synthesis of silver nanostars (AgNS) in a two-step reduction using mild reagents.²¹ The anisotropic nature of nanostars make them excellent SERS tools, with a large number of inbuilt hotspots at the points and nanojunctions.²¹ They showed that AgNS have an intrinsically high LSPR without the need for nanoparticle aggregation and have since described methods to tune the size, number of points, and the LSPR frequency of these nanoparticles making them very versatile for a number of applications.²² The authors recorded an enhancement factor of 10^6 for nanostars, compared to 10^4 for spherical nanoparticles. Previous reports for the synthesis of AuNS

had limited SERS applications, relying on the use of surfactants such as PVP or CTAB to control the morphology. These surfactants bind strongly to the surface of the AuNS meaning that SERS spectra are heavily influenced, both by the intensity of bands arising from these agents and by the inability for the target analyte to get within close proximity to the enhanced electric field at the nanostar.

The Garcia-Leis synthesis method uses hydroxylamine (HA) as a neutral reductant in the first step, which produces a number of highly faceted silver nanoparticles. AgNS are capped with citrate, a soft capping agent, which is added in the second step of the synthesis. The citrate group preferentially binds to the (111) facets in the growing nanoparticle, directing the anisotropic growth of the nanostar points. Careful control of [Ag⁺]:[HA], [HA]:[citrate], the stirring rate, temperature; and rate of addition allows AgNS to be morphologically tuned allowing different optical properties to be exploited.^{21,22}

Silver nanostars are versatile and can be used in several applications. For example, they have been drop-casted onto paper to produce plasmonic substrates that can be stored ready for use,¹¹⁰ used to characterise components in complex wine samples,¹¹¹ and used to detect traces of Congo Red as a marker for Alzheimer's disease.²² No direct biological functionalisation has been reported using AgNS.

5.3 Calculation of SERS enhancement factors

To test the effect that silver nanostars have on thiol monolayers, three simple aromatic thiols have been chosen. The enhancement factor (EF) is calculated using the spectra before and after enhancement, and then integrating the area under a chosen peak. Benzenethiol is the typical SERS probe for calculating the EF of a substrate.

$$\text{Enhancement factor (EF)} = \frac{I_{\text{SERS}} A_{\text{BT}} V_1 \rho_{\text{BT}} N_A}{I_{\text{Raman}} A_1 R M_{\text{BT}}} \quad (5.1)$$

In this equation: I_{SERS} represents the intensity of the peak measured on the SSV substrate which is determined by the peak height, A_{BT} is the area occupied by a single BT molecule (0.22 nm²), V_1 is the laser volume in neat BT (4160 μm³), ρ_{BT} is the density of neat BT (1.073 g cm⁻¹), N_A is Avogadro's constant (6.022 × 10²³ mol⁻¹), I_{Raman} is the intensity of the peak measured in neat BT, A_1 is the laser area (208 μm²), R is a geometrical roughness

factor based on the thickness of the structured substrate (equal to 3.32 for 80% thickness SSV, and 1 for a flat surface) and M_{BT} is the molecular weight of BT ($110.18 \text{ g mol}^{-1}$).

In this section, silver nanostars were deposited on thiolated flat gold and SSV surfaces to assess whether any combined enhancement effect may occur.

5.3.1 Benzenethiol

The SERS spectra are shown for benzenethiol (BT) adsorbed to gold SSV, on AgNS, and where a monolayer of BT was formed on the SSV and silver nanostars added. The Raman spectrum of benzenethiol is shown in Figure 32, page 72. Two vibrational modes were chosen – the C=C stretch at 1576 cm^{-1} , and the ring breathing mode at 1002 cm^{-1} . In both cases, BT monolayers with AgNS are the most enhanced, closely followed by the combined SSV and AgNS, followed by the SSV substrate.

A combined enhancement effect could have been expected to occur in the SSV and AgNS samples, but the coverage of silver nanostars within the cavities was not uniform, and the signal intensity varied between regions as a result. SSV surfaces are superhydrophobic and BT monolayers are also hydrophobic, resulting in aqueously suspended AgNS being repelled from the surface. AgNS also have a tendency to cluster together meaning there is an inhomogeneous surface coverage, thus signals are different depending on the area irradiated. The data shown here represent an average of multiple measurements.

Table 25 The enhancement factors calculated for the 1576 cm^{-1} band of benzenethiol.

Sample	Intensity of peak at 1576 cm^{-1} / Counts $\text{mW}^{-1} \text{ s}^{-1}$	Enhancement factor
Neat BT	48	-
AgNS	24865	1.34×10^7
SSV	11425	1.85×10^6
SSV + AgNS	64546	1.05×10^7

Table 26 The enhancement factors calculated for the 1002 cm^{-1} band of benzenethiol.

Sample	Intensity of peak at 1002 cm^{-1} / Counts $\text{mW}^{-1}\text{ s}^{-1}$	Enhancement factor
Neat BT	536	-
AgNS	22028	1.06×10^6
SSV	13236	1.92×10^5
SSV + AgNS	45965	6.66×10^5

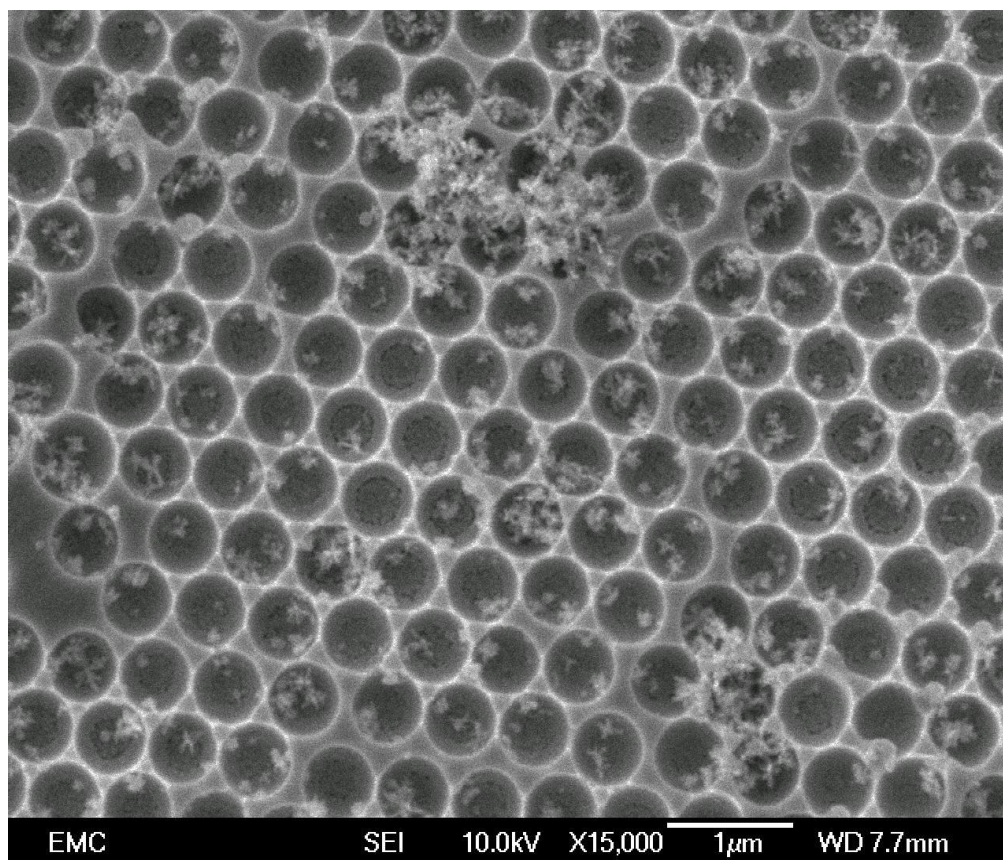


Figure 40 SEM image showing the distribution of silver nanostars on an SSV surface.

Accelerating voltage 10 kV, 15000 \times magnification, scale bar 1 μM .

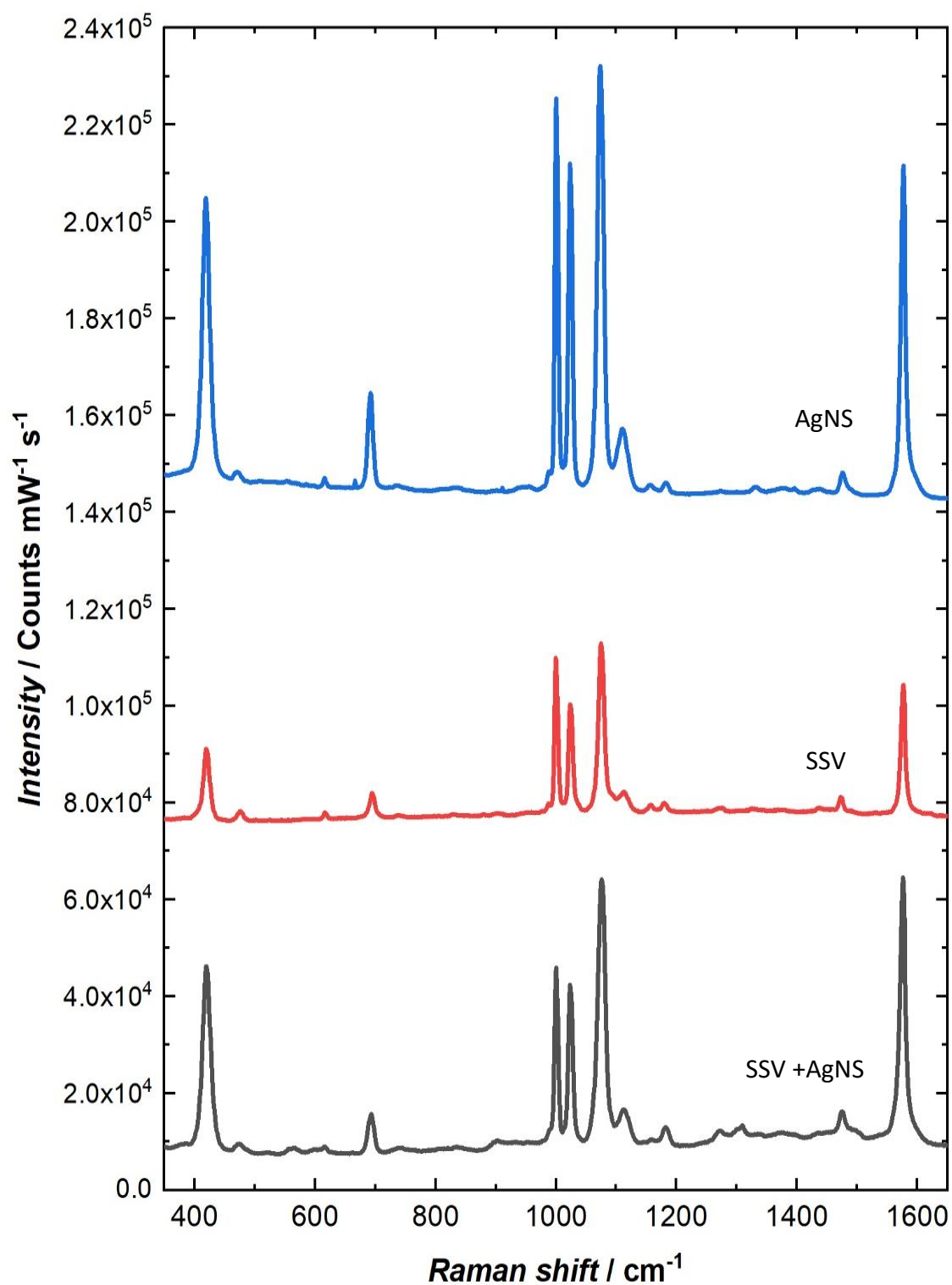


Figure 41 SERS spectra for benzenethiol monolayers on AgNS (top), SSV (middle), and combined AgNS and SSV substrates (bottom). The spectra have been normalised to counts $\text{mW}^{-1} \text{s}^{-1}$ and offset for clarity. 785 nm excitation.

No clear impact on the combined presence of SSV and AgNS was observed with respect to the enhancement factor, although a change in the relative peak heights could be consistently observed with the different substrates. The C=C stretch at 1576 cm^{-1} for example is greatly enhanced for each of the substrates but to a lesser extent for the SSV substrate compared to the AgNS substrates. The ring breathing band in the combined AgNS+SSV substrate is comparatively weaker compared to the isolated AgNS and SSV substrates. At 421 cm^{-1} , the C-S stretching and in-plane ring deformation is observed and is particularly strong in both the AgNS and SSV + AgNS substrates but is weak on only Au SSV. This may indicate a change in adsorbate orientation or selected enhancement of bands arising from charge transfer for example, as vibrations are enhanced most when perpendicular to the substrate. Selection of an out-of-plane mode to determine the EF may provide more information on the orientation, but the signal intensities are weak making comparison difficult.

The enhancement factors (EF) that have been calculated from these data are of the magnitude between 10^5 - 10^7 which is in line with these types of substrates reported in the literature.

5.3.2 Aminobenzenethiol

p-aminobenzenethiol (ABT) was chosen as an analyte as it is a simple, substituted benzenethiol where the amine substituent allows for exploration of the charge transfer mechanism, and provides a surface that is compatible with the silver nanostars. The exposed amine group is positively charged when exposed to the Ag colloid, hence an electrostatic attraction could contribute to the increased surface density of AgNS at the SSV surface. Material data sheets for ABT list it as a solid at room temperature, however the ABT analysed was a liquid. This is likely due to exposure to humidity. Without being able to quantify the water content, the assumption has been made for the following EF calculations that ABT is pure, the properties used for the BT calculations have also been used here. The spectra of ABT solutions were dominated by solvent peaks, hence the decision to use neat ABT. The unenhanced Raman spectrum for this material was collected by Nikolay Zhelev, and the integrated peak intensity plotted in Table 27 and Table 28.

Table 27 The enhancement factors calculated for the 1078 cm^{-1} band of ABT on SERS substrates.

Sample	Intensity of peak at 1078 cm^{-1} / Counts $\text{mW}^{-1} \text{s}^{-1}$	Enhancement factor
ABT	3230	-
AgNS	23681	1.76×10^5
SSV	7036	1.58×10^4
SSV + AgNS	5258733	1.18×10^7

Table 28 The enhancement factors calculated for the 1145 cm^{-1} band of ABT on SERS substrates.

Sample	Intensity of peak at 1145 cm^{-1} / Counts $\text{mW}^{-1} \text{s}^{-1}$	Enhancement factor
ABT	402	-
AgNS	21924	1.31×10^6
SSV	1872	3.37×10^4
SSV + AgNS	5692221	1.03×10^8

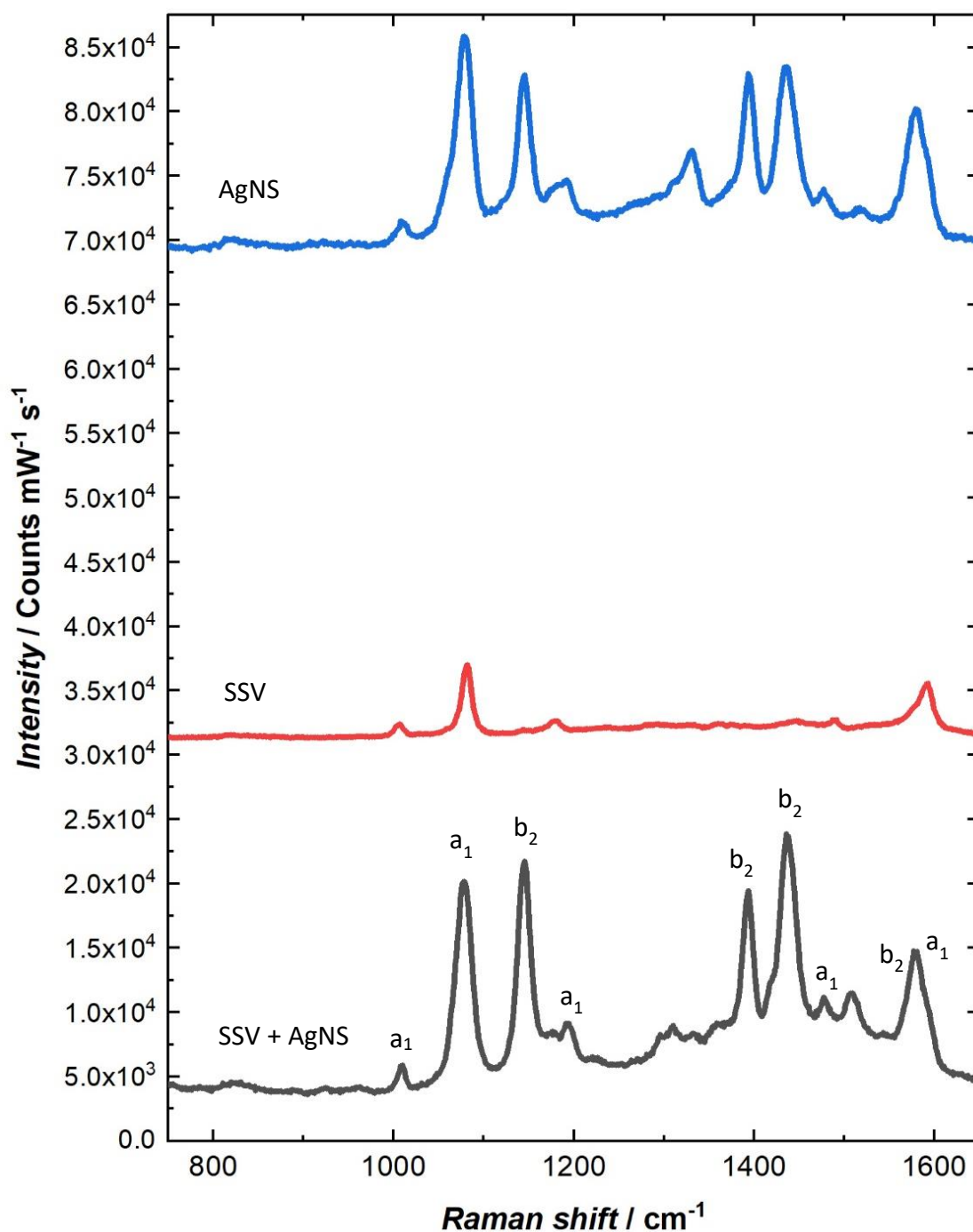


Figure 42 SERS spectra for *p*-aminobenzenethiol monolayers on AgNS (top), SSV (middle), and combined AgNS and SSV substrates (bottom), the intensity of this spectrum was divided by 100 to allow for comparison between the spectra. The spectra have been normalised to counts $\text{mW}^{-1} \text{s}^{-1}$ and offset for clarity. 785 nm excitation.

Chapter 5

When a monolayer of ABT is formed on an SSV substrate, there is preferential enhancement of the a_1 bands at 1005 cm^{-1} , 1078 cm^{-1} , 1179 cm^{-1} , 1491 cm^{-1} and 1592 cm^{-1} . In the cases where silver nanostars are present, the ABT molecules are sandwiched between gold and silver. In this case, both the a_1 and b_2 bands are enhanced.

The combined SSV and nanoparticle system greatly increases the EF. The amine group allows for a stronger interaction with the citrate capped AgNS and a greater occupancy of the SSV cavities is believed to occur as a result, producing a greater number of hot spots. As observed with BT, the signal intensity varied greatly between locations, indicating that the distribution of AgNS was not uniform. Electromagnetic enhancement arises from the coupling of the AgNS and SSV plasmons. On the SSV substrate, only the a_1 bands are enhanced when irradiated with a 785 nm laser. A difference is observed in the literature with shorter excitation wavelengths, SERS of ABT on gold and silver substrates of any geometry give rise to intense a_1 and b_2 bands.^{112–114} With AgNS and SSV + AgNS, the analyte can be sandwiched between the two metals and this results in the enhancement of the b_2 bands by an additional charge-transfer effect.

It should be noted that there is an alternative argument to the selective enhancement of b_2 bands has been presented in the literature, where the origin of the b_2 bands has been attributed to the photogeneration of the azo-compound 4,4'-dimercaptoazobenzene. There is evidence to support both hypotheses, but no clear consensus.^{112,113,115–118} In this work, the charge transfer hypothesis has been used to describe the SERS effect observed across the substrates tested. This is based on the evidence provided by Osawa¹¹² and Kim,¹¹⁶ who demonstrated that b_2 -type enhancements could be observed when using a derivative of ABT where the diazotisation reaction was prevented by the inclusion of protecting groups. In either case, there is significant enhancement of ABT when using AgNS as the SERS substrate.

5.3.3 Nitrobenzenethiol

Unlike BT and ABT, a monolayer of nitrobenzenethiol had a significant scattering cross-section such that it could be observed on a flat, gold coated microscope slide with 785 nm excitation (Figure 43). The strong band at 1333 cm^{-1} is characteristic of the highly polarizable symmetric NO_2 stretch. The relative enhancement factor given by the SERS substrates has been calculated assuming a well-packed monolayer on the flat gold substrate.

Silver nanostars deposited on the gold-coated microscope slide with NBT monolayer gave a small SERS enhancement relative to the enhancement levels observed with NBT monolayers on the SSV substrates (both with and without AgNS). This is depicted in Figure 44. The spectra are plotted on the same scale to allow visualisation of the magnitude of the enhancement afforded by each of the substrates.

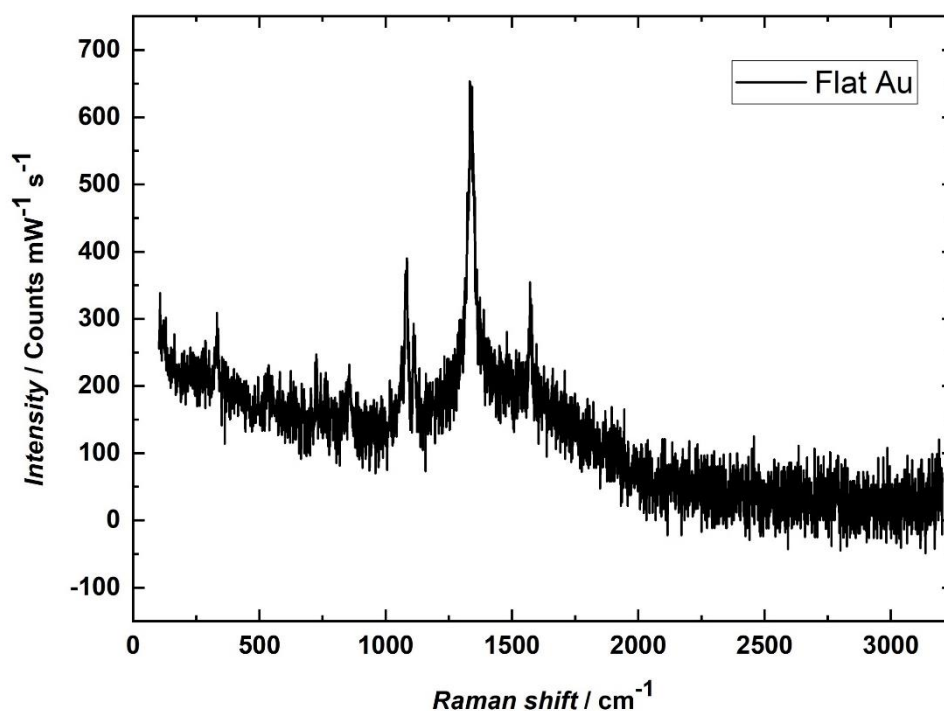


Figure 43 The Raman spectrum of a nitrobenzenethiol monolayer on flat gold coated microscope slide. Collection parameters: 785 nm excitation, 10 s, 0.05 mW.

Table 29 The enhancement of NBT monolayers on the selected substrates for the 1338 cm^{-1} peak, relative to that of NBT monolayer on a flat gold substrate.

Sample	Intensity of peak at 1338 cm^{-1} / Counts $\text{mW}^{-1} \text{s}^{-1}$	Enhancement relative to NBT monolayer on flat Au
NBT monolayer on Au	453	-
SSV	2046856	4.5×10^3
AgNS	37057	8.2×10^1
SSV + AgNS	13381400	3.0×10^4

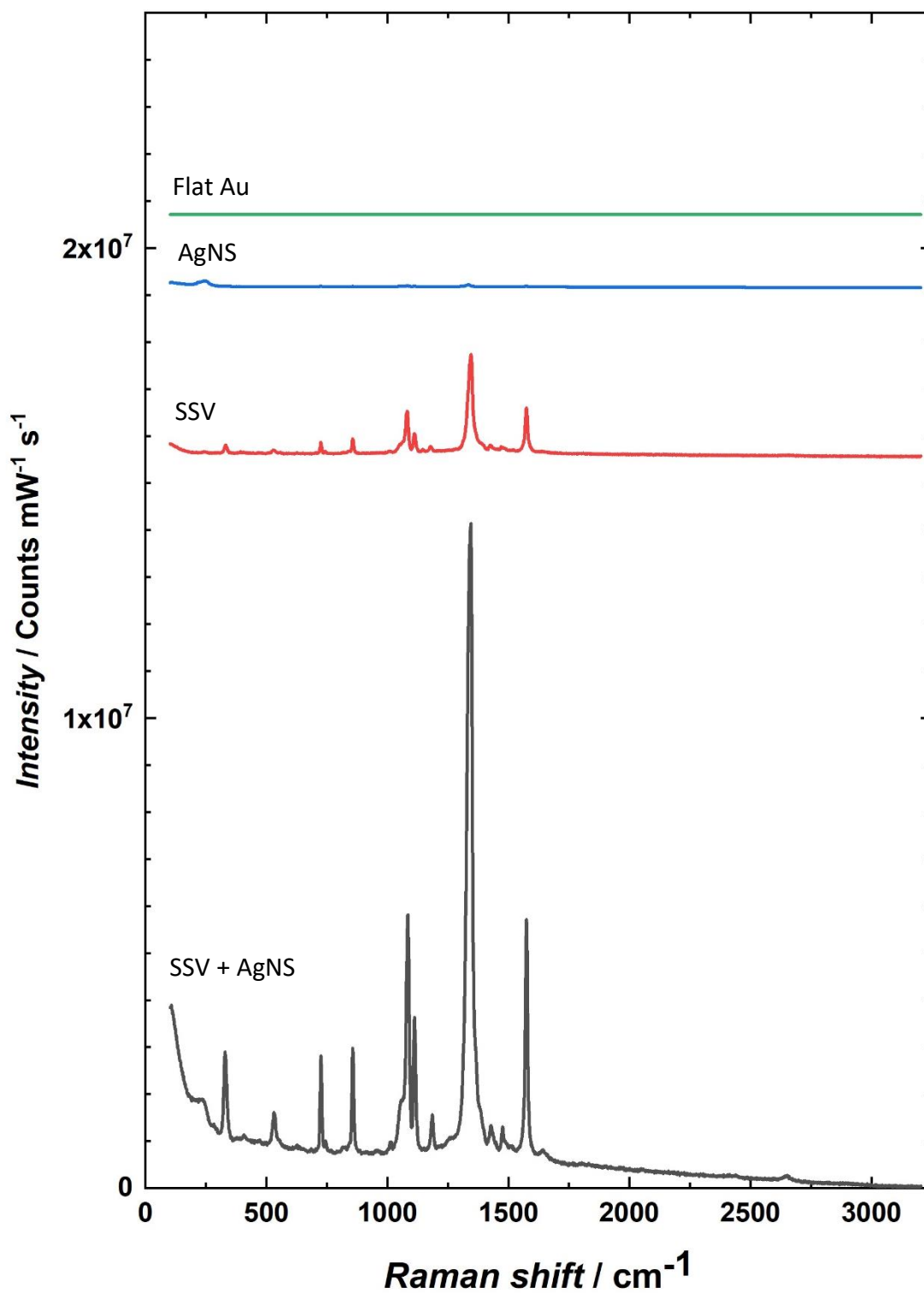


Figure 44 SER spectra showing NBT monolayers on different substrates, flat Au (top), AgNS, SSV, and SSV+AgNS (bottom). The spectra have been normalised to counts $\text{mW}^{-1} \text{s}^{-1}$ and offset for clarity.

5.4 Effects of SSV diameter on SERS

The effect of SSV diameter on the level of SERS enhancement was briefly investigated. Here 220 nm polystyrene sphere standards were used as the template. These were produced similarly to the 600 nm template (Section 2.1.1), except the thin layer cells were incubated at an 80° angle and the temperature reduced to 7.5°C, thus minimising the effects of Brownian motion on the spheres. Surface heterogeneity was more difficult to reach, with more defects and large areas of square packed arrays, although it is not clear how much of an effect the square packed arrays would have on the SERS effect. The 220 nm SSV substrates were iridescent and deep in colour, appearing a dark green or red depending on the observation angle.

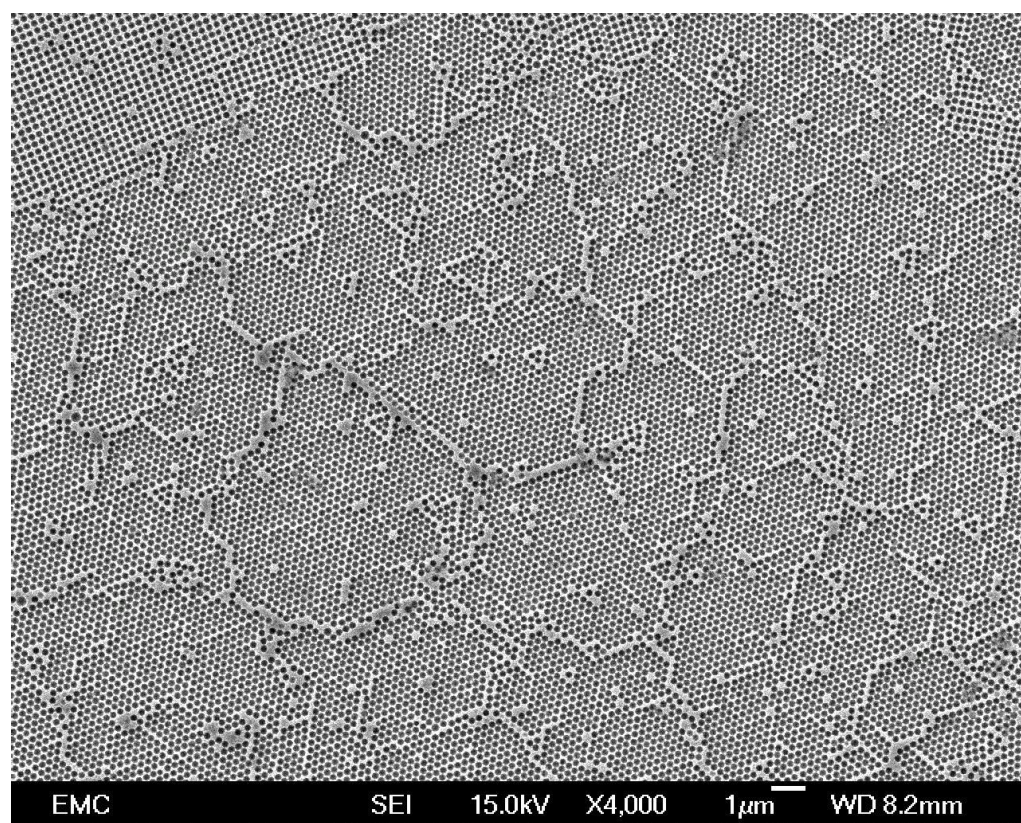


Figure 45 SEM image showing the long-range surface packing of an SSV substrate templated using 220 nm sphere standards. Accelerating voltage 15.0 kV, 4000x magnification, scale bar 1 μm.

The following spectra demonstrate the SERS effect produced from 220 nm SSVs compared to 600 nm SSVs for BT and ABT. 220 nm SSVs were chosen in part due to their smaller size matching the dimensions of the silver nanostars produced in this work. An investigation into the potential effect of accommodating a single nanostar inside each cavity was conducted, the spectra produced by AgNS with 600 nm and 220 nm SSV substrates are shown in Figure 46 and Figure 47.

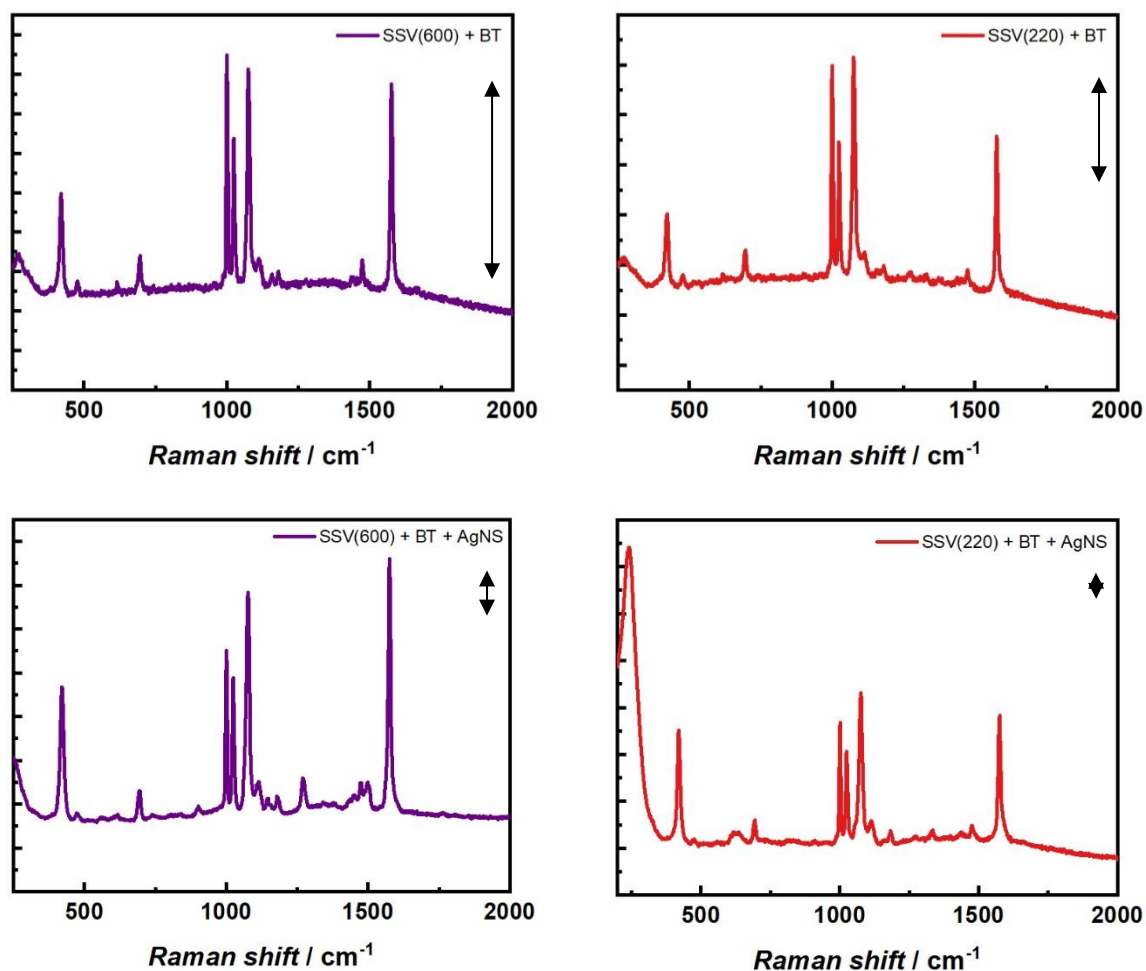


Figure 46 SERS showing a comparison between 600 nm and 220 nm SSV substrates for BT.

The double headed arrow in each spectrum indicates 10000 Counts $\text{mW}^{-1} \text{s}^{-1}$.

Top – in the absence of silver nanostars. Bottom – with silver nanostars in cavity.

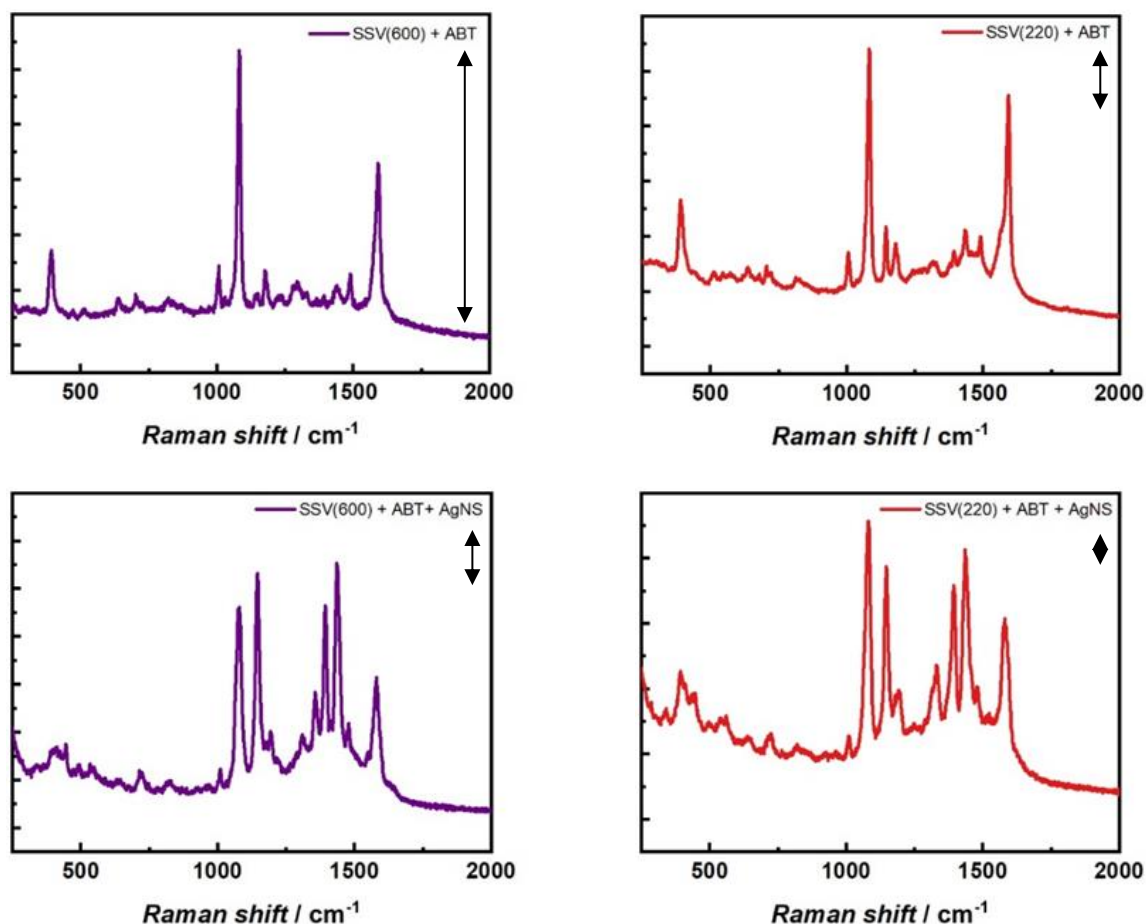


Figure 47 SERS showing a comparison between 600 nm and 220 nm SSV substrates for ABT. The arrows indicate $10000 \text{ Counts mW}^{-1} \text{ s}^{-1}$ (top spectra) and $10^6 \text{ Counts mW}^{-1} \text{ s}^{-1}$ (bottom spectra). Top – in the absence of silver nanostars. Bottom – with silver nanostars in cavity.

The enhancement factors afforded by the 220 nm SSV substrates, with and without the inclusion of silver nanostars was calculated for BT and NBT and tabulated for comparison with the 600 nm SSV substrates. The surface area of a flat substrate is 3.32x smaller than that of an ideal, hexagonally packed 220 nm and 600 nm SSV substrate with an electrodeposited height of 80% of the sphere diameter. The level of enhancement achieved by the SERS substrates is therefore not simply a factor of increased surface area. Any differences in enhancement between the 220 nm and 600 nm SSV substrates are also independent of surface area.

Table 30 Comparison of the enhancement factors calculated for BT and ABT on 600 nm and 220 nm SSV substrates with and without nanostars.

Analyte (band)	Substrate			
	600 nm SSV	600 nm SSV with AgNS	220 nm SSV	220 nm SSV with AgNS
BT (1002 cm^{-1})	1.92×10^5	6.66×10^5	3.17×10^5	7.71×10^5
BT (1576 cm^{-1})	1.85×10^6	1.05×10^7	2.09×10^6	9.35×10^6
ABT (1078 cm^{-1})	1.58×10^4	1.18×10^7	1.18×10^5	1.47×10^7
ABT (1145 cm^{-1})	3.37×10^4	1.03×10^8	2.43×10^5	7.44×10^7

There is a minor difference between the two SSV substrates with benzenethiol as the probe molecule. When these SSV substrates are combined with AgNS the enhancement factors are increased by a small, but not negligible amount, and this effect is more noticeable with the 1575 cm^{-1} band. The lack of reproducibility with AgNS dispersion in each substrate makes it difficult to determine whether the additional enhancement is originating from a nanostar-in-cavity effect, or from AgNS clusters.

With ABT, the differences between the two substrates are more apparent. The enhancement from the 220 nm SSVs is close to an order of magnitude greater than the 600 nm SSV. This trend is not observed with AgNS included within the cavities, where the enhancement factors for the 600 nm and 220 nm substrates are comparable. The greater enhancement of ABT compared to BT for the AgNS-SSV surface can be attributed to the hydrophilicity of ABT, leading to an attraction of AgNS to the SSV surface. It is unclear why greater differences can be observed for the SSV-only measurements for ABT *versus* BT.

Overall, the lack of reproducibility in AgNS dispersion on the SSV surfaces makes drawing valuable conclusions difficult from this data. While single nanostars could be accommodated in the cavities present (Figure 48) in the 220 nm SSV substrate, there was little control over the distribution, and most silver nanostars were present on the top surface of the SSV in large clusters, as was observed with the 600 nm SSV substrates. Pre-treatment of the gold SSV surface with hydrophilic or charged functional groups had little effect on improving the distribution.

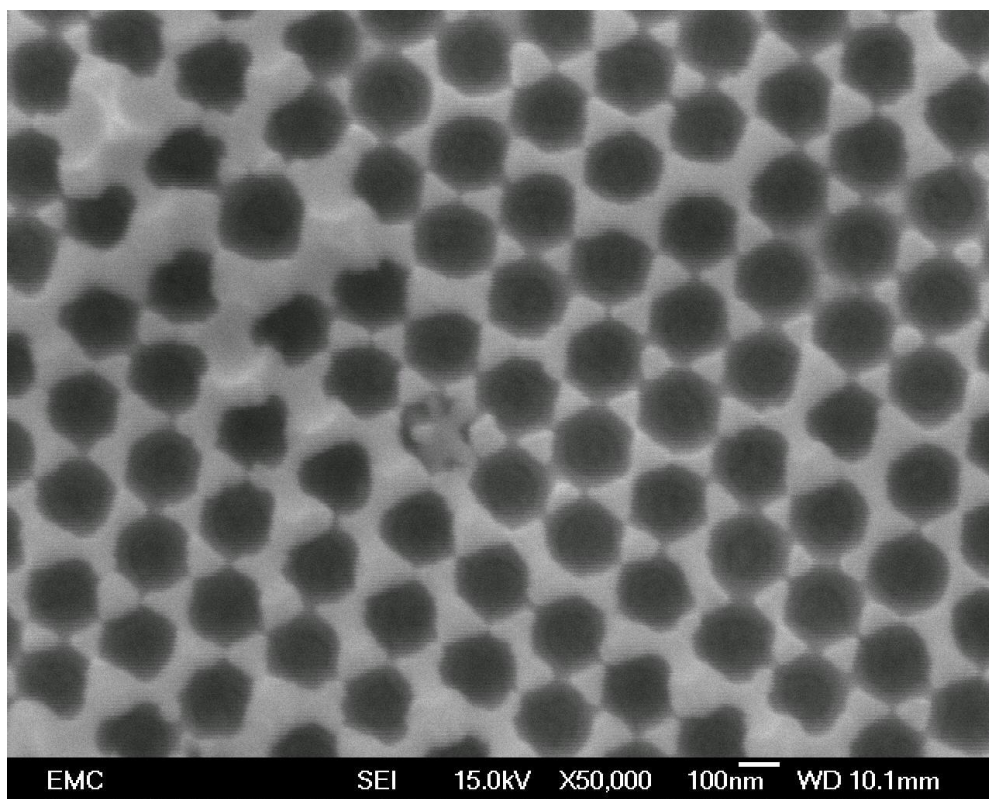


Figure 48 SEM image showing a single AgNS residing within the 220 nm SSV cavity.

Accelerating voltage 15 kV, 50000x magnification, scale bar 100 nm.

An investigation into the optimal deposition height for 220 nm SSVs with 785 nm excitation has not yet been conducted. An 80% deposition height was used for both 600 nm and 220 nm templates. Optimisation of this parameter may lead to greater amplification of the incident and scattered light, which can be used in applications where lower concentrations and detection limits are required.

5.5 Silver nanostars functionalised with rabbit anti-BSA

With the knowledge that silver nanostars provide a significant level of enhancement to the Raman signal of a target molecule, work was conducted to establish the ability to use AgNS as SERS probes. A generalised SERS probe could be applied to any surface, to enhance the signal obtained. This could also be used to form the reporting part of a sandwich assay, offering additional enhancement method to the signal obtained from a SERS or WERS platform. Most studies in the literature use gold nanoparticles in a variety of geometries.¹¹⁹ Silver nanoparticles have received minimal attention, likely due to their oxidative instability and toxicity of silver nanoparticles within cells.

Stabilisation of silver colloids may be a suitable approach to developing highly enhancing SERS probes. In Sections 5.5.1 and 5.5.2, AgNS are functionalised with two Raman reporter molecules and the AgNS are activated for the conjugation of rabbit anti-BSA IgG antibody. The spectra were recorded from a droplet of the AgNS deposited on a glass slide.

5.5.1 Thiobenzonitrile functionalisation

Thiobenzonitrile (TBN) was selected as a candidate for functionalising AgNS for use as a Raman reporter. This is a heterobifunctional molecule with an affinity to silver through the -SH functional group, and a polarizable $\text{-C}\equiv\text{N}$ group to provide a signal within the biological silent region of the Raman spectrum. A mixed monolayer of TBN with mercaptohexadecanoic acid (MHDA) was used to provide sites to immobilise the antibody through EDC/NHS coupling.

Successful TBN-MHDA monolayer formation was confirmed using SERS. While no clear peaks were observed originating from MHDA, the characteristic spectrum of TBN can be observed with a peak at 2250 cm^{-1} from the $\text{C}\equiv\text{N}$ group, and the aromatic peaks at 1078 cm^{-1} and 1600 cm^{-1} also visible. A UV-visible spectrum was also obtained, which had a maximum at 401 nm – shifted from the spectrum of unfunctionalised AgNS. This suggests aggregation of the nanostars, or the formation of spherical nanoparticles. The volume required to fill the cuvette for this measurement required significant dilution of the AgNS, hence the spectrum is weak.

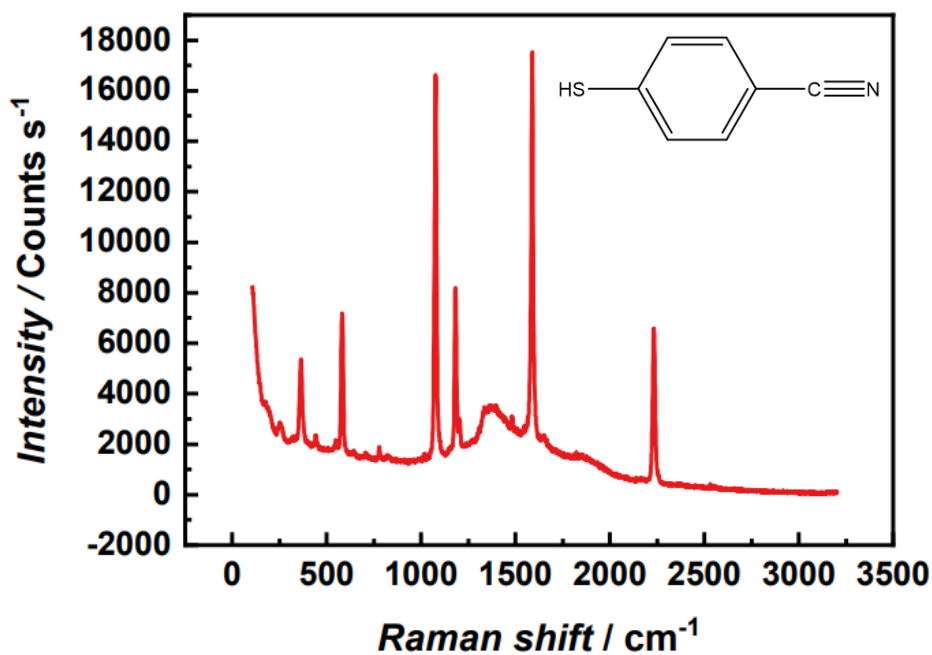


Figure 49 SERS spectrum of AgNS functionalised with a mixed monolayer of TBN and MHDA. Collection parameters: 785 nm, 0.05 mW, 10 s.

The EDC/NHS-activated AgNS were incubated with the antibody and the UV-vis spectrum is presented in Figure 51. With a very low yield, the sample was extremely dilute, leading to a poor-quality spectrum. However, the presence of protein is indicated by the intensity at and below 290 nm which is indicative of the presence of amino acids within the dispersion. The peak near 400 nm is broad, and shows the characteristic tail towards 600 nm, which is attributed to plasmonically active silver nanoparticles.

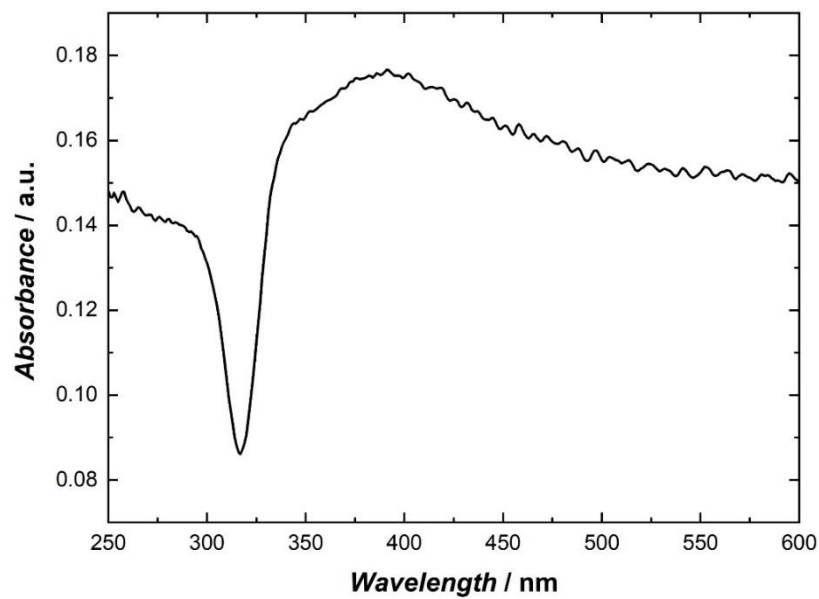


Figure 50 UV-vis spectrum showing silver nanostars functionalised with a mixed monolayer of TBN and MHDA. $\lambda_{\text{max}} = 400$ nm.

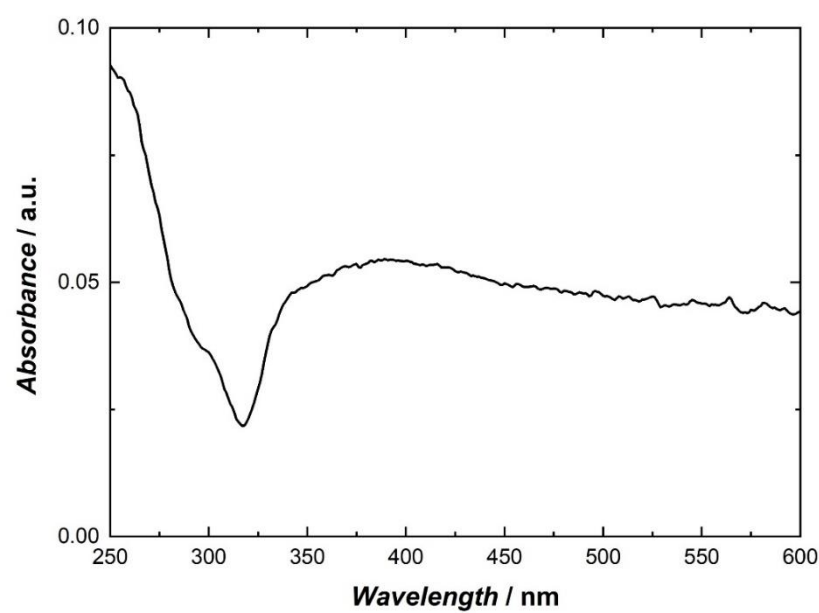


Figure 51 UV-vis spectrum showing silver nanostars functionalised with a mixed monolayer of TBN and MHDA, followed by binding of IgG antibody.

TEM images of the AgNS were collected. The TBN-MHDA functionalised nanostars showed areas of aggregates and disperse nanostars. After introduction of the antibody, more clusters were observed. However, the geometrical structure of the AgNS remained intact.

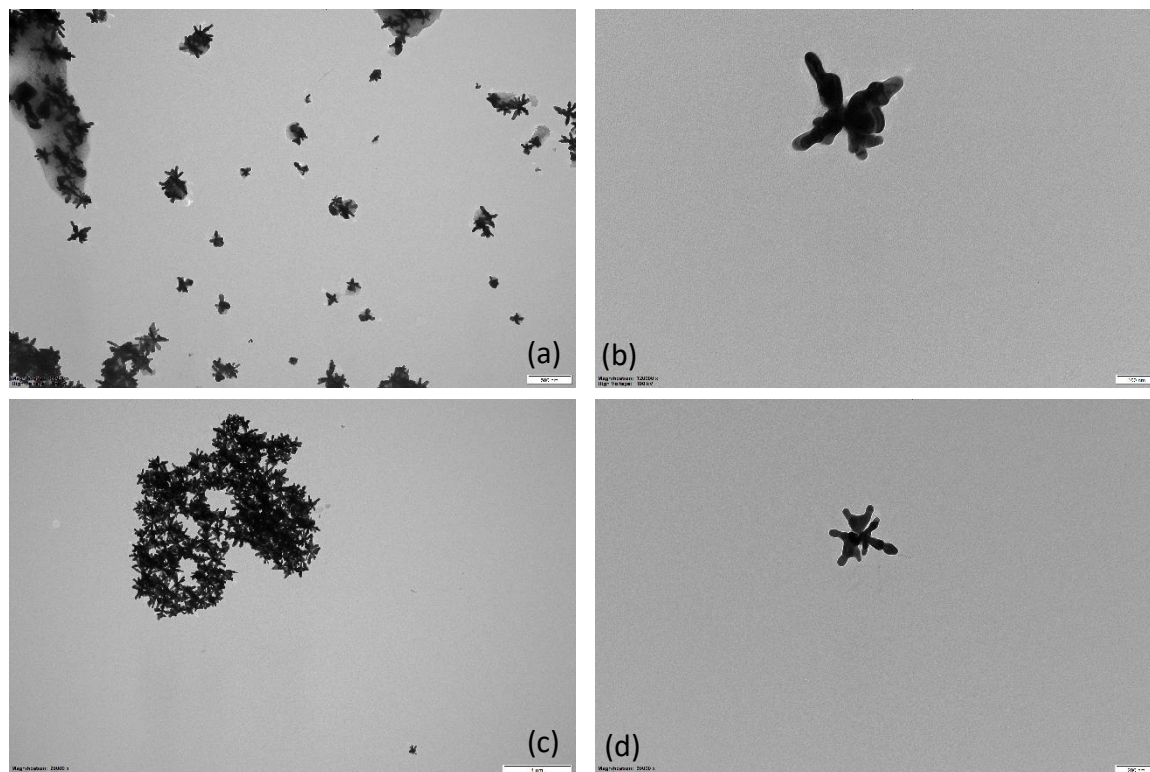


Figure 52 TEM micrographs of AgNS functionalised with TBN-MHDA (a, b) and TBN-MHDA + Ab (c, d). (a) accelerating voltage 100 kV, magnification 20000x, scale bar 500 nm; (b) 100 kV, 120000x, scale bar 100 nm; (c) 100 kV, 20000x, scale bar 1 μ m; (d) 100 kV, 20000x, scale bar 200 nm.

5.5.2 DTNB functionalisation

5,5'-dithiobis-(2-nitrobenzoic acid) (DTNB) has been used as a Raman reporter for gold SERS probes.^{120,121} While existing as a dimer, the disulfide group dissociates to form a triply substituted benzene ring, anchoring to the metallic surface through the thiol. An -NO₂ group provides a strong and easily distinguishable Raman signal for the SERS probe. Finally, the carboxylic acid group enables additional functionalisation and immobilisation of the antibody.

The SERS spectrum was of good quality and showed a very strong band at ~ 1330 cm⁻¹ from the symmetric NO₂ stretch, and the UV-visible spectrum showed a shift to 401 nm

which is typical of spherical silver nanoparticles and aggregates. TEM images showed a loss of the AgNS shape and aggregation of the more rounded nanoparticles. This aggregation may have generated hot-spots leading to the high level of enhancement observed with SERS.

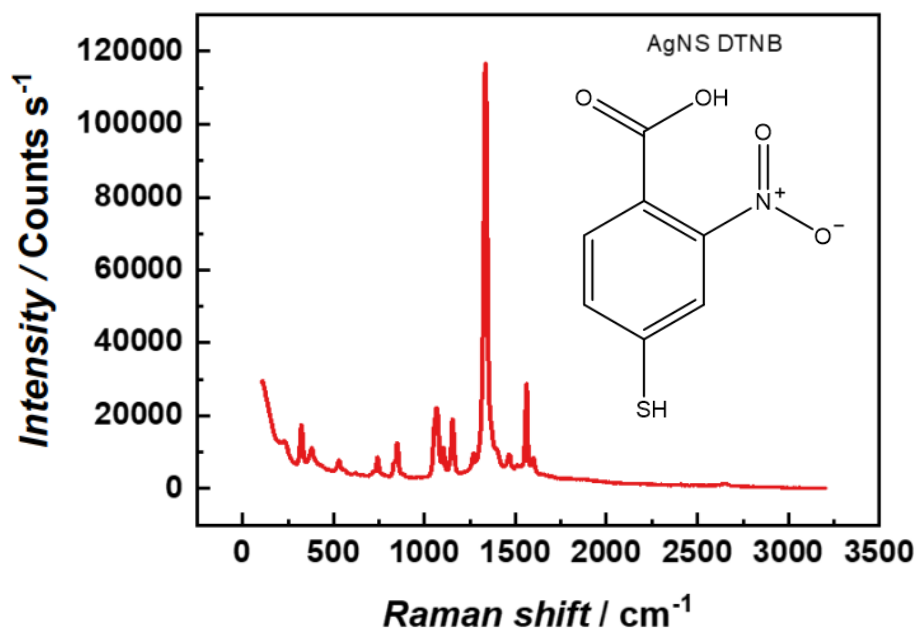


Figure 53 The SERS spectrum of AgNS functionalised with DTNB. Collection parameters: 785 nm excitation, 10 s integration, 0.05 mW.

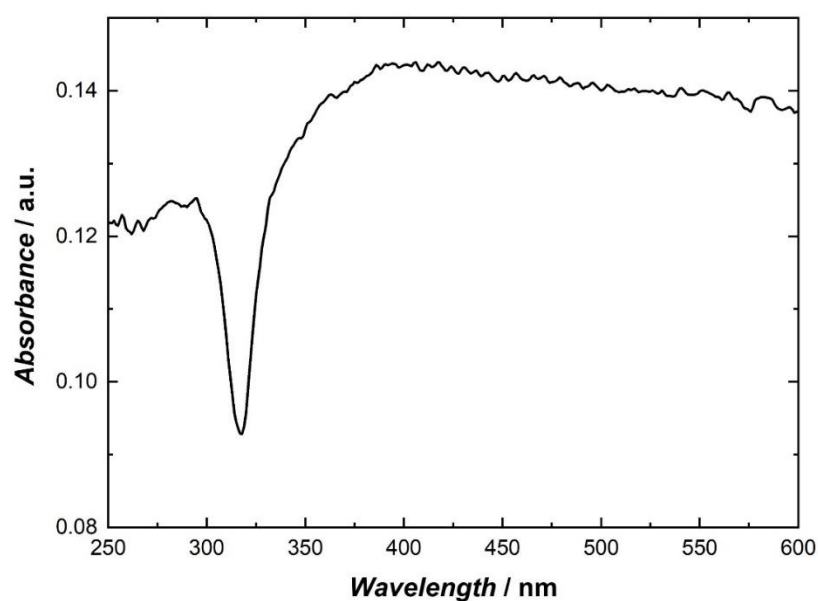


Figure 54 UV-visible spectrum of DTNB functionalised AgNS.

Chapter 5

DTNB AgNS that had been incubated with the antibody were also highly aggregated and amorphous. The UV-vis spectrum showed a level of absorbance below 300 nm, and a maximum at approximately 400 nm which may indicate the presence of protein and nanoparticles. As the sample was highly diluted, it is not possible to determine with confidence whether any antibody was present on the surface of the AgNS.

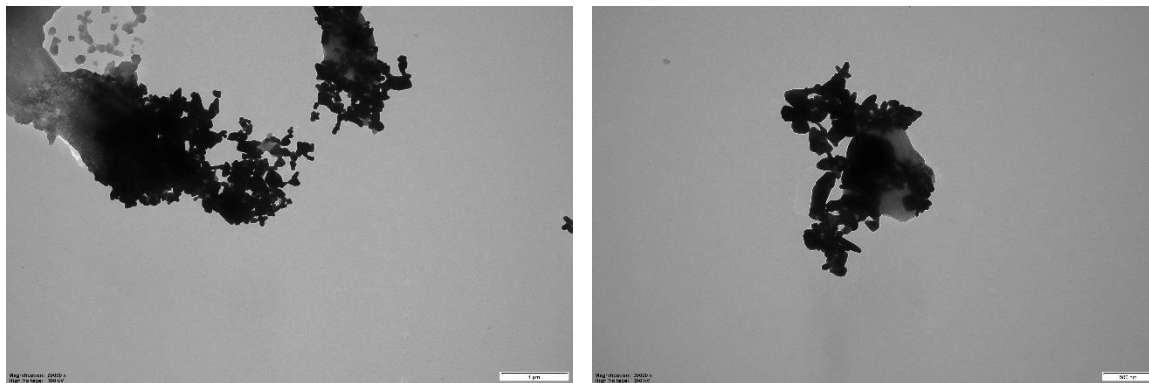


Figure 55 TEM images showing DTNB functionalised AgNS

5.5.3 Summary of AgNS biofunctionalization strategies

Functionalisation of AgNS with Ab is currently in a very early stage of development and the data currently obtained is insufficient to confidently state the possibility of application within a biosensor. Without further stabilisation, DTNB may be ruled out as a potential Raman reporter, as the loss of shape and aggregation of the AgNS limits the reproducibility and longer-term stability of the colloid. The Raman signal produced from DTNB functionalised AgNS is sufficiently high that there is interest in further development, and this may be achievable through changing buffers, adding BSA or other blockers to the buffer solution, or through adding additional steps such as PEGylation.^{122,123} Addition of hydrophilic groups such as heterobifunctional oligoethyleneglycol- containing groups may stabilise the nanostars against aggregation. PEGylated nanoparticles have been used in the literature and have found commercial use in reducing non-specific interactions of proteins in the sample media.

The SERS signal originating from the TBN-MHDA AgNS was not as strong as observed with DTNB, but the presence of the characteristic $C\equiv N$ band in the biological silent region means that it may be readily identified, even in the presence of a complex mixture, where identification in the fingerprint region may be obscured through Raman bands or

autofluorescence. The nanostar shape was retained, and the MHDA carboxylic acid group allows flexibility for further modification.

A fully stabilised, and strongly enhanced SERS probe may find use in sandwich assays. Currently, this area is dominated by Au nanoparticles, employing Raman reporters or dyes such as Rhodamine 6G or MGITC. Finding a methodology for functionalising silver nanostars with a variety of reporter molecules may enable highly sensitive, multiplex detection.

5.6 Introduction to paper fluidics

A key characteristic in a low-burden biosensor is the ability to use small sample volumes, using readily available and disposable materials. This section will look at the potential for paper to be used in this way to assist the detection of a target molecule using SERS.

Paper fluidics provide an inexpensive and disposable method for enabling detection of analytes, whether the detection occurs within the paper^{124–127} or if the paper is used as a delivery system to a sensor platform. Paper is made up of cellulose fibres and is porous, so liquids are able to wick through the paper by capillary action, and typically only microlitre volumes of analyte are required. Early work into the field used SU-8 photoresist or PDMS to create highly resolved channels within the paper; however, the material and experimental costs may limit widespread use of the technique. Whitesides¹²⁸ and Lu¹²⁹ both demonstrated the use of a solid ink printer to print hydrophobic boundaries in Whatman chromatography paper. The estimated material cost of these devices was USD \$0.001 cm⁻² for the chromatography paper, and USD \$0.0001 cm⁻² for the solid ink, alongside one-time costs of purchasing the wax printer and the ink.¹²⁸ A benefit of this method includes the rapid fabrication, as multiple devices may be printed on a single sheet of paper and then the sheets are briefly placed in an oven to allow the wax to penetrate the paper. It can take less than 1 minute to produce a sheet of multiple devices, so low-cost devices capable of multiplexing analysis may be produced on a mass-scale taking up little space and using few resources.

Paper fluidic biosensing devices usually take the form of a colorimetric assay. Glucose can be detected by spotting potassium iodide and HRP/glucose oxidase in a well of the device. The protein BSA can be detected by spotting citrate buffer in a separate well and adding

Chapter 5

an ethanolic solution of tetrabromophenol blue. Whitesides *et al.* showed the colorimetric detection of 2.5 mM glucose and 0.38 μM BSA in an artificial urine sample, which is comparable to the sensitivity of commercial dipstick tests.¹³⁰ The colour change can be seen visually, or through processing the intensity of the image with graphics software.

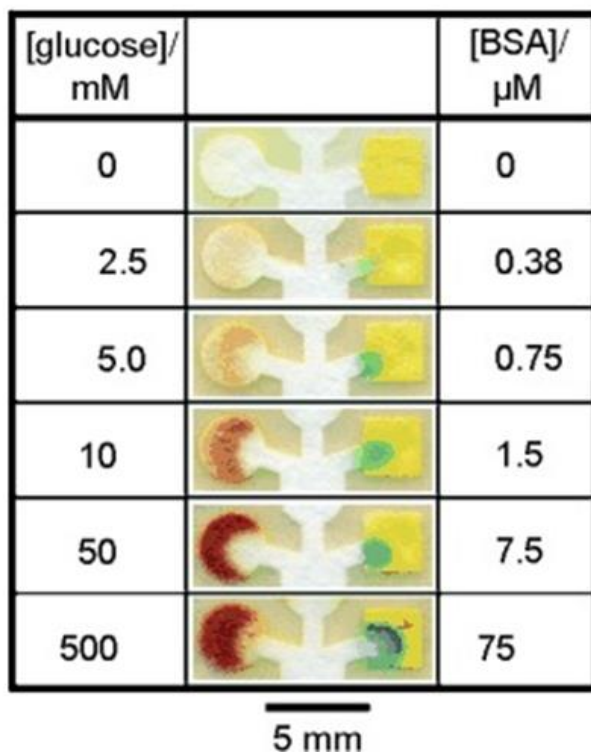


Figure 56 Paper microfluidic detection of glucose and BSA. The boundaries have been defined by a photoresist, but the same effect is observed when the boundaries are wax.[130]

More recently, 3D paper analytical devices have been produced which allow the incubation of an analyte with a reactant and minimise evaporation losses.^{126,131} Figure 57 shows an example of a 3D analytical device used to conjugate biomarkers associated with cardiovascular disease (miR-29a-3p) to Raman reporter-labelled gold nanoparticles.¹³¹

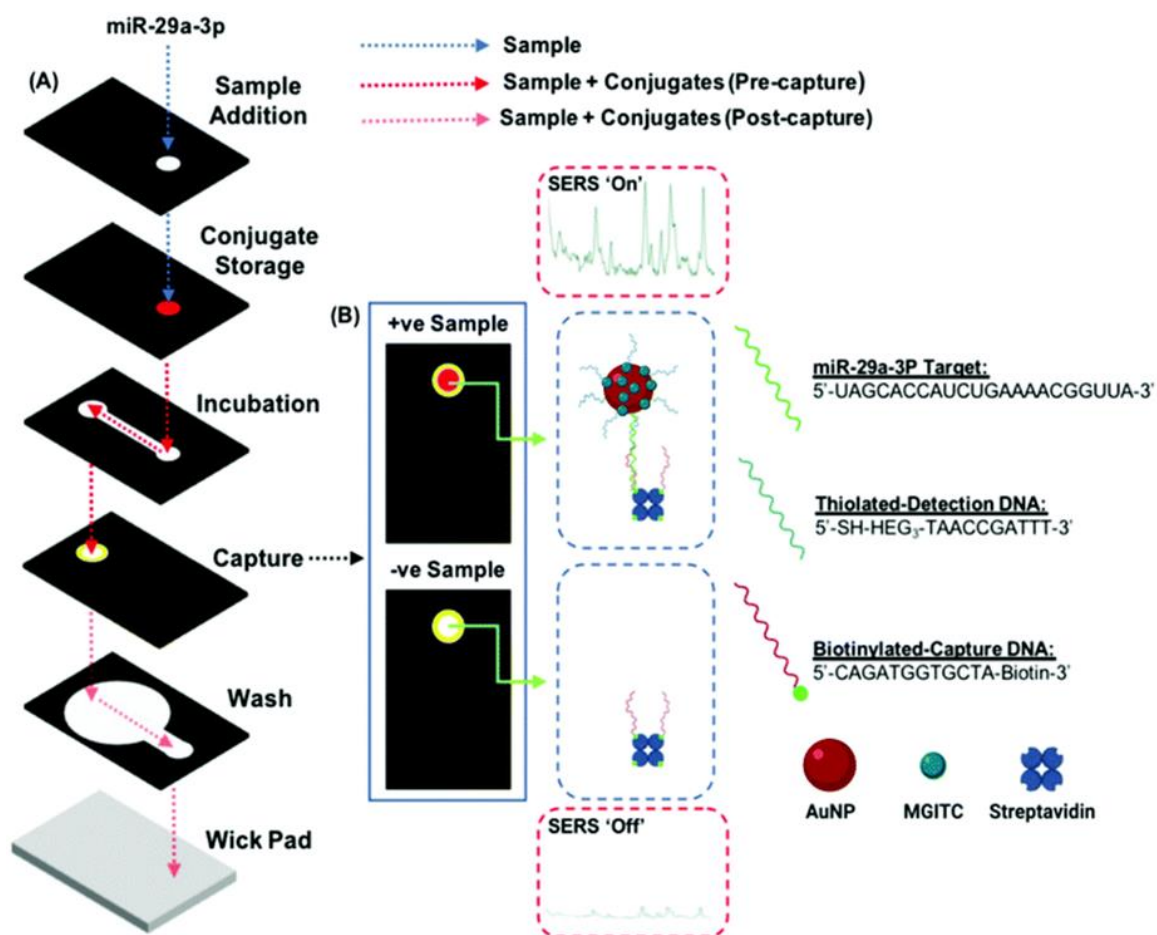


Figure 57 A 3D paper fluidic device allowing the incubation of cardiac marker miR-29a-3p with SERS active nanoparticles. [131]

5.6.1 Glucose detection as proof of concept

A SERS based detection platform was developed for the monitoring of glucose in PBS as a proof of concept, showing that the paper-based fluidics can be used in a biological setting to deliver analytes to a sensor. Boronic acids are known to react selectively and reversibly with 1,2- and 1,3-*cis* diols, as is the case with glucose, fructose and other sugars to form 5- or 6-membered rings.¹³² Some cell walls and antibody side chains can also contain sugar to react with boronic acids.¹³³ Arylboronic acids can also be selectively oxidised under mild conditions by H_2O_2 to cleave the Ar-B(OH)_2 bond resulting in B(OH)_3 and Ar-OH .¹³² The following discussion will focus on 4-mercaptoboronic acid (4-MPBA) because it is highly polarizable, compatible with SERS substrates and contains the boronic functional group for detection.

Direct SERS detection using boronic acids has proved an extremely powerful method of identifying diols, including those on the surface of some cancer cells. However, the main issue of using this as a detection method is that the binding is not selective to glucose – and the affinity is considerably stronger for fructose. Yang *et al.* describe the concentration dependent red shift in the Raman bands resulting from the constraining of the Raman mode upon glucose binding.¹³⁴ They note the benefit of detecting shifts as opposed to intensity monitoring where the intensity is highly dependent on the substrate and can be difficult to reproduce from spot to spot. The competitive binding of fructose (which has a higher association constant at physiological pH) was mentioned, and the naturally lower bodily concentration of fructose was considered to have a negligible contribution to the SERS shift. This shift can also be seen in other benzenethiol derivatives when its functional group bonds to peptides or DNA.¹³⁵ Sun *et al.* describe the changes of the 8a and 8b benzene bands which occur as the symmetry of 4-MBPA is lost upon sugar binding to change the symmetry from pseudo C_{2v} to C_s which results from Herzberg-Teller contributions.^{135,136} They also demonstrated the binding of sugars to 3-MPBA showed no change in Raman signal suggesting that the symmetry element is critical. The methods described offer a one-step detection of glucose, meaning the analyte liquid has to just be added to the sensor to produce the reading, while simplicity is beneficial, neither are selective for glucose, and the identification of the change is dependent on the resolution abilities of the spectrometer.

Kong *et al.* demonstrate a method comparable to a sandwich assay, whereby a mixture of sugar molecules are allowed to bind freely to the 4-MPBA SAM.¹³⁷ After binding, fructose and other sugars are rendered further inactive due to having no available cis-diol groups for further reactivity. Only glucose is still active and reacts with 4-(dihydroxyborophenyl)acetylene added during a second step. The acetylene group is capable of producing a strong Raman signal in the biologically silent region and is easy to distinguish. By measuring the intensity of this band to a stable band, one can calculate the glucose concentration.

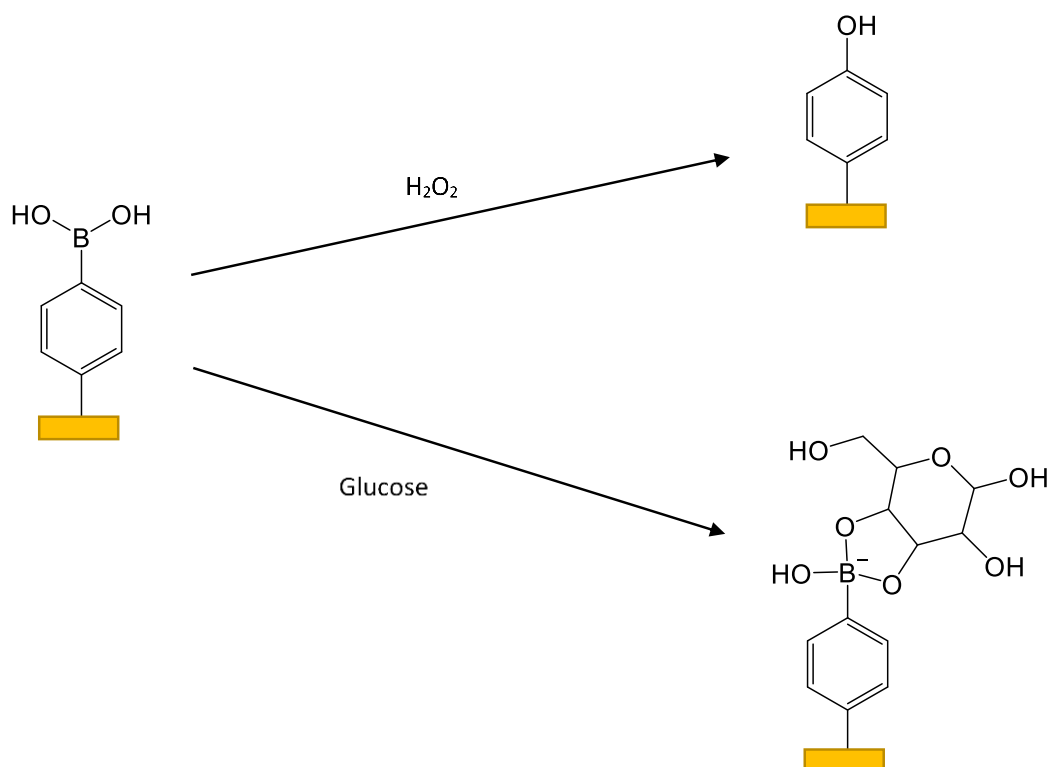


Figure 58 Glucose detection methods using 4-MPBA attached to gold SSV surface. The indirect detection method uses H_2O_2 to cleave the C-B(OH)_2 bond to give 4-MP. The direct method forms a complex with glucose and the boronic acid.

An indirect approach to glucose detection is by the selective conversion of glucose to gluconic acid and hydrogen peroxide in the presence of glucose oxidase (GOx). Wallace *et al.* showed that SAMs of 4-mercaptophenylboronic acid (4-MPBA) could be converted to 4-mercaptophenol (4-MP) after overnight exposure to a 30% H_2O_2 and showed the distinct changes in the SERS spectra associated with this change.¹³⁸ The H_2O_2 concentration used in this demonstration was much higher than the concentration that would be produced by the enzyme, but the authors proposed that this approach could be used in glucose sensors.¹³⁸ This method is useful because it overcomes the limitations associated with the direct detection of glucose, gluconic acid and H_2O_2 where these have only a small Raman cross-section. Instead, the Raman reporter is a simple aromatic molecule with a large cross-section, a head-group that allows it to be anchored to the SERS platform, and the boronic acid functional group that is stable in acidic and physiological conditions but can be selectively cleaved by H_2O_2 .¹³⁹ This change can be monitored using SERS. There are currently no reports employing this strategy for indirect

Chapter 5

glucose detection with 4-MPBA, although colloidal nanoparticle systems have been used to detect H_2O_2 concentrations *in vitro* using 4-carboxyphenylboronic acid¹³² and 3-mercaptophenylboronic acid.¹³⁹ In addition, there have been no reports of using paper to deliver glucose or H_2O_2 to the SERS substrate presenting the arylboronate moiety.

To test the hypothesis, 4-MPBA SAMs were formed on SSV substrates from a 10 mM solution in ethanol. 4-MP SAMs were produced in the same manner to provide a standard for the complete conversion of 4-MPBA to the final product. The template in Figure 59 was printed onto Whatman No. 1 chromatography paper using wax ink. The ink was then melted at 110°C in an oven to form a hydrophobic boundary through the thickness of the paper. Glucose oxidase was spotted into the incubation zone and left to dry.

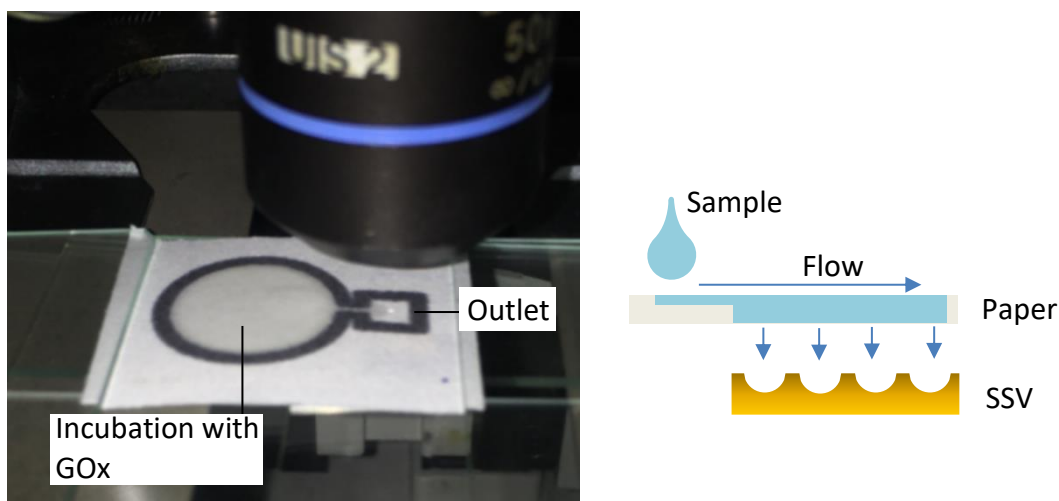


Figure 59 The wax printed design used for the glucose detection experiment. Glucose oxidase was spotted into the incubation zone. The outlet zone was pressed against the 4-MPBA decorated SSV substrate, allowing transfer of the reactants from the paper to the SERS platform. This photograph depicts the set-up for *in-situ* Raman monitoring. A hole was made in the paper, and the laser focussed on the SSV substrate.

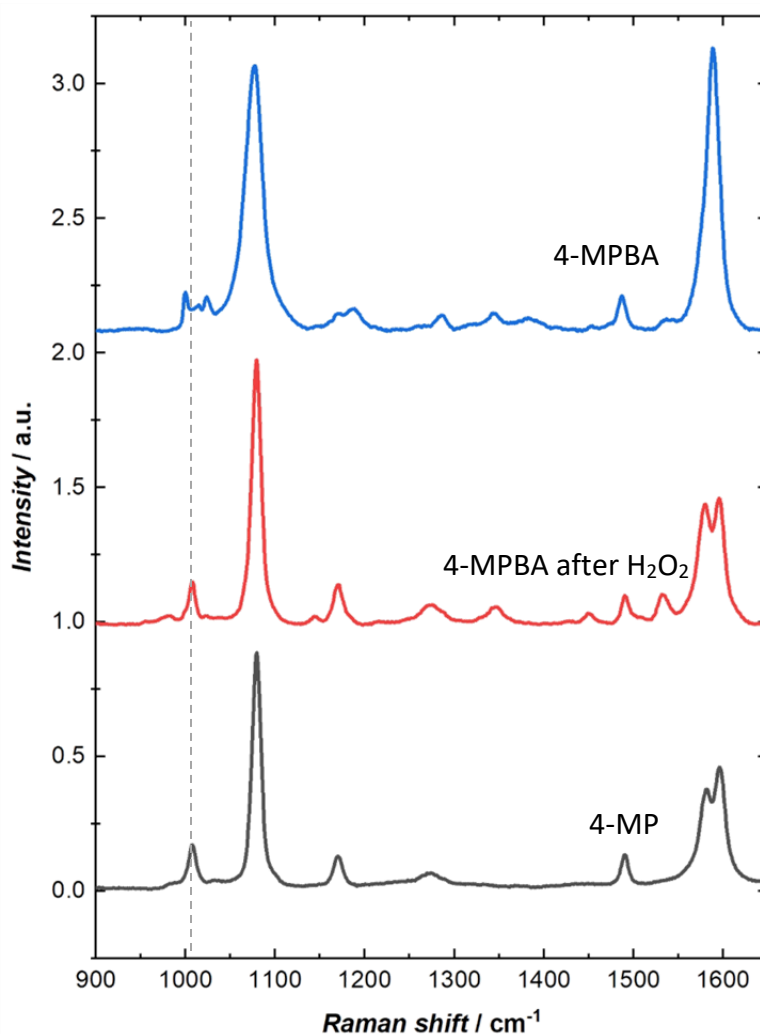


Figure 60 SERS spectra on SSV substrate showing the conversion of MPBA monolayer to MP in the presence of hydrogen peroxide. Top shows the averaged spectrum of 4-MPBA, middle shows the averaged spectrum of 4-MPBA after H₂O₂ exposure, and bottom shows the spectrum of a pure 4-MP monolayer

Figure 60 shows the spectra for the 4-MPBA monolayer (top), the 4-MP monolayer (bottom) and the spectrum resulting from the reaction of 4-MPBA with H₂O₂ produced by glucose oxidase as it metabolises glucose (middle). These represent an average of between 5-10 measurements. The middle spectrum has the characteristics of 4-MP, representing the formation of the phenol from the boronic acid. The C=C stretching bands at $\sim 1600\text{ cm}^{-1}$ have not been chosen as an identifier for the formation of 4-MP. Although 4-MP does have two distinct bands at 1596 cm^{-1} and 1582 cm^{-1} , 4-MPBA may also demonstrate these bands with a change in orientation or upon complexation with glucose.^{134,140} The SERS spectrum of the 4-MPBA-glucose complex is shown in Figure 61. For this measurement, 10 mM glucose was passed through the wax-printed paper in the

absence of glucose oxidase. The two C=C bands are clearly observed in addition to the ring breathing and CH bending modes at 999 cm^{-1} and 1024 cm^{-1} , respectively. This demonstrates that it is specifically the enzyme product, H_2O_2 , that is causing the 4-MPBA to 4-MP conversion, and not a result of the interaction between glucose and 4-MPBA.

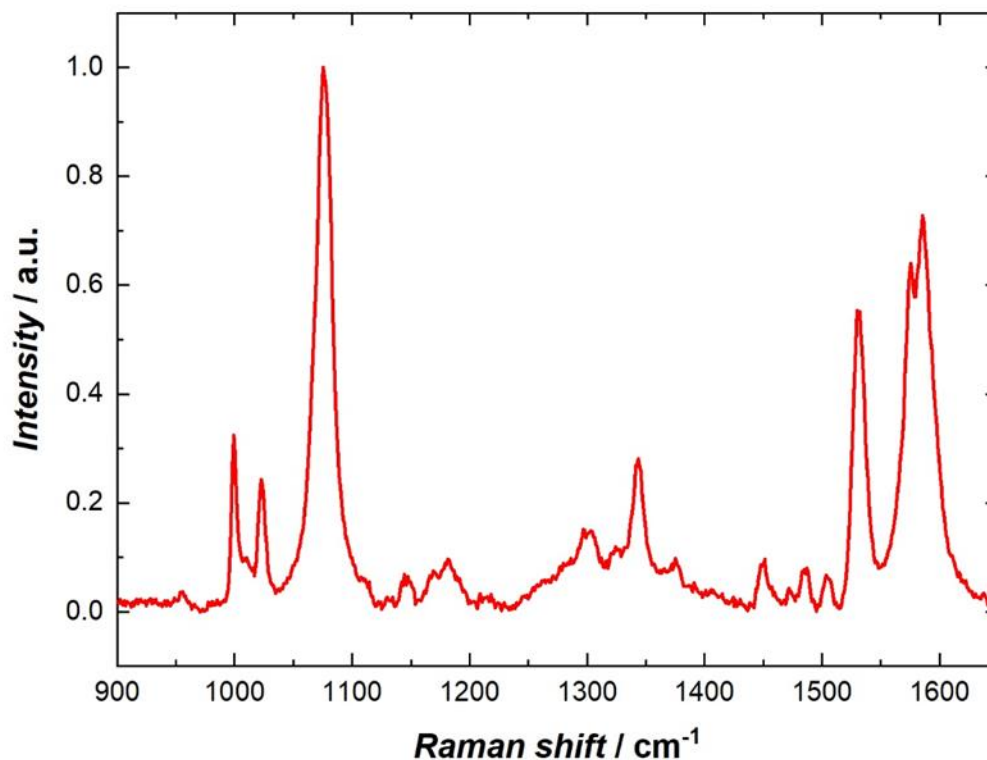


Figure 61 SERS spectrum of 4-MPBA monolayer on SSV substrate after being exposed to glucose in the absence of glucose oxidase.

The characteristic spectral change for the formation of 4-MP is the emergence of the band at 1008 cm^{-1} . This represents the in-plane CH bending mode.¹⁴¹ This is shifted from the equivalent mode in 4-MPBA at 1024 cm^{-1} as the substituent changes from $-\text{B}(\text{OH})_2$ to $-\text{OH}$. The out-of-phase breathing mode is sensitive to the mass of the substituent so the band at 999 cm^{-1} is lost, and likely appears at a much lower frequency as the $-\text{OH}$ group is substituted. The bands associated with the boron substituent are weak in the 4-MPBA spectrum. These appear at 1190 cm^{-1} and 1286 cm^{-1} . These are replaced by bands at 1170 cm^{-1} and 1272 cm^{-1} as the phenol is formed.

Using the intensity ratio of the 1008 cm^{-1} band to that of the ring breathing mode at 1079 cm^{-1} gives 0.16 for 4-MP and 0.09 for 4-MPBA + H_2O_2 . This could be used to determine the concentration of glucose in solution, provided that a suitable calibration curve and

experimental parameters were set. This has been demonstrated for the reaction of 3-MPBA to 3-MP on AuNPs.¹³⁹ Gu *et al.* used the ratio of the 882 cm^{-1} to the 995 cm^{-1} band to calculate the concentration of H_2O_2 , and indirectly the concentration of glucose in solution down to 0.5 mM (Figure 62).¹³⁹ By adopting the hole in the paper method mentioned previously, it should be possible to monitor the reaction *in situ* by using the aforementioned ratio.

Whilst glucose detection can be achieved very effectively by other analytical methods, this section demonstrates the ability for paper fluidics to be used as a tool for point of use analysis. In this example, glucose oxidase was pre-spotted into the paper and could be stored before use. Initial experiments were conducted with chemically immobilised GOx, but no difference was observed. For other applications, SERS probes, DNA strands or antibodies could be loaded in the paper ready for use without additional input from the user. In addition, only a small sample volume was required and was directed to the reactive part of the substrate with ease. These benefits, with the cost-effectiveness of this method make wax-printed paper fluidics a viable choice for using in combination with SERS or WERS for sensitive, low-cost diagnostics.

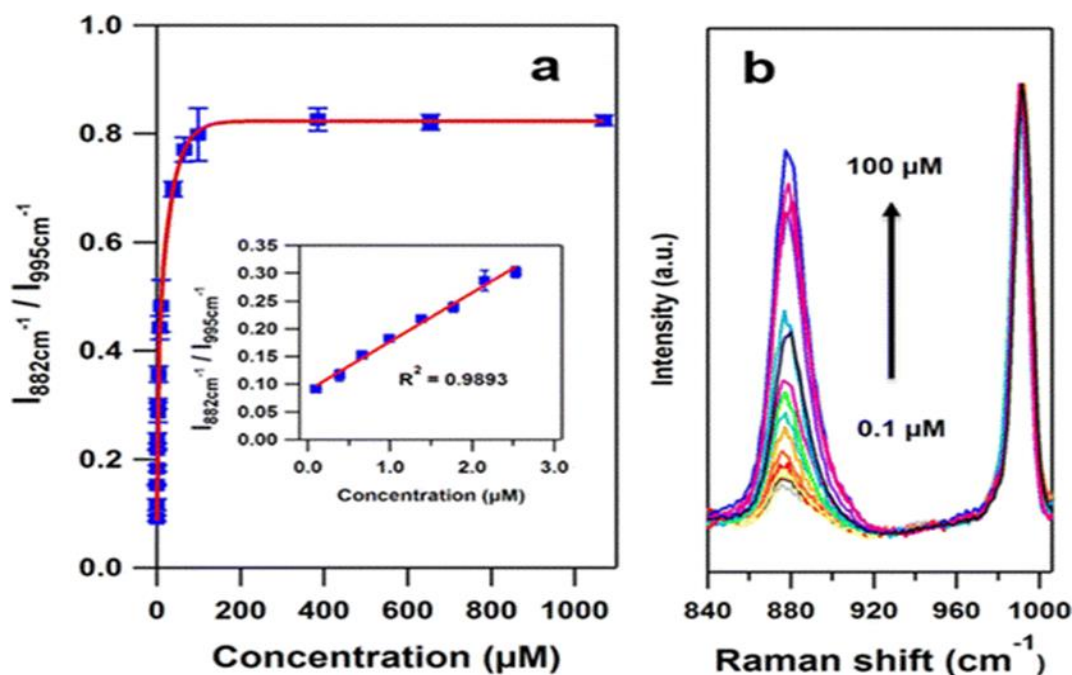


Figure 62 The SERS response to H_2O_2 concentration using 3-MPBA coated AuNPs in PBS.

[139] Left plots the ratio of the bands at 882 cm^{-1} and 995 cm^{-1} corresponding to the ring stretching and C-C bending modes, respectively. The 882 cm^{-1} band is specific to the product of the reaction, 3-MP. Right shows the average SERS spectra for increasing concentrations in the range $0.1\text{--}100\text{ }\mu\text{M}$.

5.7 Summary

SSV and AgNS were shown to be suitable SERS substrates for the analysis of monolayer spectra. The enhancement factors for benzenethiol were calculated to be within the $10^5\text{--}10^7$ region expected of SERS substrates. SSVs with a diameter of 600 nm and 220 nm were compared, with little observable difference in the enhancement factor under the chosen parameters. The use of monolayers with different functional groups had an effect on the SERS behaviour observed with the different substrates, likely due to the influence on the surface charge from the NO_2 and NH_2 substituents on the AgNS. The assumption here has been that the monolayers remain bound to the gold substrate and are not transferred.

Silver nanostars were treated with thiols to create a SERS probe with immobilised antibodies with the aim of enhancing the Raman signals when used in an assay format. Limited data are present to draw conclusions from, but there is difficulty in forming reproducible biological SERS probes with AgNS, particularly with DTNB. This is due to aggregation of the nanostars. The SERS spectra produced from both TBN and DTNB

functionalised nanostars are strong, but there is limited evidence to suggest the presence of antibody, and hence the ability to be selectively captured in an assay. Further work would involve producing greater quantities of the biofunctionalized AgNS and applying these to a SERS or WERS immunoassay.

Paper fluidics was introduced as a method of introducing small volumes of a dissolved analyte to a SERS substrate. As part of this, the analyte underwent a chemical transformation whilst incubated within the paper before reacting with the SERS substrate. This was to highlight the possibility of removing pre-treatment intervention from a hypothetical end-user, minimising training requirements and sources of human error. In this work, a glucose solution was passed through the paper, incubated with glucose oxidase, and then the enzyme product H_2O_2 was passed to a 4-MPBA functionalised SSV substrate. 4-MPBA reacts selectively with H_2O_2 to form 4-MP, and this provided a measurable change in the SERS spectra. It was noted that a system of this type could be used analogously with WERS to monitor spectral changes *in-situ*, as the paper would not interfere with the path of the laser nor reside within the evanescent field. With the SERS system, the paper and SSV were incubated together before removing the paper and collecting the spectrum. Attempts made to monitor the reaction progress in real-time by firing the laser through a hole in the paper were unsuccessful, as the introduction of liquid disrupted its focus.

Chapter 6 Conclusions and further work

6.1 Research summary and conclusions

In this work, approaches have been taken to understand how Raman spectroscopy and its enhanced variants may be used in low-burden diagnostic platforms. As part of an interdisciplinary collaboration, a prototype waveguide enhanced Raman spectrometer was produced, employing planar Ta₂O₅ waveguides and 785 nm excitation. Due to the infancy of the technique and the spectrometer, each results chapter explores a complementary research area, which is then used to guide the development of WERS.

The potential for waveguide enhanced Raman spectroscopy to be used in this manner was discussed in the introduction, with design choices tailored towards a simple to manufacture, and simple to use device. The large interaction area and the advantage of extensive reradiation enhancement offer 10⁴ levels of enhancement relative to the Raman signal. Surface enhanced Raman spectroscopy was also discussed, noting that the enhancement factors can routinely reach 10⁶-10⁷, up to single molecule detection limits in extreme cases. The limitations in forming reproducible substrates were highlighted as a research area that would require further work for SERS to be employed in this application area.

In Chapter 3, the functionalisation of Ta₂O₅ by phosphonic acids was achieved. This has significance as the popular alternative method for self-assembly on metal oxides uses alkoxy silanes. The sensitivity of these to the presence of water in the air, solvent, or on the surface increase the difficulty in producing robust and reproducible functionalised substrates. Two methods were investigated in this approach, immersion and tethering by aggregation and growth. Both demonstrated functionalisation of the surface, monitored by contact angle goniometry. Interestingly, the T-BAG method showed promise in forming densely packed self-assembled monolayers of phosphonic acid derivatives in ethanol, representing a safer to use, more polar solvent than THF. Though studies in 'dry' conditions were not carried out, it appears the phosphonic acids are not limited by the presence of water. Successful functionalisation was additionally confirmed using confocal fluorescence microscopy to show that covalently linked dye remains present on the

Chapter 6

surface, while physisorbed dye is removed by rinsing. Initial tests of the WERS device were carried out, which showed that monolayer detection of NPPA could be achieved, although work is required to develop this further to enable characterisation and identification of low concentration analytes with potentially lower scattering cross-sections. This would be a significant advancement in the field, with the first demonstration of monolayer detection on a planar waveguide with 785 nm, which is especially relevant for biological detection. This research allows for the functionalisation of Ta₂O₅ waveguides for future application as robust and adaptable sensors.

In Chapter 4 the Raman cross-section of benzyl alcohol was determined relative to that of cyclohexane, to establish a suitable new calibration standard for Raman spectroscopic methods. Benzyl alcohol was identified as a candidate due to its relative safety and low vapour pressure. In this work, several solvents and analytes of interest were also included as reference points. A 3D printed custom cuvette holder ensured that the measurement conditions for each solvent was identical. To provide a comparison to the experimental data, density functional theory was also used to calculate the Raman cross-sections. The agreement between the two techniques was good. The spectrum and scattering cross-section of benzyl alcohol is similar to that of toluene, a commonly used Raman standard. In the second part of the chapter, *m*-diethynylbenzene, benzyl alcohol, and benzyl d₇ alcohol were spotted on the waveguide, and their WERS spectra collected. Multiple features could be identified for each analyte, although a number of bands were shifted relative to the spectra obtained using the Raman microscope. For *m*-DEB, the shifted bands originated from substituent vibrations. For benzyl alcohol and benzyl d₇ alcohol, a more significant shift is observed. This demonstrates the importance of establishing a standard and calibrating the spectrometer when conducting measurements. For WERS, a Si calibration standard cannot be employed, so it is important to calibrate to a known solvent.

Chapter 5 investigated the effectiveness and potential application to Raman-based biosensors of silver nanostars and sphere segment void substrates. The enhancement factors given by silver nanostars reached 10⁵-10⁷ which is a significant level of enhancement. The overall level of enhancement was dependent on the functional group of the analyte itself, so the substrate and its surface properties must be considered when applying SERS to the detection and identification of target materials. In addition, while

offering significant levels of enhancement, the reproducibility within and between nanostar-in-cavity substrates was poor. It was unclear how many nanostars were present at the surface where the more significant levels of enhancement were observed without the ability to clearly view and aim the laser on the substrate. This issue could potentially be resolved using combined SEM-SERS analysis. A comparison between 600 nm and 220 nm SSVs showed minor differences under the chosen conditions. Initial experiments using silver nanostars as biological SERS probes was inconclusive, but not ruled out as an option. Finally, a paper fluidics approach was used to deliver H_2O_2 to a SERS substrate which appeared to be a successful and simple approach to glucose detection.

While the experimental work in Chapter 5 did not cover the application to WERS, it is feasible to assume that biofunctionalized AgNS can be transferred to the WERS platform, and the paper fluidic concept can also be transferred. Initial experiments showed that paper employed atop the waveguide is not detectable in the current configuration of the device. Whether or not additional enhancement is achievable from the WERS and AgNS system is of interest to future work.

6.2 Further work

This work was heavily impacted by logistical issues presented by Covid-19, including a lack of access to laboratory spaces, the shutdown of mechanics workshops, long lead times on chemicals and optical components, and equipment breakdowns due to lack of access to both maintenance and repairs. As such, the waveguide Raman spectrometer did not reach the expected levels of maturity to conduct a full analysis on. However, further development could enable miniaturisation and increased sensitivity of the device. Aside from the physical improvements to the WERS prototype, there are several chemical and sensor-based developments which could be employed.

6.2.1 Biological recognition and detection

Having established the fundamentals for the functionalisation of Ta_2O_5 , the next steps would involve the immobilisation of biological receptors onto the surface, using WERS to detect the target molecule. There are a range of immobilisation chemistries which can be employed which would be worth investigating, and the effects on surface treatment on the efficacy and stability could be monitored. For antibody immobilisation, direct

absorption *versus* EDC/NHS, maleimide, or copper-free click chemistry approaches would make an ideal start point. Having identified a suitable immobilisation methodology, a study on the limits of detection could be investigated. In addition to testing the limit of detection of analytes in controlled conditions, the function of the sensor should be assessed using simulant biological fluid samples, containing several potential contaminants and chances for non-specific binding. Therefore, work may be required in improving antifouling chemistry at the sensor interface.

In an ideal system, WERS could offer label free detection of the target material, which would provide a true, low-burden Raman sensing platform. Before this level is reached, initial research may be to employ labelled reporters or use functionalised nanoparticles in a sandwich assay format, or use intercalating dyes where DNA is the target. As linkers and labelling molecules are small, they will reside within the evanescent field and experience radiation enhancement from the waveguide in addition to any enhancement brought themselves, where this distance effect presents more of a challenge in SERS based methodologies. These labelled molecules could be delivered through microfluidics or paper fluidics approaches. Potentially less generalisable approaches could be to use reporters that undergo conformational changes in the presence of the target molecule – DNA molecular beacons, quenchbodies, and antibody bridged beacons could find use here, enabling one-step detection.^{142–144}

6.2.2 Phosphonic acid SAM characterisation

From a fundamental perspective, it would be ideal to fully characterise phosphonic acid SAMs on Ta₂O₅ waveguides, involving AFM, ellipsometry, and XPS analysis, alongside polarized WERS. As the adsorption behaviour of phosphonic acid SAMs is not fully understood, it would be of interest to develop the understanding further. A study into the kinetics of the formation of SAMs *in-situ* could be conducted using WERS, if the molecules in the bulk can be distinguished from the adsorbates.

6.2.3 Development of SSV and AgNS substrates

Nanostar-in-cavity approaches may enable maximal signal amplification; however, the current reproducibility is limited, and dependent on the chemical properties of the analytes. Deposition of biofunctionalized AgNS to the waveguide platform may be easier

to control, as the surface roughness is minimal, and the wettability of the surface can be more readily controlled compared to the SSV substrate. These could be delivered through pipetting, microfluidics or paper fluidics approaches. The current limitation to this is forming a stable AgNS SERS probe. Initial experiments with TBN-MHDA mixed monolayers showed promise under the reaction conditions. The success of biofunctionalisation was not confidently demonstrated, so an initial experiment would be to use AgNS functionalised in this manner in a direct or a sandwich assay on the WERS platform. The unique spectral signature from the TBN appears in the silent region of the Raman spectrum and would indicate the presence of the target on the surface. Analysis could be conducted to find detection limits and whether additional enhancement is observed with the combined SERS-WERS configuration. Further research to fully stabilise functionalised AgNS could be conducted, assessing different buffers, concentrations, and temperatures, and whether PEGylation may improve this, with a long-term goal of finding the optimum parameters to functionalise nanostars with different Raman reporter molecules, enabling multiplex detection.

SSV substrates are extremely robust and exhibit strong plasmonic enhancement. In this work, the deposition height for these the 600 nm and 220 nm SSV substrates was around 80% of the diameter of the spherical standards. The level of enhancement offered by SSV substrates is dependent on the diameter of the spheres, the excitation wavelength, the deposition height, and the quality of the substrate. In this work, a 785 nm excitation source was used. This is known to be near optimal for the 600 nm SSV, and high-quality substrates have been demonstrated for these. The 220 nm SSV substrates have not previously been investigated and so the conditions for maximum enhancement are unknown. To make these practically useful, the reproducibility would need to be improved. Assuming that these substrates could be made reproducible, a study would need to be conducted by varying the deposition height and measuring the SER spectrum with 785 nm excitation light. The work by Cui et al. into UV-SERS shows that the optimum deposition height for a 200 nm Pd SSV is 30% for a 325 nm laser.²⁸ Deep UV Raman can be used to detect low concentration analytes with minimal background fluorescence and strong Raman signals, and can be used to measure conformational changes in proteins which can occur on binding target analytes,¹⁴⁵ so there may be benefit in optimising the 220 nm SSV for <300 nm light by a similar process.

6.3 Concluding statement

Many areas related to the development of flexible, point-of-care Raman spectroscopic devices have been discussed. This has included a discussion into the practical design choices of a waveguide enhanced Raman spectrometer, as well as the chemical-based approaches used to maximise the signal collected from low-concentration analytes in terms of immobilisation and signal enhancement methodologies. For biological trace detection, WERS has an advantage over pure SERS-based techniques as the length of the enhanced field is greater, allowing for the adsorption of biorecognition molecules to the surface of the sensor within the evanescent field, while simultaneously experiencing little interference from the bulk. WERS therefore has great potential for use as a highly sensitive, portable detection technology.

Appendix A DFT calculation of polar derivatives

Table 31 Polar derivatives for CNPPA, calculated in Gaussian.

Atoms	Polar Derivatives / B ²					
	xx	xy, yx	yy	xz, zx	yz, zy	zz
a(x)	15.57354	1.140862	-2.7942	-0.1485	0.0213297	1.381885
a(y)	11.42818	0.407662	0.699249	-0.09988	0.1862306	1.471058
a(z)	0.22108	-0.08189	0.134858	-1.42145	2.989078	-0.33537
b(x)	-17.1247	-0.40017	2.261232	-0.03488	-0.0898655	1.644996
b(y)	13.80424	-0.67759	0.230606	0.095952	0.1450024	1.436886
b(z)	-0.31401	0.063908	0.160599	0.627088	3.1363203	-0.15957
c(x)	50.02356	-0.92728	2.331269	0.13413	-0.053644	0.807121
c(y)	-0.94148	0.50989	-0.45812	0.029358	-0.0544945	0.017535
c(z)	0.434483	0.09746	0.0519	4.528151	-0.1288943	0.063148
d(x)	-16.2865	1.406323	2.742458	0.028377	0.050826	1.571796
d(y)	-13.2085	0.033445	0.099753	0.025903	-0.0875978	-1.5269
d(z)	0.25203	0.100057	-0.16165	0.681916	-3.1201065	0.197665
e(x)	13.82275	-2.06386	-3.07389	-0.08612	0.0308756	-1.41087
e(y)	-11.1285	0.924043	-0.08944	0.017955	-0.0626157	-1.26611
e(z)	0.516544	-0.04924	-0.12517	-1.37917	-2.7896256	0.169437
f(x)	-18.581	0.399794	-1.02164	0.361788	0.0561328	-0.68517
f(y)	-0.53772	-1.66346	0.034823	-0.13275	-0.1267634	-0.1325
f(z)	-1.13982	-0.4826	-0.10548	-3.37673	0.2682074	-0.2967
g(x)	-2.55015	1.753963	-2.17066	-0.07505	0.0809093	-0.2644
g(y)	2.004012	-2.46926	6.766332	0.091165	-0.2358577	0.612747
g(z)	-0.248	0.073793	-0.24633	-0.08984	0.4507026	0.08533
h(x)	2.284568	2.524292	3.115773	-0.07729	-0.0795602	0.323645
h(y)	2.226242	3.224224	7.38475	-0.08072	-0.1770105	0.63315
h(z)	-0.08667	-0.04968	-0.14705	0.405005	0.4078464	-0.03624
i(x)	2.238999	-2.45433	3.041627	0.06309	-0.0710345	0.306819
i(y)	-2.17036	3.18025	-7.64682	-0.07256	0.1706718	-0.62569
i(z)	0.017833	-0.09836	0.19201	0.374007	-0.444393	0.041129
j(x)	-2.38403	-2.16362	-2.54431	0.021705	0.0409054	-0.23971
j(y)	-2.21897	-2.76448	-6.97743	0.078315	0.1085255	-0.63185
j(z)	-0.06084	0.008815	0.083122	-0.11709	-0.4441123	0.017135
k(x)	-67.91	1.173757	-2.13677	-0.33775	0.0338654	-1.52515
k(y)	0.940074	-1.48775	0.050228	-0.00141	-0.0188165	0.048628
k(z)	-0.70203	0.000383	-0.05103	-1.63154	0.0421905	-0.09404
l(x)	53.40093	-0.76461	3.204595	0.234163	-0.0124973	3.256029
l(y)	-0.63269	7.044744	-0.2847	-4.1E-05	0.0522016	-0.05655
l(z)	0.425322	-0.00805	0.044358	7.061432	-0.1212277	0.151378
m(x)	11.31799	-2.24294	0.440023	-0.90757	-0.4457155	0.51377
m(y)	-3.12858	2.137322	-3.24976	-0.84367	0.1916234	0.055295
m(z)	-1.47356	-0.65734	0.332845	1.073726	0.9364734	0.111954
n(x)	6.806531	2.221974	1.290887	1.818542	0.8166762	1.600126

Appendix A

n(y)	0.335254	-0.50181	-3.306	0.09525	-2.3332573	-1.72041
n(z)	0.631398	-0.12742	-1.71188	-0.70893	-1.6767086	-4.88096
o(x)	-13.0173	-3.04583	-1.51787	-3.64111	-1.1143392	-2.09456
o(y)	-3.03486	-1.26628	-0.96951	-0.66764	-0.6083947	-0.3658
o(z)	-2.58447	-0.70421	-0.33144	-1.70709	-0.6446961	-1.21957
p(x)	-6.11875	-1.08193	-0.30438	1.246337	0.8948903	0.213293
p(y)	-5.71555	-1.24882	-4.08661	2.674426	1.7576854	-4.65468
p(z)	1.922834	1.9628	0.916064	-0.14843	-3.0085089	0.768474
q(x)	-1.5041	0.024762	-0.39571	1.374853	-0.3014445	-1.5313
q(y)	1.895635	-0.73429	0.921718	-1.453	1.3073085	2.837903
q(z)	2.612864	-0.32721	1.17433	-2.83656	1.0289265	6.125716
r(x)	-9.99226	4.49883	-2.46843	0.025292	0.1416899	-1.10456
r(y)	10.0836	-4.64782	10.88094	0.243357	-0.214441	3.867287
r(z)	-0.42498	0.278781	-0.21006	-1.3345	3.1185279	-0.53826

Table 32 Polar derivatives of NPPA, calculated in Gaussian.

Atoms	Polar Derivatives / B ²					
	xx	xy, yx	yy	xz, zx	yz, zy	zz
a(x)	2.029454	1.144084	2.287629	0.104003	-0.0971656	2.013783
a(y)	7.093714	0.208418	3.440374	-0.10312	-0.0078788	0.899422
a(z)	-0.08143	0.04514	0.026425	2.967955	2.8678008	0.182901
b(x)	-3.37779	-4.73221	-0.83132	-0.06752	-0.0822773	-0.14618
b(y)	0.591591	0.178118	0.571595	-0.0006	-0.0342798	2.329378
b(z)	-0.13126	0.066467	-0.08278	-0.42266	3.746863	-0.00469
c(x)	-1.20845	2.876957	-2.04407	0.084443	0.0011426	-2.28229
c(y)	9.83411	4.272176	2.721168	0.016384	0.1053722	0.160978
c(z)	0.026723	0.021672	-0.02983	-3.05934	2.1101778	0.016015
d(x)	-14.0968	-12.0931	-7.57012	-0.13547	-0.0157712	-0.62321
d(y)	-14.5784	-5.37675	-4.09689	-0.00283	-0.0929369	-0.47827
d(z)	-0.12867	-0.01777	-0.02618	-2.81751	-1.5552306	-0.04072
e(x)	3.043168	10.05503	4.534541	0.217954	-0.0140627	0.039704
e(y)	-3.21785	1.874051	-2.2976	0.002577	-0.0061305	-1.49282
e(z)	0.01215	0.062104	-0.01938	0.943024	-2.1521161	-0.0372
f(x)	6.389955	-4.37174	-0.78621	-0.29627	0.1720752	0.372517
f(y)	-7.3328	-4.95051	-2.75859	0.009721	0.0262152	-0.1492
f(z)	0.460217	-0.55415	0.500269	2.49824	-0.6330556	0.190433
g(x)	5.299654	2.756368	2.893123	0.063822	0.0566281	0.474275
g(y)	2.475819	2.992624	4.116261	0.047331	0.0654371	0.452463
g(z)	0.172168	-0.0198	0.112026	0.143579	0.2759752	0.030552
h(x)	-0.40317	1.651614	-1.15674	0.013777	-0.0080522	-0.08255
h(y)	1.196403	-1.50568	12.31842	-0.01082	0.0632202	0.673929
h(z)	0.007995	0.008978	0.002062	-0.20992	0.5560515	0.004434
i(x)	-7.24816	2.525205	-2.28619	-0.0224	0.0070381	-0.65931
(y)i	2.283972	-2.58603	1.560746	0.001219	-0.0060596	0.302986
i(z)	-0.02142	0.004057	-0.00918	-0.3625	0.1671773	-0.01019

j(x)	-0.3067	-1.29961	0.706844	0.023102	-0.0098738	0.002053
j(y)	-1.69913	0.455698	-6.0582	0.008062	0.0045479	-0.69521
j(z)	0.049191	-0.0226	0.045429	-0.08116	-0.4190289	0.006294
k(x)	21.16876	8.38241	4.351592	0.102443	0.0902121	-1.11198
k(y)	7.283154	9.405652	11.44447	0.033755	0.1207583	-0.77329
k(z)	0.15486	0.04764	0.124698	0.201912	0.2139732	0.003744
l(x)	0.922435	-1.80072	0.572283	0.000168	-0.0036278	0.292029
l(y)	-10.1487	-9.13064	-19.0337	-0.05368	-0.1288857	-0.74011
l(z)	-0.05982	-0.03581	-0.07631	-0.31798	-4.1972763	-0.0487
m(x)	-25.8887	-4.14666	-3.82652	-0.06992	-0.0476833	-0.51556
m(y)	6.769675	-0.63841	2.900767	0.057389	0.0006795	0.440145
m(z)	-0.04438	0.002336	-0.02777	-4.43475	1.0258227	-0.00682
n(x)	-8.40744	0.920195	0.9094	0.363156	-0.5349541	-0.42889
n(y)	-1.96228	-3.0428	-2.34002	-0.82883	0.5253195	0.339852
n(z)	0.569071	-0.77912	0.526392	-0.3385	1.234911	-0.24173
o(x)	-3.96551	2.572579	-4.30967	-0.738	2.0193422	-2.18448
o(y)	2.384957	-1.88388	-0.54989	1.522097	1.2842337	-0.90151
o(z)	-0.26082	0.425122	1.158093	-0.00291	-1.6882464	5.253426
p(x)	7.107262	-4.5291	3.595245	2.50055	-1.7879672	1.841592
p(y)	-4.92602	3.508794	-3.71177	-1.52567	1.6843239	-1.25609
p(z)	1.581791	-1.09441	0.992827	1.279702	-1.173195	1.257531
q(x)	1.726773	-1.83968	-0.62747	-0.08165	0.0983578	-2.04699
q(y)	-4.79114	2.287868	-5.06775	1.689442	-2.8351784	-3.98315
q(z)	0.238744	1.555507	-1.92892	-1.27905	-2.5314513	-0.12813
r(x)	2.025999	-0.285	0.682742	-1.87989	0.04982	2.503481
r(y)	1.187297	0.282746	0.15472	-0.94476	-0.6829896	1.779879
r(z)	-2.48839	0.219663	-1.15972	2.913862	-0.2343403	-6.37859
s(x)	15.18922	2.213374	2.904916	-0.18231	0.106819	2.542001
s(y)	7.555681	3.648556	6.685892	0.082334	0.0857681	3.090622
s(z)	-0.05673	0.06498	-0.12814	2.378014	2.385188	-0.04855

List of References

- (1) Chen, Y.; Liu, J.; Yang, Z.; Wilkinson, J. S.; Zhou, X. Optical Biosensors Based on Refractometric Sensing Schemes: A Review. *Biosensors and Bioelectronics* **2019**, *144*, 111693. <https://doi.org/10.1016/j.bios.2019.111693>.
- (2) Aydin, D.; Barnes, J. A.; Loock, H.-P. In-Fiber Interferometry Sensors for Refractive Index. *Applied Physics Reviews* **2023**, *10* (1), 011307. <https://doi.org/10.1063/5.0105147>.
- (3) Schmitt, K.; Oehse, K.; Sulz, G.; Hoffmann, C. Evanescent Field Sensors Based on Tantalum Pentoxide Waveguides – A Review. *Sensors* **2008**, *8* (2), 711–738. <https://doi.org/10.3390/s8020711>.
- (4) Strianese, M.; Staiano, M.; Ruggiero, G.; Labella, T.; Pellecchia, C.; D’Auria, S. Fluorescence-Based Biosensors. In *Spectroscopic Methods of Analysis: Methods and Protocols*; Bujalowski, W. M., Ed.; Methods in Molecular Biology; Humana Press: Totowa, NJ, 2012; pp 193–216. https://doi.org/10.1007/978-1-61779-806-1_9.
- (5) Benito-Peña, E.; Valdés, M. G.; Glahn-Martínez, B.; Moreno-Bondi, M. C. Fluorescence Based Fiber Optic and Planar Waveguide Biosensors. A Review. *Analytica Chimica Acta* **2016**, *943*, 17–40. <https://doi.org/10.1016/j.aca.2016.08.049>.
- (6) Pilot, R.; Signorini, R.; Durante, C.; Orian, L.; Bhamidipati, M.; Fabris, L. A Review on Surface-Enhanced Raman Scattering. *Biosensors* **2019**, *9* (2), 57. <https://doi.org/10.3390/bios9020057>.
- (7) Fan, M.; Andrade, G. F. S.; Brolo, A. G. A Review on Recent Advances in the Applications of Surface-Enhanced Raman Scattering in Analytical Chemistry. *Analytica Chimica Acta* **2020**, *1097*, 1–29. <https://doi.org/10.1016/j.aca.2019.11.049>.
- (8) Polzius, R.; Schneider, Th.; Biert, F. F.; Bilitewski, U.; Koschinski, W. Optimization of Biosensing Using Grating Couplers: Immobilization on Tantalum Oxide Waveguides. *Biosensors and Bioelectronics* **1996**, *11* (5), 503–514. [https://doi.org/10.1016/0956-5663\(96\)86787-X](https://doi.org/10.1016/0956-5663(96)86787-X).
- (9) Mukundan, H.; Anderson, A. S.; Grace, W. K.; Grace, K. M.; Hartman, N.; Martinez, J. S.; Swanson, B. I. Waveguide-Based Biosensors for Pathogen Detection. *Sensors (Basel)* **2009**, *9* (7), 5783–5809. <https://doi.org/10.3390/s90705783>.
- (10) Martinez, J. S.; Grace, W. K.; Grace, K. M.; Hartman, N.; Swanson, B. I. Pathogen Detection Using Single Mode Planar Optical Waveguides. *J. Mater. Chem.* **2005**, *15* (43), 4639–4647. <https://doi.org/10.1039/B502329G>.
- (11) Love, J. C.; Estroff, L. A.; Kriebel, J. K.; Nuzzo, R. G.; Whitesides, G. M. Self-Assembled Monolayers of Thiolates on Metals as a Form of Nanotechnology. *Chem. Rev.* **2005**, *105* (4), 1103–1170. <https://doi.org/10.1021/cr0300789>.

List of References

- (12) Chen, X.; Jiang, C.; Yu, S. Nanostructured Materials for Applications in Surface-Enhanced Raman Scattering. *CrystEngComm* **2014**, *16* (43), 9959–9973. <https://doi.org/10.1039/C4CE01383B>.
- (13) Lebanov, L.; Paull, B. Smartphone-Based Handheld Raman Spectrometer and Machine Learning for Essential Oil Quality Evaluation. *Anal. Methods* **2021**, *13* (36), 4055–4062. <https://doi.org/10.1039/D1AY00886B>.
- (14) Zeng, F.; Mou, T.; Zhang, C.; Huang, X.; Wang, B.; Ma, X.; Guo, J. Paper-Based SERS Analysis with Smartphones as Raman Spectral Analyzers. *Analyst* **2018**, *144* (1), 137–142. <https://doi.org/10.1039/C8AN01901K>.
- (15) Jehlička, J.; Culka, A. Critical Evaluation of Portable Raman Spectrometers: From Rock Outcrops and Planetary Analogs to Cultural Heritage – A Review. *Analytica Chimica Acta* **2022**, *1209*, 339027. <https://doi.org/10.1016/j.aca.2021.339027>.
- (16) Kneipp, K.; Kneipp, H.; Manoharan, R.; Hanlon, E. B.; Itzkan, I.; Dasari, R. R.; Feld, M. S. Extremely Large Enhancement Factors in Surface-Enhanced Raman Scattering for Molecules on Colloidal Gold Clusters. *Appl. Spectrosc.*, *AS* **1998**, *52* (12), 1493–1497.
- (17) Nie, S.; Emory, S. R. Probing Single Molecules and Single Nanoparticles by Surface-Enhanced Raman Scattering. *Science* **1997**, *275* (5303), 1102–1106. <https://doi.org/10.1126/science.275.5303.1102>.
- (18) Fleischmann, M.; Hendra, P. J.; McQuillan, A. J. Raman Spectra of Pyridine Adsorbed at a Silver Electrode. *Chemical Physics Letters* **1974**, *26* (2), 163–166. [https://doi.org/10.1016/0009-2614\(74\)85388-1](https://doi.org/10.1016/0009-2614(74)85388-1).
- (19) Albrecht, M. G.; Creighton, J. A. Anomalously Intense Raman Spectra of Pyridine at a Silver Electrode. *J. Am. Chem. Soc.* **1977**, *99* (15), 5215–5217. <https://doi.org/10.1021/ja00457a071>.
- (20) Jeanmaire, D. L.; Van Duyne, R. P. Surface Raman Spectroelectrochemistry: Part I. Heterocyclic, Aromatic, and Aliphatic Amines Adsorbed on the Anodized Silver Electrode. *Journal of Electroanalytical Chemistry and Interfacial Electrochemistry* **1977**, *84* (1), 1–20. [https://doi.org/10.1016/S0022-0728\(77\)80224-6](https://doi.org/10.1016/S0022-0728(77)80224-6).
- (21) Garcia-Leis, A.; Garcia-Ramos, J. V.; Sanchez-Cortes, S. Silver Nanostars with High SERS Performance. *J. Phys. Chem. C* **2013**, *117* (15), 7791–7795. <https://doi.org/10.1021/jp401737y>.
- (22) Garcia-Leis, A.; Rivera-Arreba, I.; Sanchez-Cortes, S. Morphological Tuning of Plasmonic Silver Nanostars by Controlling the Nanoparticle Growth Mechanism: Application in the SERS Detection of the Amyloid Marker Congo Red. *Colloids and Surfaces A: Physicochemical and Engineering Aspects* **2017**, *535*, 49–60. <https://doi.org/10.1016/j.colsurfa.2017.09.013>.
- (23) Xie, J.; Zhang, Q.; Lee, J. Y.; Wang, D. I. C. The Synthesis of SERS-Active Gold Nanoflower Tags for In Vivo Applications. *ACS Nano* **2008**, *2* (12), 2473–2480. <https://doi.org/10.1021/nn800442q>.
- (24) Tahir, M. A.; Zhang, X.; Cheng, H.; Xu, D.; Feng, Y.; Sui, G.; Fu, H.; Valev, V. K.; Zhang, L.; Chen, J. Klarite as a Label-Free SERS-Based Assay: A Promising Approach for

- Atmospheric Bioaerosol Detection. *Analyst* **2019**, *145* (1), 277–285.
<https://doi.org/10.1039/C9AN01715A>.
- (25) Abdelsalam, M. E.; Bartlett, P. N.; Baumberg, J. J.; Coyle, S. Preparation of Arrays of Isolated Spherical Cavities by Self-Assembly of Polystyrene Spheres on Self-Assembled Pre-Patterned Macroporous Films. *Advanced Materials* **2004**, *16* (1), 90–93. <https://doi.org/10.1002/adma.200306052>.
- (26) Bartlett, P. N. Electrodeposition of Nanostructured Films Using Self-Organizing Templates. *Electrochem. Soc. Interface* **2004**, *13* (4), 28–33.
<https://doi.org/10.1149/2.F04044IF>.
- (27) Cintra, S.; Abdelsalam, M. E.; Bartlett, P. N.; Baumberg, J. J.; Kelf, T. A.; Sugawara, Y.; Russell, A. E. Sculpted Substrates for SERS. *Faraday Discuss.* **2006**, *132* (0), 191–199.
<https://doi.org/10.1039/B508847J>.
- (28) Cui, L.; Mahajan, S.; Cole, R. M.; Soares, B.; Bartlett, P. N.; Baumberg, J. J.; Hayward, I. P.; Ren, B.; Russell, A. E.; Tian, Z. Q. UV SERS at Well Ordered Pd Sphere Segment Void (SSV) Nanostructures. *Phys. Chem. Chem. Phys.* **2009**, *11* (7), 1023–1026.
<https://doi.org/10.1039/B817803H>.
- (29) Mahajan, S.; Richardson, J.; Brown, T.; Bartlett, P. N. SERS-Melting: A New Method for Discriminating Mutations in DNA Sequences. *J. Am. Chem. Soc.* **2008**, *130* (46), 15589–15601. <https://doi.org/10.1021/ja805517q>.
- (30) Levy, Y.; Imbert, C.; Cipriani, J.; Racine, S.; Dupeyrat, R. Raman Scattering of Thin Films as a Waveguide. *Optics Communications* **1974**, *11* (1), 66–69.
[https://doi.org/10.1016/0030-4018\(74\)90336-8](https://doi.org/10.1016/0030-4018(74)90336-8).
- (31) Rabolt, J. F.; Santo, R.; Swalen, J. D. Raman Measurements on Thin Polymer Films and Organic Monolayers. *Appl Spectrosc* **1980**, *34* (5), 517–521.
<https://doi.org/10.1366/0003702804731249>.
- (32) Rabolt, J. F.; Santo, R.; Swalen, J. D. Raman Spectroscopy of Thin Polymer Films Using Integrated Optical Techniques. *Appl Spectrosc* **1979**, *33* (6), 549–551.
<https://doi.org/10.1366/0003702794925101>.
- (33) Rabolt, J. F.; Schlotter, N. E.; Swalen, J. D.; Santo, R. Comparative Raman Studies of Molecular Interactions at a Dye/Polymer and a Dye/Glass Interface. *Journal of Polymer Science: Polymer Physics Edition* **1983**, *21* (1), 1–9.
<https://doi.org/10.1002/pol.1983.180210101>.
- (34) Schlotter, N. E.; Rabolt, J. F. Measurements of the Optical Anisotropy of Trapped Molecules in Oriented Polymer Films by Waveguide Raman Spectroscopy (WRS). *Appl. Spectrosc., AS* **1984**, *38* (2), 208–211.
- (35) Kanger, J. S.; Otto, C.; Slotboom, M.; Greve, J. Waveguide Raman Spectroscopy of Thin Polymer Layers and Monolayers of Biomolecules Using High Refractive Index Waveguides. *J. Phys. Chem.* **1996**, *100* (8), 3288–3292.
<https://doi.org/10.1021/jp952566t>.

List of References

- (36) Kanger, J. S.; Otto, C. Orientation Effects in Waveguide Resonance Raman Spectroscopy of Monolayers. *Appl Spectrosc* **2003**, *57* (12), 1487–1493. <https://doi.org/10.1366/000370203322640125>.
- (37) Wang, Z. Waveguide Enhanced Raman Spectroscopy (WERS): Principles, Performance, and Applications. phd, University of Southampton, 2016. <https://eprints.soton.ac.uk/409729/> (accessed 2022-09-14).
- (38) Coucheron, D. A.; Wadduwage, D. N.; Murugan, G. S.; So, P. T. C.; Ahluwalia, B. S. Chip-Based Resonance Raman Spectroscopy Using Tantalum Pentoxide Waveguides. *IEEE Photonics Technology Letters* **2019**, *31* (14), 1127–1130. <https://doi.org/10.1109/LPT.2019.2915671>.
- (39) Dhakal, A.; Raza, A.; Peyskens, F.; Subramanian, A. Z.; Clemmen, S.; Thomas, N. L.; Baets, R. Efficiency of Evanescent Excitation and Collection of Spontaneous Raman Scattering near High Index Contrast Channel Waveguides. *Opt. Express, OE* **2015**, *23* (21), 27391–27404. <https://doi.org/10.1364/OE.23.027391>.
- (40) Holmstrom, S. A.; Stievater, T. H.; Kozak, D. A.; Pruessner, M. W.; Tyndall, N.; Rabinovich, W. S.; McGill, R. A.; Khurgin, J. B. Trace Gas Raman Spectroscopy Using Functionalized Waveguides. *Optica, OPTICA* **2016**, *3* (8), 891–896. <https://doi.org/10.1364/OPTICA.3.000891>.
- (41) Wang, P.; Miller, B. L. Waveguide-Enhanced Raman Spectroscopy (WERS): An Emerging Chip-Based Tool for Chemical and Biological Sensing. *Sensors* **2022**, *22* (23), 9058. <https://doi.org/10.3390/s22239058>.
- (42) Ettabib, M. A.; Marti, A.; Liu, Z.; Bowden, B. M.; Zervas, M. N.; Bartlett, P. N.; Wilkinson, J. S. Waveguide Enhanced Raman Spectroscopy for Biosensing: A Review. *ACS Sens.* **2021**, *6* (6), 2025–2045. <https://doi.org/10.1021/acssensors.1c00366>.
- (43) Lee, W.; Muñoz-Galindo, P.; Hegeman, I.; Yong, Y.-S.; Dijkstra, M.; García-Blanco, S. M.; Offerhaus, H. L. Study on Multiple Waveguide Platforms for Waveguide Integrated Raman Spectroscopy. *OSA Continuum* **2020**, *3* (5), 1322. <https://doi.org/10.1364/OSAC.389053>.
- (44) Kita, D. M.; Kita, D. M.; Kita, D. M.; Michon, J.; Michon, J.; Michon, J.; Hu, J. A Packaged, Fiber-Coupled Waveguide-Enhanced Raman Spectroscopic Sensor. *Opt. Express, OE* **2020**, *28* (10), 14963–14972. <https://doi.org/10.1364/OE.392486>.
- (45) Wang, Z.; Zervas, M. N.; Bartlett, P. N.; Wilkinson, J. S. Surface and Waveguide Collection of Raman Emission in Waveguide-Enhanced Raman Spectroscopy. *Opt. Lett.* **2016**, *41* (17), 4146. <https://doi.org/10.1364/OL.41.004146>.
- (46) Raza, A.; Clemmen, S.; Wuytens, P.; Goede, M. de; Tong, A. S. K.; Thomas, N. L.; Liu, C.; Suntivich, J.; Skirtach, A. G.; Garcia-Blanco, S. M.; Blumenthal, D. J.; Wilkinson, J. S.; Baets, R. High Index Contrast Photonic Platforms for On-Chip Raman Spectroscopy. *Opt. Express, OE* **2019**, *27* (16), 23067–23079. <https://doi.org/10.1364/OE.27.023067>.
- (47) Makela, M.; Gordon, P.; Tu, D.; Soliman, C.; Coté, G. L.; Maitland, K.; Lin, P. T. Benzene Derivatives Analysis Using Aluminum Nitride Waveguide Raman Sensors.

- Anal. Chem.* **2020**, *92* (13), 8917–8922.
<https://doi.org/10.1021/acs.analchem.0c00809>.
- (48) Evans, C. C.; Liu, C.; Suntivich, J. TiO₂ Nanophotonic Sensors for Efficient Integrated Evanescent Raman Spectroscopy. *ACS Photonics* **2016**, *3* (9), 1662–1669.
<https://doi.org/10.1021/acsphotonics.6b00314>.
- (49) Dhakal, A.; Wuytens, P. C.; Peyskens, F.; Jans, K.; Thomas, N. L.; Baets, R. Nanophotonic Waveguide Enhanced Raman Spectroscopy of Biological Submonolayers. *ACS Photonics* **2016**, *3* (11), 2141–2149.
<https://doi.org/10.1021/acsphotonics.6b00593>.
- (50) Emmons, E. D.; Wilcox, P. G.; Roese, E. S.; Tripathi, A.; Guicheteau, J. A.; Hung, K. C.; Miller, B. L.; Luta, E. P.; Yates, M. Z.; Tyndall, N. F.; Stievater, T. H. Waveguide-Enhanced Raman Spectroscopy for Field Detection of Threat Materials. In *Integrated Optics: Devices, Materials, and Technologies XXVI*; SPIE, 2022; Vol. 12004, pp 141–147. <https://doi.org/10.1117/12.2610654>.
- (51) Tyndall, N. F.; Kozak, D. A.; Pruessner, M. W.; Stievater, T. H.; Miller, B. L.; Wang, P. Y.; Butt, J. N. Waveguide Enhanced Raman Spectroscopy (WERS) for Biomarker Detection and Identification. In *Chemical, Biological, Radiological, Nuclear, and Explosives (CBRNE) Sensing XXIII*; SPIE, 2022; Vol. 12116, pp 122–125.
<https://doi.org/10.1117/12.2623361>.
- (52) Tyndall, N. F.; Stievater, T. H.; Kozak, D. A.; Koo, K.; McGill, R. A.; Pruessner, M. W.; Rabinovich, W. S.; Holmstrom, S. A. Waveguide-Enhanced Raman Spectroscopy of Trace Chemical Warfare Agent Simulants. *Opt. Lett., OL* **2018**, *43* (19), 4803–4806.
<https://doi.org/10.1364/OL.43.004803>.
- (53) Luta, E. P.; Watterson, B.; Yates, M. Z.; Miller, B. L. New Polymer Sorbents for Waveguide-Enhanced Raman Spectroscopy (WERS) and Refractive Index-Based Photonic Sensing. In *Chemical, Biological, Radiological, Nuclear, and Explosives (CBRNE) Sensing XXIII*; SPIE, 2022; Vol. 12116, pp 117–121.
<https://doi.org/10.1117/12.2619383>.
- (54) Laing, S.; Jamieson, L. E.; Faulds, K.; Graham, D. Surface-Enhanced Raman Spectroscopy for in Vivo Biosensing. *Nat Rev Chem* **2017**, *1* (8), 1–19.
<https://doi.org/10.1038/s41570-017-0060>.
- (55) Moura, C. C.; Tare, R. S.; Oreffo, R. O. C.; Mahajan, S. Raman Spectroscopy and Coherent Anti-Stokes Raman Scattering Imaging: Prospective Tools for Monitoring Skeletal Cells and Skeletal Regeneration. *Journal of The Royal Society Interface* **2016**, *13* (118), 20160182. <https://doi.org/10.1098/rsif.2016.0182>.
- (56) Wilson, E. B. A Partial Interpretation of the Raman and Infrared Spectra of Benzene. *Phys. Rev.* **1934**, *46* (2), 146–147. <https://doi.org/10.1103/PhysRev.46.146.2>.
- (57) Gardner, A. M.; Wright, T. G. Consistent Assignment of the Vibrations of Monosubstituted Benzenes. *The Journal of Chemical Physics* **2011**, *135* (11), 114305.
<https://doi.org/10.1063/1.3638266>.
- (58) Tuttle, W. D.; Gardner, A. M.; Andrejeva, A.; Kemp, D. J.; Wakefield, J. C. A.; Wright, T. G. Consistent Assignment of the Vibrations of Symmetric and Asymmetric Ortho-

List of References

- Disubstituted Benzenes. *Journal of Molecular Spectroscopy* **2018**, *344*, 46–60. <https://doi.org/10.1016/j.jms.2017.10.011>.
- (59) Le Ru, E. C.; Etchegoin, P. G. *Principles of Surface-Enhanced Raman Spectroscopy: And Related Plasmonic Effects*, 1st ed.; Elsevier: Amsterdam ; Boston, 2009.
- (60) Ulman, A. Formation and Structure of Self-Assembled Monolayers. *Chem. Rev.* **1996**, *96* (4), 1533–1554. <https://doi.org/10.1021/cr9502357>.
- (61) Budach, W.; Abel, A. P.; Bruno, A. E.; Neuschäfer, D. Planar Waveguides as High-Performance Sensing Platforms for Fluorescence-Based Multiplexed Oligonucleotide Hybridization Assays. *Anal. Chem.* **1999**, *71* (16), 3347–3355. <https://doi.org/10.1021/ac990092e>.
- (62) Brovelli, D.; Hähner, G.; Ruiz, L.; Hofer, R.; Kraus, G.; Waldner, A.; Schlösser, J.; Oroszlan, P.; Ehrat, M.; Spencer, N. D. Highly Oriented, Self-Assembled Alkanephosphate Monolayers on Tantalum(V) Oxide Surfaces. *Langmuir* **1999**, *15* (13), 4324–4327. <https://doi.org/10.1021/la981758n>.
- (63) Hofer, R.; Textor, M.; Spencer, N. D. Alkyl Phosphate Monolayers, Self-Assembled from Aqueous Solution onto Metal Oxide Surfaces. *Langmuir* **2001**, *17* (13), 4014–4020. <https://doi.org/10.1021/la001756e>.
- (64) Chen, X.; Luais, E.; Darwish, N.; Ciampi, S.; Thordarson, P.; Gooding, J. J. Studies on the Effect of Solvents on Self-Assembled Monolayers Formed from Organophosphonic Acids on Indium Tin Oxide. *Langmuir* **2012**, *28* (25), 9487–9495. <https://doi.org/10.1021/la3010129>.
- (65) Textor, M.; Ruiz, L.; Hofer, R.; Rossi, A.; Feldman, K.; Hähner, G.; Spencer, N. D. Structural Chemistry of Self-Assembled Monolayers of Octadecylphosphoric Acid on Tantalum Oxide Surfaces. *Langmuir* **2000**, *16* (7), 3257–3271. <https://doi.org/10.1021/la990941t>.
- (66) Gao, W.; Reven, L. Solid-State NMR Studies of Self-Assembled Monolayers. *Langmuir* **1995**, *11* (6), 1860–1863. <https://doi.org/10.1021/la00006a007>.
- (67) Gao, W.; Dickinson, L.; Grozinger, C.; Morin, F. G.; Reven, L. Self-Assembled Monolayers of Alkylphosphonic Acids on Metal Oxides. *Langmuir* **1996**, *12* (26), 6429–6435. <https://doi.org/10.1021/la9607621>.
- (68) Maege, I.; Jaehne, E.; Henke, A.; Adler, H.-J. P.; Bram, C.; Jung, C.; Stratmann, M. Ultrathin Organic Layers for Corrosion Protection. *Macromolecular Symposia* **1998**, *126* (1), 7–24. <https://doi.org/10.1002/masy.19981260104>.
- (69) Bram, C.; Jung, C.; Stratmann, M. Self Assembled Molecular Monolayers on Oxidized Inhomogeneous Aluminum Surfaces. *Fresenius J Anal Chem* **1997**, *358* (1), 108–111. <https://doi.org/10.1007/s002160050357>.
- (70) Tull, E. J.; Bartlett, P. N.; Murugan, G. S.; Wilkinson, J. S. Manipulating Spheres That Sink: Assembly of Micrometer Sized Glass Spheres for Optical Coupling. *Langmuir* **2009**, *25* (3), 1872–1880. <https://doi.org/10.1021/la803560s>.

- (71) Pellerite, M. J.; Dunbar, T. D.; Boardman, L. D.; Wood, E. J. Effects of Fluorination on Self-Assembled Monolayer Formation from Alkanephosphonic Acids on Aluminum: Kinetics and Structure. *J. Phys. Chem. B* **2003**, *107* (42), 11726–11736. <https://doi.org/10.1021/jp0354200>.
- (72) Vega, A.; Thissen, P.; Chabal, Y. J. Environment-Controlled Tethering by Aggregation and Growth of Phosphonic Acid Monolayers on Silicon Oxide. *Langmuir* **2012**, *28* (21), 8046–8051. <https://doi.org/10.1021/la300709n>.
- (73) Thissen, P.; Valtiner, M.; Grundmeier, G. Stability of Phosphonic Acid Self-Assembled Monolayers on Amorphous and Single-Crystalline Aluminum Oxide Surfaces in Aqueous Solution. *Langmuir* **2010**, *26* (1), 156–164. <https://doi.org/10.1021/la900935s>.
- (74) Hanson, E. L.; Schwartz, J.; Nickel, B.; Koch, N.; Danisman, M. F. Bonding Self-Assembled, Compact Organophosphonate Monolayers to the Native Oxide Surface of Silicon. *J. Am. Chem. Soc.* **2003**, *125* (51), 16074–16080. <https://doi.org/10.1021/ja035956z>.
- (75) Schmitt Pauly, C.; Genix, A.-C.; Alauzun, J. G.; Guerrero, G.; Appavou, M.-S.; Pérez, J.; Oberdisse, J.; Mutin, P. H. Simultaneous Phase Transfer and Surface Modification of TiO₂ Nanoparticles Using Alkylphosphonic Acids: Optimization and Structure of the Organosols. *Langmuir* **2015**, *31* (40), 10966–10974. <https://doi.org/10.1021/acs.langmuir.5b02833>.
- (76) Bhartia, B.; Bacher, N.; Jayaraman, S.; Khatib, S.; Song, J.; Guo, S.; Troadec, C.; Puniredd, S. R.; Srinivasan, M. P.; Haick, H. Application of Organophosphonic Acids by One-Step Supercritical CO₂ on 1D and 2D Semiconductors: Toward Enhanced Electrical and Sensing Performances. *ACS Appl. Mater. Interfaces* **2015**, *7* (27), 14885–14895. <https://doi.org/10.1021/acsami.5b03597>.
- (77) Chen, D.; Wu, H. K. Y.; Naderi-Gohar, S.; Wu, Y.; Huang, Y.; Nie, H.-Y. An Extremely Rapid Dip-Coating Method for Self-Assembly of Octadecylphosphonic Acid and Its Thermal Stability on an Aluminum Film. *J. Mater. Chem. C* **2014**, *2* (46), 9941–9948. <https://doi.org/10.1039/C4TC02017K>.
- (78) Bulusu, A.; Paniagua, S. A.; MacLeod, B. A.; Sigdel, A. K.; Berry, J. J.; Olson, D. C.; Marder, S. R.; Graham, S. Efficient Modification of Metal Oxide Surfaces with Phosphonic Acids by Spray Coating. *Langmuir* **2013**, *29* (12), 3935–3942. <https://doi.org/10.1021/la303354t>.
- (79) Sang, L.; Knesting, K. M.; Bulusu, A.; Sigdel, A. K.; Giordano, A. J.; Marder, S. R.; Berry, J. J.; Graham, S.; Ginger, D. S.; Pemberton, J. E. Effect of Time and Deposition Method on Quality of Phosphonic Acid Modifier Self-Assembled Monolayers on Indium Zinc Oxide. *Applied Surface Science* **2016**, *389*, 190–198. <https://doi.org/10.1016/j.apsusc.2016.06.183>.
- (80) Pujari, S. P.; Scheres, L.; Marcelis, A. T. M.; Zuilhof, H. Covalent Surface Modification of Oxide Surfaces. *Angewandte Chemie International Edition* **2014**, *53* (25), 6322–6356. <https://doi.org/10.1002/anie.201306709>.

List of References

- (81) Randon, J.; Blanc, P.; Paterson, R. Modification of Ceramic Membrane Surfaces Using Phosphoric Acid and Alkyl Phosphonic Acids and Its Effects on Ultrafiltration of BSA Protein. *Journal of Membrane Science* **1995**, *98* (1), 119–129. [https://doi.org/10.1016/0376-7388\(94\)00183-Y](https://doi.org/10.1016/0376-7388(94)00183-Y).
- (82) Giza, M.; Thissen, P.; Grundmeier, G. Adsorption Kinetics of Organophosphonic Acids on Plasma-Modified Oxide-Covered Aluminum Surfaces. *Langmuir* **2008**, *24* (16), 8688–8694. <https://doi.org/10.1021/la8000619>.
- (83) Luschtinetz, R.; Oliveira, A. F.; Duarte, H. A.; Seifert, G. Self-Assembled Monolayers of Alkylphosphonic Acids on Aluminum Oxide Surfaces – A Theoretical Study. *Zeitschrift für anorganische und allgemeine Chemie* **2010**, *636* (8), 1506–1512. <https://doi.org/10.1002/zaac.201000016>.
- (84) Chen, X.; Chockalingam, M.; Liu, G.; Luais, E.; Gui, A. L.; Gooding, J. J. A Molecule with Dual Functionality 4-Aminophenylmethylphosphonic Acid: A Comparison Between Layers Formed on Indium Tin Oxide by In Situ Generation of an Aryl Diazonium Salt or by Self-Assembly of the Phosphonic Acid. *Electroanalysis* **2011**, *23* (11), 2633–2642. <https://doi.org/10.1002/elan.201100337>.
- (85) Jagadeesh, R. V.; Lakshminarayanan, V. Adsorption Kinetics of Phosphonic Acids and Proteins on Functionalized Indium Tin Oxide Surfaces Using Electrochemical Impedance Spectroscopy. *Electrochimica Acta* **2016**, *197*, 1–9. <https://doi.org/10.1016/j.electacta.2016.03.008>.
- (86) Muriano, A.; Thayil, K. N. A.; Salvador, J.-P.; Loza-Alvarez, P.; Soria, S.; Galve, R.; Marco, M.-P. Two-Photon Fluorescent Immunosensor for Androgenic Hormones Using Resonant Grating Waveguide Structures. *Sensors and Actuators B: Chemical* **2012**, *174*, 394–401. <https://doi.org/10.1016/j.snb.2012.08.006>.
- (87) Lu, X.; Nicovich, P. R.; Gaus, K.; Gooding, J. J. Towards Single Molecule Biosensors Using Super-Resolution Fluorescence Microscopy. *Biosensors and Bioelectronics* **2017**, *93*, 1–8. <https://doi.org/10.1016/j.bios.2016.10.048>.
- (88) Chockalingam, M.; Magenau, A.; Parker, S. G.; Parviz, M.; Vivekchand, S. R. C.; Gaus, K.; Gooding, J. J. Biointerfaces on Indium–Tin Oxide Prepared from Organophosphonic Acid Self-Assembled Monolayers. *Langmuir* **2014**, *30* (28), 8509–8515. <https://doi.org/10.1021/la501774b>.
- (89) White, M. A.; Johnson, J. A.; Koberstein, J. T.; Turro, N. J. Toward the Syntheses of Universal Ligands for Metal Oxide Surfaces: Controlling Surface Functionality through Click Chemistry. *J. Am. Chem. Soc.* **2006**, *128* (35), 11356–11357. <https://doi.org/10.1021/ja064041s>.
- (90) Busch, G.; Jaehne, E.; Cai, X.; Oberoi, S.; Adler, H.-J. P. Ultrathin Layers for Adhesion Promotion. *Synthetic Metals* **2003**, *137* (1), 871–872. [https://doi.org/10.1016/S0379-6779\(02\)01097-4](https://doi.org/10.1016/S0379-6779(02)01097-4).
- (91) Arnould, C.; Denayer, J.; Planckaert, M.; Delhalle, J.; Mekhalif, Z. Bilayers Coating on Titanium Surface: The Impact on the Hydroxyapatite Initiation. *Journal of Colloid and Interface Science* **2010**, *341* (1), 75–82. <https://doi.org/10.1016/j.jcis.2009.09.030>.

- (92) Hotchkiss, P. J.; Jones, S. C.; Paniagua, S. A.; Sharma, A.; Kippelen, B.; Armstrong, N. R.; Marder, S. R. The Modification of Indium Tin Oxide with Phosphonic Acids: Mechanism of Binding, Tuning of Surface Properties, and Potential for Use in Organic Electronic Applications. *Acc. Chem. Res.* **2012**, *45* (3), 337–346. <https://doi.org/10.1021/ar200119g>.
- (93) Woodward, J. T.; Ulman, A.; Schwartz, D. K. Self-Assembled Monolayer Growth of Octadecylphosphonic Acid on Mica. *Langmuir* **1996**, *12* (15), 3626–3629. <https://doi.org/10.1021/la9510689>.
- (94) De Palma, R.; Laureyn, W.; Frederix, F.; Bonroy, K.; Pireaux, J.-J.; Borghs, G.; Maes, G. Formation of Dense Self-Assembled Monolayers of (n-Decyl)Trichlorosilanes on Ta/Ta₂O₅. *Langmuir* **2007**, *23* (2), 443–451. <https://doi.org/10.1021/la061951e>.
- (95) Koh, S. E.; McDonald, K. D.; Holt, D. H.; Dulcey, C. S.; Chaney, J. A.; Pehrsson, P. E. Phenylphosphonic Acid Functionalization of Indium Tin Oxide: Surface Chemistry and Work Functions. *Langmuir* **2006**, *22* (14), 6249–6255. <https://doi.org/10.1021/la052379e>.
- (96) Dulcey, C. S.; Georger, Jacques H.; Chen, M.-S.; McElvany, S. W.; O’Ferrall, C. E.; Benezra, V. I.; Calvert, J. M. Photochemistry and Patterning of Self-Assembled Monolayer Films Containing Aromatic Hydrocarbon Functional Groups. *Langmuir* **1996**, *12* (6), 1638–1650. <https://doi.org/10.1021/la9509514>.
- (97) Neves, B. R. A.; Salmon, M. E.; Russell, P. E.; Troughton, E. B. Spread Coating of OPA on Mica: From Multilayers to Self-Assembled Monolayers. *Langmuir* **2001**, *17* (26), 8193–8198. <https://doi.org/10.1021/la010909a>.
- (98) Acosta-Maeda, T. E.; Misra, A. K.; Porter, J. N.; Bates, D. E.; Sharma, S. K. Remote Raman Efficiencies and Cross-Sections of Organic and Inorganic Chemicals. *Appl. Spectrosc., AS* **2017**, *71* (5), 1025–1038.
- (99) Emmons, E. D.; Guicheteau, J. A.; Fountai, A. W.; Christesen, S. D. Comparison of Visible and Near-Infrared Raman Cross-Sections of Explosives in Solution and in the Solid State. *Appl Spectrosc* **2012**, *66* (6), 636–643. <https://doi.org/10.1366/11-06549>.
- (100) Pelletier, M. J. Quantitative Analysis Using Raman Spectrometry. *Appl. Spectrosc., AS* **2003**, *57* (1), 20A–42A.
- (101) Ray, K. G.; McCreery, R. L. Simplified Calibration of Instrument Response Function for Raman Spectrometers Based on Luminescent Intensity Standards. *Appl. Spectrosc., AS* **1997**, *51* (1), 108–116.
- (102) Choquette, S. J.; Etz, E. S.; Hurst, W. S.; Blackburn, D. H.; Leigh, S. D. Relative Intensity Correction of Raman Spectrometers: NIST SRMs 2241 Through 2243 for 785 Nm, 532 Nm, and 488 Nm/514.5 Nm Excitation. *Appl. Spectrosc., AS* **2007**, *61* (2), 117–129.
- (103) Rodriguez, J. D.; Westenberger, B. J.; Buhse, L. F.; Kauffman, J. F. Standardization of Raman Spectra for Transfer of Spectral Libraries across Different Instruments. *Analyst* **2011**, *136* (20), 4232–4240. <https://doi.org/10.1039/C1AN15636E>.

List of References

- (104) *Vibrational Spectra of Benzene Derivatives - 1st Edition*.
<https://www.elsevier.com/books/vibrational-spectra-of-benzene-derivatives/varsanyi/978-0-12-714950-9> (accessed 2022-09-13).
- (105) King, G. W.; van Putten, A. A. G. Diethynylbenzenes; The Vibrational Spectra of Some Deuterated Isomers. *Journal of Molecular Spectroscopy* **1978**, *70* (1), 53–67.
[https://doi.org/10.1016/0022-2852\(78\)90008-5](https://doi.org/10.1016/0022-2852(78)90008-5).
- (106) Ivanov, A. V.; Koklin, A. E.; Uvarova, E. B.; Kustov, L. M. A DRIFT Spectroscopic Study of Acetylene Adsorbed on Metal Oxides. *Phys. Chem. Chem. Phys.* **2003**, *5* (20), 4718–4723. <https://doi.org/10.1039/B307138C>.
- (107) Mordenti, D.; Grotz, P.; Knözinger, H. Methylacetylene and Tert-Butylacetylene as IR-Probe Molecules for the Characterisation of Basicity. *Catalysis Today* **2001**, *70* (1), 83–90. [https://doi.org/10.1016/S0920-5861\(01\)00409-6](https://doi.org/10.1016/S0920-5861(01)00409-6).
- (108) Tao, F.; Qiao, M. H.; Li, Z. H.; Yang, L.; Dai, Y. J.; Huang, H. G.; Xu, G. Q. Adsorption of Phenylacetylene on Si(100)-2×1: Reaction Mechanism and Formation of a Styrene-like π -Conjugation System. *Phys. Rev. B* **2003**, *67* (11), 115334.
<https://doi.org/10.1103/PhysRevB.67.115334>.
- (109) Prystupa, D. A.; Anderson, A.; Torrie, B. H. Raman and Infrared Study of Solid Benzyl Alcohol. *Journal of Raman Spectroscopy* **1994**, *25* (2), 175–182.
<https://doi.org/10.1002/jrs.1250250206>.
- (110) Oliveira, M. J.; Quaresma, P.; Peixoto de Almeida, M.; Araújo, A.; Pereira, E.; Fortunato, E.; Martins, R.; Franco, R.; Águas, H. Office Paper Decorated with Silver Nanostars - an Alternative Cost Effective Platform for Trace Analyte Detection by SERS. *Sci Rep* **2017**, *7* (1), 2480. <https://doi.org/10.1038/s41598-017-02484-8>.
- (111) de Almeida, M. P.; Leopold, N.; Franco, R.; Pereira, E. Expedite SERS Fingerprinting of Portuguese White Wines Using Plasmonic Silver Nanostars. *Frontiers in Chemistry* **2019**, *7*.
- (112) Osawa, M.; Matsuda, N.; Yoshii, K.; Uchida, I. Charge Transfer Resonance Raman Process in Surface-Enhanced Raman Scattering from p-Aminothiophenol Adsorbed on Silver: Herzberg-Teller Contribution. *J. Phys. Chem.* **1994**, *98* (48), 12702–12707.
<https://doi.org/10.1021/j100099a038>.
- (113) Kim, K.; Choi, J.-Y.; Lee, H. B.; Shin, K. S. Raman Scattering of 4-Aminobenzenethiol Sandwiched between Ag Nanoparticle and Macroscopically Smooth Au Substrate: Effects of Size of Ag Nanoparticles and the Excitation Wavelength. *J. Chem. Phys.* **2011**, *135* (12), 124705. <https://doi.org/10.1063/1.3640890>.
- (114) Speed, J. Tailoring Plasmonic Substrates for SERS. phd, University of Southampton, 2011. <https://eprints.soton.ac.uk/191315/> (accessed 2023-06-13).
- (115) Choi, H.-K.; Shon, H. K.; Yu, H.; Lee, T. G.; Kim, Z. H. B2 Peaks in SERS Spectra of 4-Aminobenzenethiol: A Photochemical Artifact or a Real Chemical Enhancement? *J. Phys. Chem. Lett.* **2013**, *4* (7), 1079–1086. <https://doi.org/10.1021/jz4002828>.

- (116) Kim, K.; Shin, D.; Choi, J.-Y.; Kim, K. L.; Shin, K. S. Surface-Enhanced Raman Scattering Characteristics of 4-Aminobenzenethiol Derivatives Adsorbed on Silver. *J. Phys. Chem. C* **2011**, *115* (50), 24960–24966. <https://doi.org/10.1021/jp208945s>.
- (117) Huang, Y.-F.; Zhu, H.-P.; Liu, G.-K.; Wu, D.-Y.; Ren, B.; Tian, Z.-Q. When the Signal Is Not from the Original Molecule To Be Detected: Chemical Transformation of Para-Aminothiophenol on Ag during the SERS Measurement. *J. Am. Chem. Soc.* **2010**, *132* (27), 9244–9246. <https://doi.org/10.1021/ja101107z>.
- (118) Fang, Y.; Li, Y.; Xu, H.; Sun, M. Ascertaining p,P'-Dimercaptoazobenzene Produced from p-Aminothiophenol by Selective Catalytic Coupling Reaction on Silver Nanoparticles. *Langmuir* **2010**, *26* (11), 7737–7746. <https://doi.org/10.1021/la904479q>.
- (119) Tian, F.; Bonnier, F.; Casey, A.; Shanahan, A. E.; Byrne, H. J. Surface Enhanced Raman Scattering with Gold Nanoparticles: Effect of Particle Shape. *Anal. Methods* **2014**, *6* (22), 9116–9123. <https://doi.org/10.1039/C4AY02112F>.
- (120) Maurer, V.; Frank, C.; Porsiel, J. C.; Zellmer, S.; Garnweitner, G.; Stosch, R. Step-by-Step Monitoring of a Magnetic and SERS-Active Immunosensor Assembly for Purification and Detection of Tau Protein. *Journal of Biophotonics* **2020**, *13* (3), e201960090. <https://doi.org/10.1002/jbio.201960090>.
- (121) Tezcan, T.; Hsu, C.-H. High-Sensitivity SERS Based Sensing on the Labeling Side of Glass Slides Using Low Branched Gold Nanoparticles Prepared with Surfactant-Free Synthesis. *RSC Adv.* **2020**, *10* (56), 34290–34298. <https://doi.org/10.1039/D0RA02490B>.
- (122) Duffield, C.; Lyu, N.; Wang, Y. Synthesis and Characterization of Reporter Molecules Embedded Core-Shell Nanoparticles as SERS Nanotags. *J. Innov. Opt. Health Sci.* **2021**, *14* (04), 2141007. <https://doi.org/10.1142/S1793545821410078>.
- (123) Kamińska, A.; Winkler, K.; Kowalska, A.; Witkowska, E.; Szyborski, T.; Janeczek, A.; Waluk, J. SERS-Based Immunoassay in a Microfluidic System for the Multiplexed Recognition of Interleukins from Blood Plasma: Towards Picogram Detection. *Sci Rep* **2017**, *7* (1), 10656. <https://doi.org/10.1038/s41598-017-11152-w>.
- (124) Mentele, M. M.; Cunningham, J.; Koehler, K.; Volckens, J.; Henry, C. S. Microfluidic Paper-Based Analytical Device for Particulate Metals. *Anal. Chem.* **2012**, *84* (10), 4474–4480. <https://doi.org/10.1021/ac300309c>.
- (125) Saha, A.; Jana, N. R. Paper-Based Microfluidic Approach for Surface-Enhanced Raman Spectroscopy and Highly Reproducible Detection of Proteins beyond Picomolar Concentration. *ACS Appl. Mater. Interfaces* **2015**, *7* (1), 996–1003. <https://doi.org/10.1021/am508123x>.
- (126) Schilling, K. M.; Lepore, A. L.; Kurian, J. A.; Martinez, A. W. Fully Enclosed Microfluidic Paper-Based Analytical Devices. *Anal. Chem.* **2012**, *84* (3), 1579–1585. <https://doi.org/10.1021/ac202837s>.
- (127) Wang, R.; Kim, K.; Choi, N.; Wang, X.; Lee, J.; Jeon, J. H.; Rhie, G.; Choo, J. Highly Sensitive Detection of High-Risk Bacterial Pathogens Using SERS-Based Lateral Flow

List of References

- Assay Strips. *Sensors and Actuators B: Chemical* **2018**, *270*, 72–79.
<https://doi.org/10.1016/j.snb.2018.04.162>.
- (128) Carrilho, E.; Martinez, A. W.; Whitesides, G. M. Understanding Wax Printing: A Simple Micropatterning Process for Paper-Based Microfluidics. *Anal. Chem.* **2009**, *81* (16), 7091–7095. <https://doi.org/10.1021/ac901071p>.
- (129) Lu, Y.; Shi, W.; Jiang, L.; Qin, J.; Lin, B. Rapid Prototyping of Paper-Based Microfluidics with Wax for Low-Cost, Portable Bioassay. *ELECTROPHORESIS* **2009**, *30* (9), 1497–1500. <https://doi.org/10.1002/elps.200800563>.
- (130) Martinez, A. W.; Phillips, S. T.; Butte, M. J.; Whitesides, G. M. Patterned Paper as a Platform for Inexpensive, Low-Volume, Portable Bioassays. *Angewandte Chemie International Edition* **2007**, *46* (8), 1318–1320.
<https://doi.org/10.1002/anie.200603817>.
- (131) Mabbott, S.; Fernandes, S. C.; Schechinger, M.; Cote, G. L.; Faulds, K.; Mace, C. R.; Graham, D. Detection of Cardiovascular Disease Associated MiR-29a Using Paper-Based Microfluidics and Surface Enhanced Raman Scattering. *Analyst* **2020**, *145* (3), 983–991. <https://doi.org/10.1039/C9AN01748H>.
- (132) Qu, L.-L.; Liu, Y.-Y.; He, S.-H.; Chen, J.-Q.; Liang, Y.; Li, H.-T. Highly Selective and Sensitive Surface Enhanced Raman Scattering Nanosensors for Detection of Hydrogen Peroxide in Living Cells. *Biosensors and Bioelectronics* **2016**, *77*, 292–298.
<https://doi.org/10.1016/j.bios.2015.09.039>.
- (133) Tabatabaei, M.; Wallace, G. Q.; Caetano, F. A.; Gillies, E. R.; Ferguson, S. S. G.; Lagugné-Labarthe, F. Controlled Positioning of Analytes and Cells on a Plasmonic Platform for Glycan Sensing Using Surface Enhanced Raman Spectroscopy. *Chem Sci* **2016**, *7* (1), 575–582. <https://doi.org/10.1039/c5sc03332b>.
- (134) Su, H.; Wang, Y.; Yu, Z.; Liu, Y.; Zhang, X.; Wang, X.; Sui, H.; Sun, C.; Zhao, B. Surface-Enhanced Raman Spectroscopy Study on the Structure Changes of 4-Mercaptophenylboronic Acid under Different PH Conditions. *Spectrochimica Acta Part A: Molecular and Biomolecular Spectroscopy* **2017**, *185*, 336–342.
<https://doi.org/10.1016/j.saa.2017.05.068>.
- (135) Sun, F.; Galvan, D. D.; Jain, P.; Yu, Q. Multi-Functional, Thiophenol-Based Surface Chemistry for Surface-Enhanced Raman Spectroscopy. *Chem. Commun.* **2017**, *53* (33), 4550–4561. <https://doi.org/10.1039/C7CC01577A>.
- (136) Sun, F.; Bai, T.; Zhang, L.; Ella-Menye, J.-R.; Liu, S.; Nowinski, A. K.; Jiang, S.; Yu, Q. Sensitive and Fast Detection of Fructose in Complex Media via Symmetry Breaking and Signal Amplification Using Surface-Enhanced Raman Spectroscopy. *Anal. Chem.* **2014**, *86* (5), 2387–2394. <https://doi.org/10.1021/ac4040983>.
- (137) Kong, K. V.; Ho, C. J. H.; Gong, T.; Lau, W. K. O.; Olivo, M. Sensitive SERS Glucose Sensing in Biological Media Using Alkyne Functionalized Boronic Acid on Planar Substrates. *Biosensors and Bioelectronics* **2014**, *56*, 186–191.
<https://doi.org/10.1016/j.bios.2013.12.062>.
- (138) Wallace, G. Q.; Tabatabaei, M.; Zuin, M. S.; Workentin, M. S.; Lagugné-Labarthe, F. A Nanoaggregate-on-Mirror Platform for Molecular and Biomolecular Detection by

- Surface-Enhanced Raman Spectroscopy. *Anal Bioanal Chem* **2016**, *408* (2), 609–618. <https://doi.org/10.1007/s00216-015-9142-z>.
- (139) Gu, X.; Wang, H.; Schultz, Z. D.; Camden, J. P. Sensing Glucose in Urine and Serum and Hydrogen Peroxide in Living Cells by Use of a Novel Boronate Nanoprobe Based on Surface-Enhanced Raman Spectroscopy. *Anal Chem* **2016**, *88* (14), 7191–7197. <https://doi.org/10.1021/acs.analchem.6b01378>.
- (140) Li, S.; Zhou, Q.; Chu, W.; Zhao, W.; Zheng, J. Surface-Enhanced Raman Scattering Behaviour of 4-Mercaptophenyl Boronic Acid on Assembled Silver Nanoparticles. *Phys. Chem. Chem. Phys.* **2015**, *17* (27), 17638–17645. <https://doi.org/10.1039/C5CP02409A>.
- (141) Ji, W.; Xue, X.; Ruan, W.; Wang, C.; Ji, N.; Chen, L.; Li, Z.; Song, W.; Zhao, B.; Lombardi, J. R. Scanned Chemical Enhancement of Surface-Enhanced Raman Scattering Using a Charge-Transfer Complex. *Chem. Commun.* **2011**, *47* (8), 2426–2428. <https://doi.org/10.1039/C0CC03697H>.
- (142) Wei, X.; Su, S.; Guo, Y.; Jiang, X.; Zhong, Y.; Su, Y.; Fan, C.; Lee, S.-T.; He, Y. A Molecular Beacon-Based Signal-Off Surface-Enhanced Raman Scattering Strategy for Highly Sensitive, Reproducible, and Multiplexed DNA Detection. *Small* **2013**, *9* (15), 2493–2499. <https://doi.org/10.1002/smll.201202914>.
- (143) Dong, J.; Ueda, H. Recent Advances in Quenchbody, a Fluorescent Immunosensor. *Sensors (Basel)* **2021**, *21* (4), 1223. <https://doi.org/10.3390/s21041223>.
- (144) Yan, X.; Le, X. C.; Zhang, H. Antibody-Bridged Beacon for Homogeneous Detection of Small Molecules. *Anal. Chem.* **2018**, *90* (16), 9667–9672. <https://doi.org/10.1021/acs.analchem.8b02510>.
- (145) Huang, C.-Y.; Balakrishnan, G.; Spiro, T. G. Protein Secondary Structure from Deep-UV Resonance Raman Spectroscopy. *Journal of Raman Spectroscopy* **2006**, *37* (1–3), 277–282. <https://doi.org/10.1002/jrs.1440>.